Institut für
Mechatronische Systeme
imes Leibniz Universität Hannover

Leibniz
Universität
Hannover

Integrated Control for High-Speed Railway Running Gears with Driven Independently Rotating Wheels

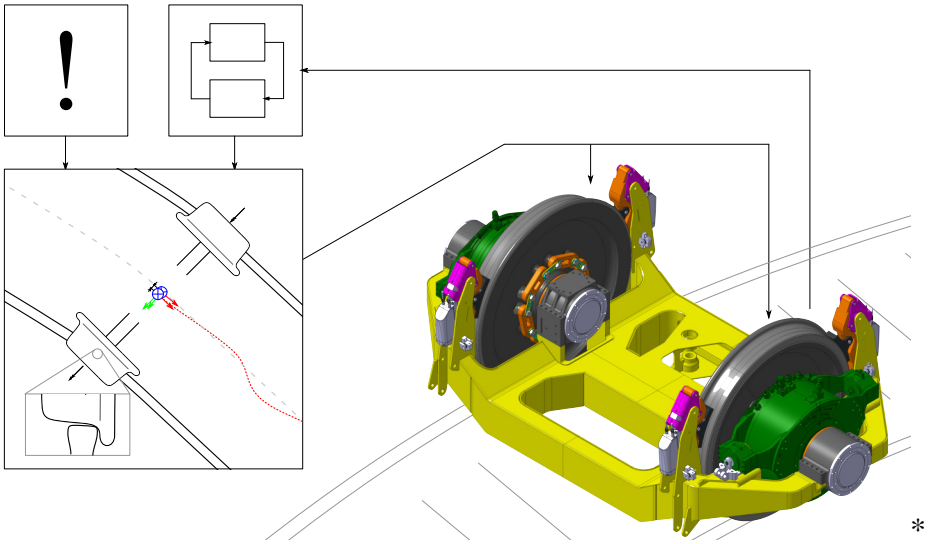

*

Master's Thesis M-12/2022-1157

Jan-Hendrik Ewering
Registration Number 10035201

Hannover, December 14th, 2022

First Examiner	Dr.-Ing. habil. Hans-Georg Jacob
Second Examiner	Prof. Dr.-Ing. Jörg Wallaschek
Supervisor	Simon F. G. Ehlers, M.Sc.
	Dr.-Ing. Christoph Schwarz

*CAD rendering by [Dav21]

Sperrvermerk

Die vorliegende Arbeit beinhaltet vertrauliche Informationen, die aus Gründen der Geheimhaltung nicht veröffentlicht, vervielfältigt oder verbreitet werden dürfen. Die Arbeit ist jedoch Mitarbeitenden der Leibniz Universität Hannover im Rahmen des Prüfungsverfahrens zugänglich zu machen. Dies beinhaltet ausdrücklich auch einen hochschulinternen Vortrag. Des weiteren beinhaltet dies eine Plagiatsprüfung der Arbeit, bei der die Arbeit in digitaler Form bei dem Dienst Docoloc hochgeladen wird.
Das Einsehen oder die Weitergabe dieser Arbeit darf ab dem Datum der Abgabe für einen Zeitraum von **6** Monaten nur mit ausdrücklicher Genehmigung vom

Institut für Systemdynamik und Regelungstechnik
Deutsches Zentrum für Luft- und Raumfahrt e.V. (DLR)
Adresse: Münchener Str. 20, 82234 Wessling
Ansprechperson: Prof. Dr.-Ing. Dipl.-Math. Johann Bals
Kontaktdaten: +49 8153 28-2433, Johann.Bals@dlr.de

erfolgen.

Personen, die während des oben genannten Zeitraums Zugang zur Arbeit erhalten, haben die Einhaltung dieser Vereinbarung gegenüber Dritten sicherzustellen.

Nach Ablauf der Frist erlischt die Pflicht zur Geheimhaltung.

Andreas Heckmann
Digital signiert von Andreas Heckmann
DN: C=DE, O=Deutsches Zentrum fuer Luft- und Raumfahrt e.V. (DLR), CN=Andreas Heckmann
Grund: Ich stimme den angegebenen Teilen dieses Dokuments zu
Ort: Oberpfaffenhofen
Datum: 2022.12.14 09:28:15+01'00'
Foxit PDF Editor Version: 12.0.2

Vertretung des DLR

Dr.-Ing. habil. Hans-Georg Jacob

Jan-Hendrik Ewering

Institut für Mechatronische Systeme
imes Leibniz Universität Hannover

Leibniz Universität Hannover

M-12/2022-1157

Declaration of Authorship

Name:	**Jan-Hendrik Ewering**
Registration no.:	10035201
Thesis title:	Integrated Control for High-Speed Railway Running Gears with Driven Independently Rotating Wheels
Type of thesis:	Master's Thesis
Study program:	Mechanical Engineering
Submission date:	December 14th, 2022
First examiner :	Dr.-Ing. habil. Hans-Georg Jacob
Second examiner:	Prof. Dr.-Ing. Jörg Wallaschek
Supervisor:	Simon F. G. Ehlers, M.Sc.
	Dr.-Ing. Christoph Schwarz

I, *Jan-Hendrik Ewering*, hereby affirm that the Master's Thesis entitled *Integrated Control for High-Speed Railway Running Gears with Driven Independently Rotating Wheels* was written independently, that no references and aids other than those indicated were used, that all passages of the thesis which were taken over literally or analogously from other sources are marked as such and that the thesis has not yet been presented to any examination board in the same or similar form.
I hereby agree to the transmission of my work also to external services for plagiarism checking by plagiarism software.

Hannover, December 14th, 2022

(Jan-Hendrik Ewering)

Abstract

Railway traffic is a forward-looking possibility to facilitate the transition to a sustainable and environmentally friendly mobility. To achieve a significant modal shift, efforts in the entire railway sector are demanded, including infrastructure, train operation, and of course the railway vehicle itself.

In this light, railway running gears with Independently Rotating Wheels (IRW) can improve wear figures, comfort and safety significantly, if certain measures for wheel carrier stabilization are taken. Apart from lateral guidance, the longitudinal control is of crucial importance for railway safety. Therefore, the current thesis contributes to the development of a safe, reliable, and efficient rail transport by exploring new concepts for the integrated control of high-speed railway running gears with IRW. It is conducted as part of the initiative Next Generation Train (NGT) of the German Aerospace Center (German: Deutsches Zentrum für Luft- und Raumfahrt e.V. (DLR)).

There are two main methodological contributions in the present work. First, Model Predictive Control (MPC) approaches are investigated based on an extensive literature review and a thorough system analysis. Different schemes, such as Linear Time-Variant (LTV) and nonlinear MPC are compared. The MPC schemes are able to make use of tabulated track geometry data and preview information about desired system behavior. Second, a novel adhesion-based control law is devised for reliable traction and braking without knowledge of the adhesion conditions in the wheel-rail contacts. It can handle regular operation as well as critical driving scenarios. Thus, a holistic framework for integrated control of railway running gears with IRW is contributed in the present work.

In terms of experimental verification, co-simulation results with the state-of-the-art Multi-Body Simulation (MBS) software SIMPACK show the effectiveness of the approach in comparison with existing controllers. Various scenarios are considered, including curving, changing velocities up to 400 km/h and abruptly changing wheel-rail adhesion conditions.

Due to the novelty of the devised controller and the promising results, the main part of this thesis is presented as a scientific publication in order to be published as a journal paper.

Contents

1 Introduction **1**
1.1 Development Framework . . . 1
1.1.1 Next Generation Train . . . 1
1.1.2 Motivation . . . 2
1.1.3 Objectives . . . 4
1.2 System Analysis and Approach . . . 6

2 Literature Review **8**
2.1 Wheel-Rail Contacts . . . 8
2.2 Control in Railway Running Gears . . . 11
2.3 Integrated Control . . . 14
2.4 Model Predictive Control . . . 15

3 Publication **17**

4 Further Description of Methods **29**
4.1 Modeling . . . 29
4.1.1 Track . . . 29
4.1.2 Running Gear with Driven Independently Rotating Wheels . . . 30
4.1.3 Wheel-Rail Interaction . . . 37
4.1.4 Simplified Model . . . 38
4.2 Control Synthesis . . . 38
4.2.1 Adhesion-based Control . . . 38
4.2.2 Linear Time-Variant Model Predictive Control . . . 40
4.2.3 Parameter Optimization . . . 42
4.3 Evaluation . . . 43
4.3.1 Programmatic Environment . . . 43
4.3.2 Further Results . . . 44

5 Conclusion and Outlook **50**
5.1 Conclusion . . . 50
5.2 Outlook . . . 51

Appendix **52**

A Dependent Variables of Wheel-Rail Contacts **53**

Bibliography **55**

List of Figures

1.1 Full scale prototype and integration test rig of a running gear with IRW. Primary wheel carrier is shown in blue and secondary suspension frame is shown in black [Deu22b]. 2
1.2 Possible control structure of the NGT with decentralized, integrated running gear controllers (Train figure adjusted from: DLR, CC-BY 3.0). *A priori* knowledge is denoted $\square^{-}$. Estimated quantities are denoted $\hat{\square}$. 5
1.3 Control-oriented system overview of a wheel carrier with IRW. Excerpt of the contact geometries. 6

2.1 Schematic adhesion-slip with good (a) and bad (b) adhesion conditions. . . . 9
2.2 Polach model for different spin slip values (excerpt from [Pol05]). 10
2.3 Locus diagram of a freely running (a) and a damped and spring loaded (b) solid axle wheelset. 11
2.4 Nonlinear Dynamic Inversion (NDI) scheme for lateral guidance of running gears with IRW (excerpt from [HKG20]). 13

4.1 Desired design Power Spectral Densities (PSD) according to [HPK18] and estimated PSD of randomly sampled track irregularity sequences. 30
4.2 Top view (a) and rear view (b) sketch of a railway running gear with IRW, including coordinate systems and transformations. Rear view is shown for relative yaw angle between track frame and wheel carrier frame $\psi - \psi_{\mathrm{Tr}} = 0$. 31
4.3 Contact search results z and φ dependent on ${}_{(\mathrm{Tr})}y_{\mathrm{Ax}}$ and ${}_{(\mathrm{Tr})}\psi_{\mathrm{Ax}}$. 37
4.4 Adhesion-slip characteristic (gray) with operational segments (I)-(IX) of the presented adhesion-based controller. 39
4.5 Environment for development and evaluation of the proposed control schemes in MATLAB (blue) and SIMULINK (orange), featuring an optional parameter optimization block (light blue). 43
4.6 MODELICA roller rig model, moderate acceleration, good adhesion conditions, sine sweep as controller input. 45
4.7 MODELICA roller rig model, $50\mathrm{km/h}$, $F_x^* = 0$, good adhesion conditions, ramp as controller input. 46

4.8 MODELICA roller rig model, $40\mathrm{km/h}$, changing braking demand, changing adhesion conditions, sine with ramp as controller input. 47
4.9 Good and poor adhesion conditions in the right and left wheel-rail contact. . . 48
4.10 Co-simulation result, evaluation track $\mathcal{T}_4$, $400\mathrm{km/h}$, good adhesion conditions, lateral error trajectory as controller input, $F_x^* = 0$. 49

A.1 Setting for optimization-based contact search between wheel and rail geometries along a grid of ${}_{(\mathrm{Tr})}y_{\mathrm{Ax}}$ and ${}_{(\mathrm{Tr})}\psi_{\mathrm{Ax}}$. Results are vertical wheel carrier position z with respect to the track frame, wheel carrier roll angle φ with respect to the track frame, wheel radii $r_{\mathrm{C}j}$, lateral contact positions $y_{\mathrm{C}j}$ and contact angles $\delta_{\mathrm{C}j}$ for $j \in \{\mathrm{ri}, \mathrm{le}\}$. 53
A.2 Contact search results r_{Cr}, y_{Cr} and δ_{Cr} dependent on ${}_{(\mathrm{Tr})}y_{\mathrm{Ax}}$ and ${}_{(\mathrm{Tr})}\psi_{\mathrm{Ax}}$. Results regarding the left side are mirrored about ${}_{(\mathrm{Tr})}y_{\mathrm{Ax}}$. 54

Nomenclature

General Conventions

a, A	Scalars
$\boldsymbol{v}$	Vectors
$\boldsymbol{M}$	Matrices
$\mathbf{0}$	Matrix of zeros of suitable dimension

Wheel-Rail Contacts

s_{x_j}	Longitudinal creepage in wheel-rail contact
s_{y_j}	Lateral creepage in wheel-rail contact
Ψ_j	Spin creepage in wheel-rail contact
F_{x_j}	Tangential wheel-rail contact force in longitudinal direction
F_{y_j}	Tangential wheel-rail contact force in lateral direction
F_{T_j}	Tangential wheel-rail contact force,
	i. e. $F_{\mathrm{T}_j} = \sqrt{F_{x_j}^2 + F_{y_j}^2}$
F_{N_j}	Normal wheel-rail contact force
f_{x_j}	Longitudinal adhesion in wheel-rail contact,
	i. e. $f_{x_j} = F_{x_j}/F_{\mathrm{N}_j}$
f_{y_j}	Longitudinal adhesion in wheel-rail contact,
	i. e. $f_{y_j} = F_{y_j}/F_{\mathrm{N}_j}$
Q	Wheel load
μ	Friction coefficient
ϵ_{T}	Gradient of tangential contact stress
a, b	Contact ellipse half axes
$c_{11_j}, c_{22_j}, c_{23_j}$	Kalker coefficients

$j \in \{\mathrm{ri}, \mathrm{le}\}$

Coordinate Frames

$(\mathrm{CF})_0$	Fixed inertial frame
$(\mathrm{CF})_i$	Coordinate frame i
${}_{(i)}\boldsymbol{v}$	General vector, described in $(\mathrm{CF})_i$

Rotation and Transformation Matrices

${}^{i}\boldsymbol{R}_{k}$	Rotation matrix, describes rotation from $(\mathrm{CF})_{k}$ to $(\mathrm{CF})_{i}$
${}^{i}\boldsymbol{T}_{k}$	Homogeneous transformation matrix, describes translation and rotation from $(\mathrm{CF})_{k}$ to $(\mathrm{CF})_{i}$
${}_{(i)}\tilde{\boldsymbol{r}}$	Position vector with homogeneous extension, described in $(\mathrm{CF})_{i}$ i. e. ${}_{(i)}\tilde{\boldsymbol{r}}^{\mathrm{T}} = \begin{bmatrix} {}_{(i)}\boldsymbol{r}^{\mathrm{T}} & 1 \end{bmatrix}$

Three dimensional Mechanics

${}_{(i)}\boldsymbol{r}_{\mathrm{P}}$	Position vector from origin to point P, described in $(\mathrm{CF})_{i}$
${}_{(i)}\dot{\boldsymbol{r}}_{\mathrm{P}}$	Velocity of point P, described in $(\mathrm{CF})_{i}$
${}_{(i)}\boldsymbol{\omega}_{\mathrm{B}}$	Rotational velocity of body B, described in $(\mathrm{CF})_{i}$
${}_{(i)}\boldsymbol{J}_{\mathrm{B}}^{(\mathrm{P})}$	Rotational inertia matrix of body B regarding point P, described in $(\mathrm{CF})_{i}$, i. e. ${}_{(0)}\boldsymbol{J}_{\mathrm{B}}^{(\mathrm{P})} = {}^{0}\boldsymbol{R}_{i\,(i)}\boldsymbol{J}_{\mathrm{B}}^{(\mathrm{P})}\,({}^{0}\boldsymbol{R}_{i})^{\mathrm{T}}$
m_{i}	Mass of body i
${}_{(0)}\boldsymbol{g}$	Vector of gravity

System Description

$\mathcal{E}_{\mathrm{Tr}}$	Set of parameters, describing the track geometry
$\mathcal{C}_{\mathrm{Tr}}$	Set of parameters, describing the wheel-rail adhesion conditions
$\mathcal{F}_{\mathrm{Train}}$	Set of parameters, describing the interaction between car body and wheel carrier
θ	Combined set of variable parameters, i. e. $\theta = \{\mathcal{E}_{\mathrm{Track}}, \mathcal{C}_{\mathrm{Track}}, \mathcal{F}_{\mathrm{Train}}\}$
$\boldsymbol{f}$, $\boldsymbol{f}_{\mathrm{d}}$	Continuous- and discrete-time system description, respectively
$\boldsymbol{x}$	State vector
$\boldsymbol{u}$	Input vector
τ_{j}	Wheel motor torque
x	Cartesian coordinate in the corresponding frame
y	Cartesian coordinate in the corresponding frame
z	Cartesian coordinate in the corresponding frame
φ	Rotation angle about x-axis (roll angle) in the corresponding frame
ϵ	Rotation angle about y-axis (pitch angle) in the corresponding frame
ψ	Rotation angle about z-axis (yaw angle) in the corresponding frame
$y_{\mathrm{C}j}$	Lateral position of the wheel-rail contact
$r_{\mathrm{C}j}$	Wheel radius at the wheel-rail contact
$\delta_{\mathrm{C}j}$	Contact angle at the wheel-rail contact

$j \in \{\mathrm{ri}, \mathrm{le}\}$

LAGRANGE Formalism

E_T	Kinetic energy
E_V	Potential energy
E_D	Dissipation function
$\mathcal{L}$	LAGRANGIAN
$\boldsymbol{F}_\mathrm{gen}$	Vector of generalized forces and moments
$\boldsymbol{q}$	Vector of generalized coordinates

Integrated Control

$\boldsymbol{Q}_\mathrm{MPC}$, $\boldsymbol{Q}$	State cost weighting of suitable dimension
$\boldsymbol{R}_\mathrm{MPC}$, R	Input cost weighting of suitable dimension
H	Prediction horizon length
T	Discrete prediction horizon time step
L	Discrete prediction steps i. e. $L = H/T$
$\boldsymbol{\mathcal{X}}$	Static state constraints
$\boldsymbol{\mathcal{U}}$	Static input constraints
Δu	Differential control torque, determined by lateral guidance control
u^d	Mean control torque, determined by adhesion-based control
δu	Mean control torque step, determined by adhesion-based control, i. e. $u_k^\mathrm{d} = u_{k-1}^\mathrm{d} + \delta u$

Mathematical Abbreviations

$\|\boldsymbol{v}\|_{\boldsymbol{M}}^2 = \boldsymbol{v}^\mathrm{T}\boldsymbol{M}\boldsymbol{v}$

$\boldsymbol{v}_{[n,m]} = \{\boldsymbol{v}_k\}_{k=n}^m$

1 Introduction

According to climate protection laws in Germany, the emissions of greenhouse gases have to be reduced to 85 million tons of CO_2-equivalents by the year 2030. This is a reduction of 65% compared to the emissions in 1990 [Bun21]. In this light, railway traffic is a forward-looking possibility to cope with the necessary mobility transition. To achieve a significant modal shift, efforts in the entire railway sector are demanded, including infrastructure, train operation, and of course the railway vehicle itself.
The current thesis contributes to the development of a safe, reliable, and efficient rail transport by exploring new concepts for the integrated control of high-speed railway running gears with Independently Rotating Wheels (IRW). In detail, Model Predictive Control (MPC) approaches are investigated.
The work is conducted as part of the initiative Next Generation Train (NGT) of the German Aerospace Center (German: Deutsches Zentrum für Luft- und Raumfahrt e.V. (DLR)) and builds upon existing results of the DLR Institute of System Dynamics and Control (German: Institut für Systemdynamik und Regelungstechnik (SR)). The main part of this thesis is presented in form of a scientific publication, since the control of railway running gears with IRW is an active research area. Introducing context chapters as well as a further description of methods provide a frame for the publication. In the following, the development framework is described in the context of existing literature.

1.1 Development Framework

To start with, the flagship project NGT and the activities of the DLR are briefly described. The motivation to use IRW in railway running gears and for application of MPC are outlined. Lastly, specific objectives for the current thesis are stated.

1.1.1 Next Generation Train

The climate crisis is one of the most urgent challenges of today and insistently demonstrates the necessity for a transition of the mobility sector. Increasing material prices, dependency on international actors, and rising transport volumes exacerbate the problem.
In this context, railway transport can make a contribution to a sustainable and environmentally friendly mobility and should be developed further. To this end, the DLR combines its railway

research activities in the flagship project NGT [Deu22a]. Several institutes of the DLR work towards improvements of operational processes, conceptual train design, and control aspects. As a part of a new and promising running gear concept with IRW, SR conducts research regarding control and estimation in railway vehicles.
Previously, a roller rig of scale 1:5 has been used for verification of the devised techniques. For more realistic experiments and to refine the research further, a full scale prototype of the new running gear will be available in the near future. A picture of the prototype is shown in Fig. 1.1.

1.1.2 Motivation

The use of wheelsets with rigidly coupled wheels has proven its robustness and simplicity for centuries. Its system dynamics have been analyzed thoroughly and design adjustments have led to improved wear figures, ride comfort, and energy consumption. In this process, the basic concept remained untouched.
An interesting design option for railway running gears is to employ IRW instead of commonly used wheelsets. The technique introduces an additional degree of freedom to the system and allows (if actively controlled) to specify the exact lateral position of the running gear in the track. Based on this, wear figures and ride comfort can be improved dramatically. In particular,

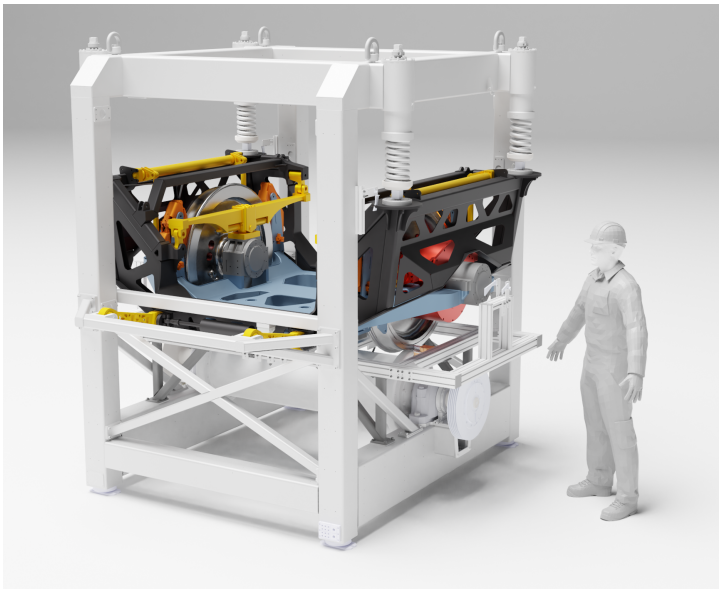

Figure 1.1: Full scale prototype and integration test rig of a running gear with IRW. Primary wheel carrier is shown in blue and secondary suspension frame is shown in black [Deu22b].

undesired slip, and hence wear, in the wheel-rail contacts can be reduced by nearly ideal rolling. Additionally, inevitable wear can be planned actively such that wheels wear off in a uniform fashion and the ”wear reservoir“ is used as effectively as possible.
Further, the omission of the middle axle enables the design of double deck trains with continuous floors on both levels which increases the transportation capacity significantly. Besides, the concept allows for low-floor trains. This advantage is especially striking in the light of the current announcement of Deutsche Bahn (DB) to limit future tenders for their Intercity-Express (ICE) fleet to accessible trains [Tag22].
However, the advantages of a running gear with IRW come at the cost of an increased system complexity. As theoretical and experimental results show, the IRW-system is not stable by itself and further measures must be taken [Iwn06]. The approach of SR is to implement a mechatronic guidance system by actuating and controlling each wheel by a separate motor [Deu22b]. Current results suggest that the mechatronic guidance of a running gear with Driven Independently Rotating Wheels (DIRW) is a possible, but yet a challenging control task [HKG20, GHL19, KHWR14, GLH18, HLGK17]. Difficulties are

- variable and hard to describe system parameters,
- nonlinear system dynamics,
- varying and unknown adhesion conditions between wheels and rails as well as a
- variable path of the track with superimposed irregularities.

Apart from lateral guidance, SR conducts research to improve the longitudinal control of trains. A key concept is the estimation of current adhesion conditions between wheels and rails and the use of this information in an adhesion-based control [SBH19, SK19, SPG21a].
So far, the described control tasks have been treated mostly separately. However, the longitudinal and lateral dynamics of a railway running gear with DIRW are inherently linked and limited by the adhesion conditions in the wheel-rail contacts. Further, the lateral system dynamics are strongly dependent on longitudinal position and velocity of the running gear, as described in the subsequent section 1.2. In this light, the need for an integrated control of the longitudinal and lateral direction becomes apparent.
A modern control technique, which is widely used in research and industry, is MPC. It is an optimization-based method and determines an optimal control input for a (possibly nonlinear) plant by means of a predictive model [Ada18]. MPC concepts have been applied recently for integrated control tasks in the automotive sector [FTA$^+$07, AKJ20, ZRCD15]. In the railway context, however, such techniques have not been implemented so far to the best of the authors knowledge.

The application of MPC for control of railway running gears with IRW is appealing due to the following aspects:

- Complex, nonlinear, and coupled system dynamics can be taken into account easily.
- Preview information about variable disturbances and set-points (such as track geometry, irregularities or desired lateral wheel carrier position in the track) can be considered nicely through the predictive nature of the method.
- Hard constraints can be introduced inside the controller such that states and inputs remain in a feasible operation region and stability is maintained.
- Individual cost functions and weightings can be used to optimize the control objective for different scenarios.

The latter is especially interesting with regard to actuator saturation and the prevention of a too high lateral wheel carrier displacement in the track. In this light, the conceptual working direction of MPC-based integrated control structures is chosen.

1.1.3 Objectives

Following the above general illustration of the research task, specific objectives for the controller and for the current thesis are formulated.
As described in section 1.1.2, MPC techniques have not been used for control of railway running gears with IRW before. In this light, the main focus lies on methodological aspects rather than on a ready-to-use practical implementation. Computation time arguments are considered, but are no immediate exclusion criteria. Furthermore, control-oriented evaluation scenarios are used to scrutinize and compare different concepts. Important performance criteria are the Root Mean Squared Error (RMSE) of the lateral position in the track and the braking distance.
With regard to the NGT background, previously developed models and simulation environments are to be considered and the results of the current thesis should suit into the existing framework. A possible overall control structure of the NGT is shown in Fig. 1.2. Here, the integrated controller to be developed is shown in a conceivable system context. The superimposed train control system is only a schematic and its development is not part of the current work. Further, estimation and observation structures have been researched separately at SR such that these techniques are assumed to be available for the subsequent control design.
As can be seen, each running gear may be controlled by an own local, integrated controller. The controllers could be supplied with information about the track geometry $\mathcal{E}_{\mathrm{Tr}}$ and adhesion conditions $\mathcal{C}_{\mathrm{Tr}}$, if available. Meaningful target values from a superimposed control system would be the desired lateral position in the track y_i^* and the desired longitudinal force $F_{x_i}^*$ at

running gear i. The outputs of the decentralized integrated controllers are the requested motor torques τ_{ij} of the wheel motors, where the index $j \in \{\mathrm{ri}, \mathrm{le}\}$ accounts for the right and left side. For the rest of this thesis, only a single running gear is considered and the index i is omitted. In this context, each integrated controller should:

- take desired lateral displacement y^* and longitudinal force F_x^* as inputs
- provide requested motor torques τ_j as outputs
- ensure stable guidance in the track while working towards the desired values
- ensure stability in the presence of changing adhesion conditions $\mathcal{C}_{\mathrm{Tr}}$
- take into account the track geometry $\mathcal{E}_{\mathrm{Tr}}$ to improve control performance

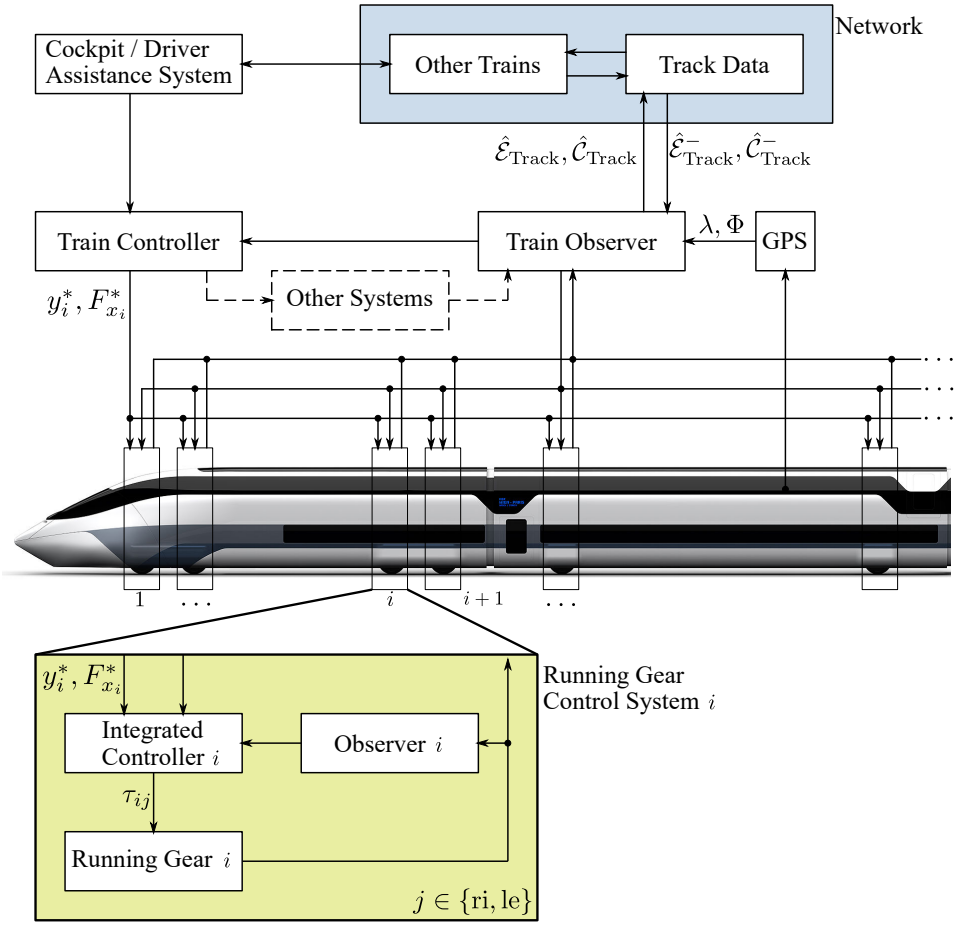

Figure 1.2: Possible control structure of the NGT with decentralized, integrated running gear controllers (Train figure adjusted from: DLR, CC-BY 3.0). *A priori* knowledge is denoted $\square^-$. Estimated quantities are denoted $\hat{\square}$.

1.2 System Analysis and Approach

To find a suitable basis approach for the current work, a first system analysis of a running gear with IRW is carried out. To do so, a schematic overview of the IRW-system is shown in Fig. 1.3. It is worth mentioning, that the figure is designed in a control-oriented fashion with focus on system inputs and outputs.
Starting at the top level, the running gear to be controlled is located inside the train plant, where it is attached to a secondary suspension frame (see also Fig. 1.1). The secondary suspension frame itself is linked to the main body (i. e. the car body) of the train. Due to the secondary suspension stage, most high frequency forces between car body and primary wheel carrier are canceled. Nonetheless, low frequency forces due to inertia and curving are transmitted to the primary wheel carrier. Therefore, the train forces are described by slowly varying parameters $\mathcal{F}_{\mathrm{Train}}$ in this work.
At ground level, the connections between running gear and track are located in the wheel-rail contacts. The occurring forces are strongly dependent on the current driving state, the wear-influenced nonlinear wheel and rail profiles, the adhesion conditions $\mathcal{C}_{\mathrm{Tr}}$, and the geometry of the track $\mathcal{E}_{\mathrm{Tr}}$, including construction-related irregularities. In this thesis, the track geometry is assumed to be known and is described by variable parameters which depend on the track coordinate s. The adhesion conditions are considered sets of time- and space-varying parameters

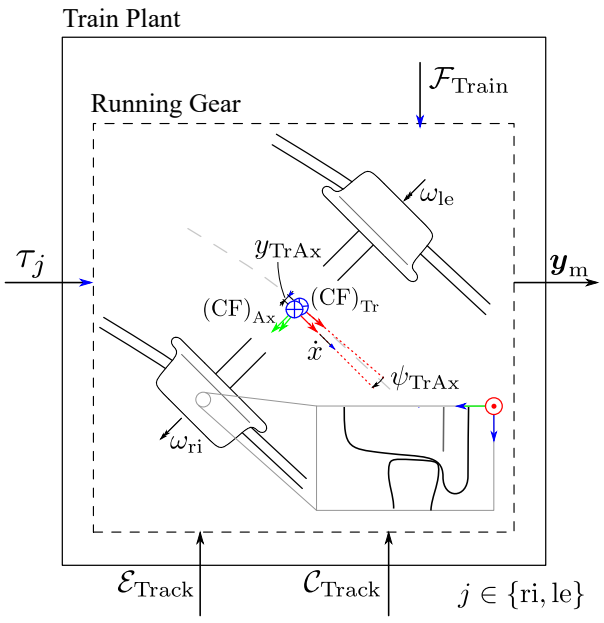

Figure 1.3: Control-oriented system overview of a wheel carrier with IRW. Excerpt of the contact geometries.

for each rail side which are *a priori* unknown. The control inputs are the demanded motor torques τ_j of the right and the left wheel motor.
In subsequent chapters, the LAGRANGE formalism is applied to the system. Thus, generalized coordinates are introduced for the system description. A possible choice of generalized coordinates is shown in Fig. 1.3, featuring longitudinal and lateral coordinate x and y, yaw angle ψ, and the rotation of both wheels independent of each other ω_j. Outputs which can be measured by means of currently available on-board equipment are the wheel speeds ω_j and the yaw rate $\dot{\psi}$. However, powerful observers have been designed at SR such that a full state availability is assumed in the current thesis [KSM19, KSM+21].
For description of lateral guidance and track path following, different Coordinate Frames (CF) are defined. Two important frames are the track frame $(\mathrm{CF})_{\mathrm{Tr}}$ and the axle frame $(\mathrm{CF})_{\mathrm{Ax}}$. The track frame is located at the current track position of the running gear. Its x-axis is aligned with the track center line and its y-axis lies in the track plane between left and right rail. The origin of the axle frame $(\mathrm{CF})_{\mathrm{Ax}}$ is centered between right and left wheel and its x-axis points into the current driving direction. In this thesis, the yaw angle of $(\mathrm{CF})_{\mathrm{Ax}}$ with respect to $(\mathrm{CF})_{\mathrm{Tr}}$ is denoted ${}_{(\mathrm{Tr})}\psi_{\mathrm{Ax}}$. The corresponding relative lateral position is ${}_{(\mathrm{Tr})}y_{\mathrm{Ax}}$. For convenience, the notation is relaxed in the scientific publication, i. e. ${}_{(\mathrm{Tr})}\psi_{\mathrm{Ax}} = \psi_{\mathrm{TrAx}}$ and ${}_{(\mathrm{Tr})}y_{\mathrm{Ax}} = y_{\mathrm{TrAx}}$.
To sum up, the system may be described by the following state space formulation:

$$\dot{\boldsymbol{x}} = \boldsymbol{f}\left(\boldsymbol{x}, \boldsymbol{u}, \theta\right),$$

with generalized coordinates	$\dot{\boldsymbol{q}}^{\mathrm{T}} = \left[\dot{x}, \dot{y}, \dot{\psi}, \omega_{\mathrm{ri}}, \omega_{\mathrm{le}}\right],$
state vector	$\boldsymbol{x}^{\mathrm{T}} = \left[\boldsymbol{q}^{\mathrm{T}}, \dot{\boldsymbol{q}}^{\mathrm{T}}\right],$
control inputs	$\boldsymbol{u}^{\mathrm{T}} = \left[\tau_{\mathrm{ri}}, \tau_{\mathrm{le}}\right],$
and varying parameters	$\theta = \left\{\mathcal{E}_{\mathrm{Tr}}, \mathcal{C}_{\mathrm{Tr}}, \mathcal{F}_{\mathrm{Train}}\right\},$
	$\mathcal{E}_{\mathrm{Tr}} = g\left(s\right),$
	$\mathcal{C}_{\mathrm{Tr}} = h\left(s, j, t\right),$
	$\mathcal{F}_{\mathrm{Train}} = f\left(\mathcal{E}_{\mathrm{Tr}}, \mathcal{C}_{\mathrm{Tr}}, t\right), \qquad j \in \left\{\mathrm{ri}, \mathrm{le}\right\}.$

In this context, a complex system with highly coupled and nonlinear dynamics is to be controlled. Additionally, preview information about the track geometry is assumed to be available and may be used. In this light, the application of MPC schemes appears to be an appropriate choice and will be a main research direction of the current work.

2 Literature Review

An extensive literature review is performed in order to devise a suitable integrated control system. First, key features of the running gear are reviewed in the context of existing research results for running gear control. Subsequently, possible control methodologies in terms of integrated and model predictive control are briefly illustrated.

2.1 Wheel-Rail Contacts

The conditions in the wheel-rail contacts are of crucial importance for a successful development of a model-based integrated controller. For instance, the adhesion conditions determine the maximum force that can be transferred between wheel and rail both, in lateral and longitudinal direction. Another relevant aspect is the continuously changing position of the contact point at which forces work and which influences the system dynamics. Therefore, the influences on the contact points will be reviewed in the following.
The traction, braking, and steering forces of each running gear occur in the wheel-rail contacts. The contacts can be described by their current size, position, shape, and adhesion conditions. The main influences on these quantities are the momentary position and orientation of the wheel carrier with respect to the track, the nonlinear and wear-dependent wheel and rail-profiles, the contact forces, material properties, and the condition of the surfaces. An example for usual wheel and rail profiles can be seen in Fig. 1.3.
As a consequence, it is difficult to describe wheel-rail contacts in detail. Usually, an extensive simulation is performed in combination with a full-vehicle simulation (e. g. in the Multi-Body Simulation (MBS) tool SIMPACK) and with the aid of simplifying models and assumptions. The contact area itself, for instance, is usually modeled elliptically on basis of HERTZIAN theory [Iwn06].
Different models are available for characterization of the adhesion conditions. The core of these models is the relationship between slip (longitudinal, lateral, and spin creepage) and resulting contact forces. For a basic understanding, possible relationships between adhesion and slip are shown in Fig. 2.1 for a single dimension. In terms of accuracy, the program CONTACT, developed by Kalker, is a well known and widely used benchmark. However, in comparison to other methods, it is computationally demanding [GK90]. An efficient alternative for small slip values is the linear theory of Kalker or the algorithm FASTSIM [Kal82]. A computationally

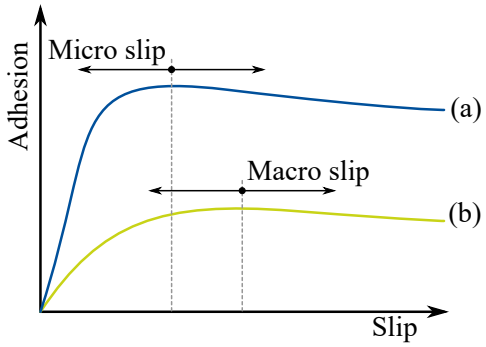

Figure 2.1: Schematic adhesion-slip with good (a) and bad (b) adhesion conditions.

tractable, yet accurate model for a wide range of slip values is the Polach model which is briefly reiterated here on basis of [Pol99, Pol05]. Since the considerations regarding the rail-wheel contacts are similar for the right and left side, the subscripts $j \in \{\mathrm{ri}, \mathrm{le}\}$ are omitted in this section for simplicity.
Due to its computational efficiency and its applicability to both micro and macro slip regimes, the Polach model is often used in MBS software. It sets longitudinal, lateral, and spin creepage in a relationship to the creep forces F_x and F_y in longitudinal and lateral direction, respectively. In detail, the total tangential force F_T in the wheel-rail contact is approximated by

$$F_\mathrm{T} = \int\int_A p_\mathrm{T}\,\mathrm{d}x\mathrm{d}y \approx -\frac{2Q\mu}{\pi}\left(\frac{\epsilon_\mathrm{T}}{1+\epsilon_\mathrm{T}^2} + \arctan\left(\epsilon_\mathrm{T}\right)\right), \tag{2.1}$$

where A is the contact area, p_T is the tangential stress in the contact area, Q is the wheel load, μ is the friction coefficient and ϵ_T is the gradient of the tangential stress. The latter is a central ingredient for the model and can be determined by

$$\epsilon_\mathrm{T} = \frac{2}{3}\frac{C\pi a^2 b}{Q\mu}s, \tag{2.2}$$

with C being a proportionality constant and a and b being the half axes of the contact ellipse. The total slip s obeys $s = \sqrt{s_x^2 + s_y^2}$ and determines the directional adhesion

$$f_i = \frac{F_i}{F_\mathrm{N}} = \frac{F}{F_\mathrm{N}}\frac{s_i}{s}, \qquad i \in \{x, y\}\,. \tag{2.3}$$

For combination of the influences of lateral slip s_y, and spin creepage Ψ, the extensions

$$s_{y\mathrm{C}} = \begin{cases} s_y + \Psi a, & \text{for } |s_y + \Psi a| > |s_y| \\ s_y, & \text{otherwise,} \end{cases} \tag{2.4}$$

$$F_{y\mathrm{C}} = F_y + F_{y\mathrm{S}}, \tag{2.5}$$

are introduced with a suitable definition for $F_{y\mathrm{S}}$ which can be found in [Pol99]. To account for both, micro and macro slip regime, further terms are added.
First, the underlying friction coefficient can be formulated exponentially dependent on the total slip velocity w with

$$\mu = \mu_0 \left((1 - A)\, \mathrm{e}^{-Bw} + A \right), \tag{2.6}$$

$$w == s\dot{x}. \tag{2.7}$$

B is the factor of exponential friction decrease and $A = \mu_\infty / \mu_0$ is the ratio between limit friction coefficient for an infinite slip velocity and maximum friction coefficient at $w = 0$.
Second, reduction factors k_A and k_S account for different slopes of the adhesion-slip characteristic in the micro and the macro slip regime, respectively [Pol05]. Therefore, (2.1) becomes

$$F_\mathrm{T} \approx \frac{2Q\mu}{\pi} \left(\frac{k_\mathrm{A} \epsilon_\mathrm{T}}{1 + (k_\mathrm{A} \epsilon_\mathrm{T})^2} + \arctan\left(k_\mathrm{S} \epsilon_\mathrm{T}\right) \right). \tag{2.8}$$

The coupled dependence of the adhesion in longitudinal and lateral direction on the slip values can be well illustrated by the multidimensional adhesion-slip diagrams in Fig. 2.2. In this context, an adhesion-slip characteristic in Fig. 2.1 could be a slice of Fig. 2.2 along a single

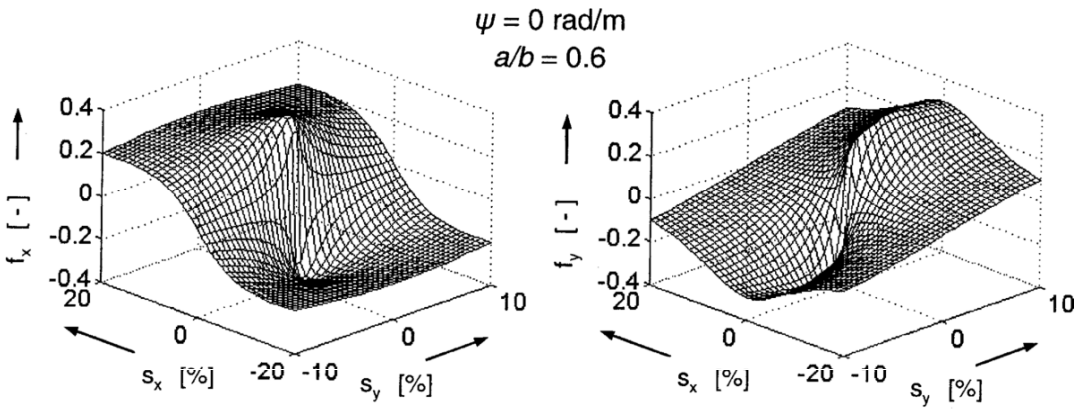

Figure 2.2: Polach model for different spin slip values (excerpt from [Pol05]).

dimension. From (2.4) it is easy to see, that $\Psi \neq 0$ increases the combined lateral slip. Thus, the adhesion maximum in longitudinal direction (see Fig. 2.2) is reduced if $\Psi \neq 0$ [Pol99]. However, due to the wheel conicity, some spin creepage does always occur.

2.2 Control in Railway Running Gears

Traditional railway running gears with solid axle wheelsets have inherent stability properties within a certain configuration specific velocity range. A locus diagram of a linearized freely running wheelset system is shown in Fig. 2.3 which illustrates the velocity-dependent position of the poles. As can be seen, the freely running wheelset shows a stable oscillation which increases in frequency if the velocity rises. Eventually the oscillation becomes unstable if a certain critical velocity is exceeded [DA12]. If damping and springs are introduced, the oscillatory motion can be mitigated. The sinusoidal motion is known as the hunting motion of the free wheelset and its frequency was first described by Klingel in 1883 [Kli83].
In modern railway systems, the desire to perform active steering has increased in the last decades due to the previously mentioned advantages. There exist different possibilities to achieve improved curving. One approach that allows for perfect curving is the use of running gears with IRW [GBM06]. Corresponding control strategies can be based on H_∞ control, where stabilization and guidance is robustly achieved in the presence of parameter variations

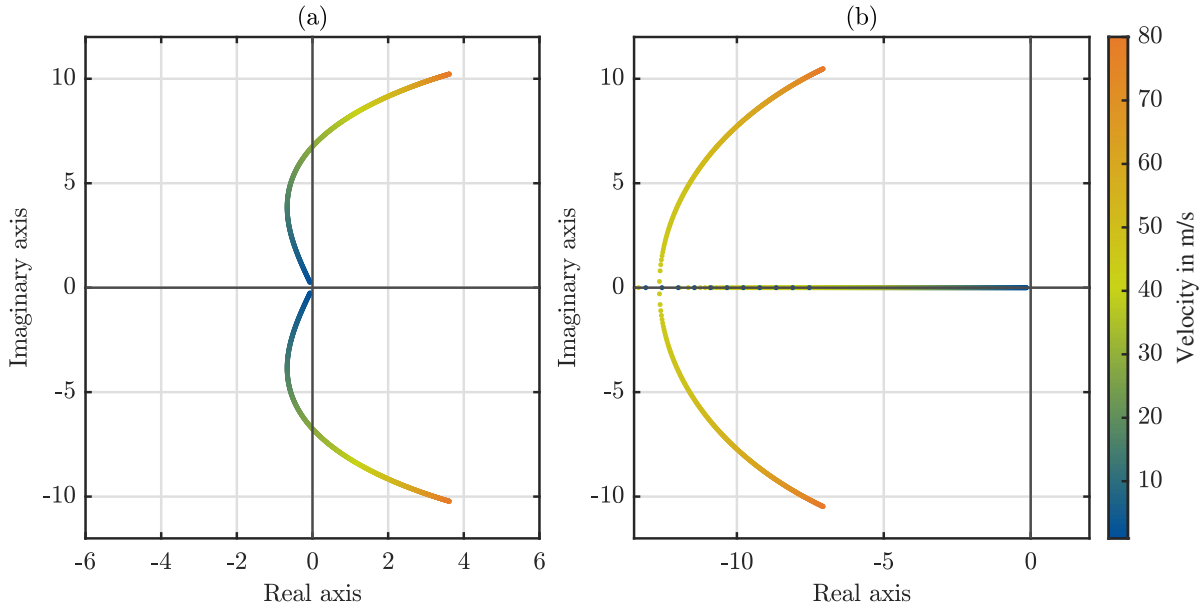

Figure 2.3: Locus diagram of a freely running (a) and a damped and spring loaded (b) solid axle wheelset.

[MG01]. Other studies employed gain scheduled state feedback controllers due to the strongly velocity dependent lateral dynamics [MG03]. Additional physically motivated feed forward control signals can improve the performance further and a parameter space approach has been used to ensure robustness despite the nonlinear wheel-rail profiles [HSB$^+$15, HLGK17]. Since the running gear with IRW shows strongly nonlinear behavior, an advanced control strategy such as feedback linearization is a suitable choice as well [GLH18, GHL19, HKG20].
The longitudinal control is relevant for all railway systems and not only for running gears with IRW. Here, a research emphasis lies on the improvement of braking systems and hence the reduction of braking distances. In this context, some groups focus on a slip-based longitudinal control. These methods depend on a desired slip area in which the best braking performance (i. e. the maximum adhesion) is assumed to be [LK16, SEEA08]. However, adhesion conditions between wheels and rails are strongly variable and dependent on environmental influences. Hence, the maximum of the adhesion-slip characteristic is achieved at changing slip values. A possibility to overcome this problem is the application of maximum-seeking controllers. An example which is based on a sliding mode approach is shown in [SPG21a, SPG21b]. Crucial for this concept is the availability of current and reliable slip and adhesion estimates. In the example, the estimates were obtained from an Extended Kalman Filter (EKF) [SK20].
The previously developed controllers of SR are used as a comparison for the results of the current work. For completeness, the main ideas of the gain scheduled state feedback controller [HSB$^+$15, HLGK17] and the controller based on feedback linearization [GLH18, GHL19, HKG20] are shortly presented here. For a more detailed explanation, the reader is referred to the corresponding publications.
For state feedback control, the running gear system is analyzed thoroughly in terms of its lateral dynamics. The velocity is considered a slowly varying model parameter v_R. Assumptions such as ideal rolling and neglect of lateral wheel slip lead to a simplified and linearized system model with three states $\boldsymbol{x}^{\mathrm{T}} = \begin{bmatrix} y & \psi & \dot{\psi} \end{bmatrix}$. For these states, a feedback control law

$$u_j = \pm u_{\mathrm{lat}}, \qquad j \in \{\mathrm{ri}, \mathrm{le}\}\,, \tag{2.9}$$

$$u_{\mathrm{lat}} = \begin{bmatrix} k_y(v_R) & k_\psi(v_R) & k_{\dot{\psi}}(v_R) \end{bmatrix} \boldsymbol{x} \tag{2.10}$$

is devised with k_y, k_ψ and $k_{\dot{\psi}}$ being velocity-scheduled controller gains. The scheduling rule is found by a parameter space approach. In this method, a desired region in which the model poles ought to be is defined in the complex plane. The region boundaries are mapped onto the model and control parameter space by means of symbolic calculations. There, it is straightforward to find controller gain scheduling laws for the considered operation region of model parameters. In [HSB$^+$15, HLGK17], variable model parameters are the velocity v_R and the wheel conicity d.

The devised feedback linearization control for running gears is also based on the assumption of ideal rolling. A basic model of the nonlinear lateral running gear dynamics with the state space representation

$$\dot{\boldsymbol{x}} = \begin{bmatrix} \dot{y} \\ \dot{\psi} \\ \ddot{\psi} \end{bmatrix} = \begin{bmatrix} f_1(\boldsymbol{x}) \\ \dot{\psi} \\ f_2(\boldsymbol{x}, u_{\mathrm{lat}}) \end{bmatrix}, \tag{2.11}$$

is derived. Suitable assumptions lead to a model whose states successively depend on each other, i. e. $f_1(\boldsymbol{x}) \rightarrow f_1(\psi)$. Hence, a cascaded control structure in the sense of a Nonlinear Dynamic Inversion (NDI) [DG08] can be set up to track the set points y^*, ψ^* and $\dot{\psi}^*$ as shown in Fig. 2.4. Appropriate feedback gains are applied to the control errors

$$e_y = y^* - y, \tag{2.12}$$

$$e_\psi = \psi^* - \psi, \tag{2.13}$$

$$e_{\dot{\psi}} = \dot{\psi}^* - \dot{\psi}, \tag{2.14}$$

inside the inversion blocks f_1^{-1} and f_2^{-1}. More detailed inverse dynamics and gain scheduled feedback gains have lead to further improved control performance. Besides, track related information is employed in a more sophisticated inversion model to tackle the influence of gyroscopic effects, track irregularities, and centripetal as well as gravitational acceleration [GHL19].

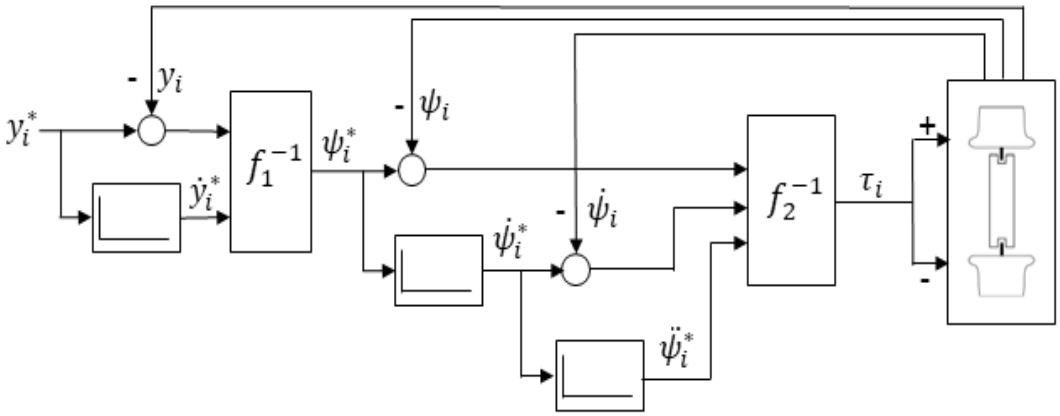

Figure 2.4: NDI scheme for lateral guidance of running gears with IRW (excerpt from [HKG20]).

2.3 Integrated Control

Integrated control in general describes the mastering of two or more control tasks in a single control system. In the vehicle context, the literature is dominated by contributions regarding the automotive sector. In this area, integrated control is understood as the goal-oriented combination of several subsystems in a road vehicle. Only some examples of these are the Electronic Stability Control (ESC), the Anti-Lock Brake System (ABS) and the Active Suspension System (ASS). The co-existing (Single Input Single Output (SISO)) control loops act together on a coupled system. The result may be practicable if the cross-coupling between the control loops are weak, but the result is suboptimal [ST10]. This control structure is known as a ”Decentralized Control“ [GHB03].
Integrated controllers aim to orchestrate the operation of the subsystems such that negative interactions are mitigated or even positive synergies are created. To achieve this, different integration strategies can be employed. On the one hand, the subsystems themselves may remain unchanged. In this case, either the inputs to the subsystems or the outputs from the subsystems can be adjusted and recombined by an integrated controller with regard to the current driving situation. This configuration is called ”Supervisory Control“ [GHB03].
On the other hand, the combination of all subsystem functionalities into one controller is possible, leading to a ”Centralized“ integration approach. Following this line, the several SISO control loops are put together to a Multiple Input Multiple Output (MIMO) system of significant complexity. For the automotive context this is known as Global Chassis Control (GCC) [ST10].
In the context of lateral and longitudinal control of vehicles, integrated controllers have an outstanding importance. First, lateral and longitudinal system dynamics are strongly coupled in traditional vehicles with non-holonomic properties, i. e. , the lateral degree of freedom cannot be controlled independently but only in combination with longitudinal velocity and a nonzero yaw angle. Second, lateral guidance, longitudinal traction, and braking are provided both by the contacts between wheels and underground and are limited by the current adhesion conditions. If the combined lateral and longitudinal adhesion exceeds the maximum possible adhesion in a contact, extensive slip and hence instability occurs. For automotive systems, many examples for successful implementations of such integrated longitudinal and lateral controllers can be found in literature. A popular methodology is the application of MPC [FTA$^+$07, AKJ20, ZRCD15].
Regarding the integrated control of railway running gears with IRW, only first attempts have been made so far. In [GB02] and [PBMV04], a decentralized integration approach is applied. A differential torque determined by a lateral guidance controller is added to a superimposed longitudinal traction or braking torque. A similar integration strategy, but with more sophisticated subsystem controllers is used in other contributions [FLG08, LSY17]. All presented methods suffer from the fact, that a fixed allocation of torques is needed for both subsystems

in order to comply with the actuator saturation. As an example, the lateral controller does not require the complete allocated torque while riding on a straight track with few irregularities. If the emergency break is applied in this scenario, only the amount of torque allocated to the longitudinal controller can be used for braking even if more motor torque could be provided. A possible solution is the introduction of a supervised integration strategy in the form of a variable allocation rule. This technique has been proposed in [SG22] and can reduce the braking distance in the presented scenario by almost 5%.
To conclude, the integrated longitudinal and lateral control of railway running gears with IRW in critical as well as regular adhesion conditions is an open research question. The topic will be approached by means of MPC techniques in following chapters. Thus a short introduction to MPC is given subsequently.

2.4 Model Predictive Control

The basic ideas and concepts of MPC are briefly reiterated here by means of a specific example. Please note, that other cost functions and method variations can be chosen. For a more detailed explanation, the reader is referred to the corresponding literature.
In MPC, a cost function associated with the difference between the predicted states $\bar{\boldsymbol{x}}$ and the desired target states $\boldsymbol{x}^{\mathrm{d}}$ is minimized along the predicted control inputs $\bar{\boldsymbol{u}}$ over a prediction horizon. In the optimization problem, dynamic constraints are imposed such that the predicted states and inputs obey the dynamics of an assumed system model $\boldsymbol{f}$. Static constraints $\boldsymbol{\mathcal{X}}$ and $\boldsymbol{\mathcal{U}}$ on states and inputs can be introduced, respectively [Ada18, GAD16, MTD+10].
The first part of the found optimal control input $\bar{\boldsymbol{u}}(\tau_{\mathrm{opt}})^*$ is applied to the plant and the optimization problem is solved again with current measured initial states $\boldsymbol{x}_{t,\mathrm{meas}}$ [GAD16]. The general optimization problem with state cost matrix $\boldsymbol{Q}_{\mathrm{MPC}}$ and input cost matrix $\boldsymbol{R}_{\mathrm{MPC}}$ reads

$$\bar{\boldsymbol{u}}(\tau_{\mathrm{opt}})^* = \arg\min_{\bar{\boldsymbol{u}}(\tau_{\mathrm{opt}})} \int_t^{\infty} \left\|\bar{\boldsymbol{x}}(\tau_{\mathrm{opt}}) - \boldsymbol{x}^{\mathrm{d}}(\tau_{\mathrm{opt}})\right\|^2_{\boldsymbol{Q}_{\mathrm{MPC}}} + \left\|\bar{\boldsymbol{u}}(\tau_{\mathrm{opt}})\right\|^2_{\boldsymbol{R}_{\mathrm{MPC}}} \mathrm{d}\tau_{\mathrm{opt}} \tag{2.15a}$$

$$\text{s.t. } \dot{\bar{\boldsymbol{x}}}(\tau_{\mathrm{opt}}) = \boldsymbol{f}\left(\bar{\boldsymbol{x}}(\tau_{\mathrm{opt}}), \bar{\boldsymbol{u}}(\tau_{\mathrm{opt}})\right), \tag{2.15b}$$

$$\bar{\boldsymbol{x}}(t) = \boldsymbol{x}_{t,\mathrm{meas}}, \tag{2.15c}$$

$$\bar{\boldsymbol{u}}(\tau_{\mathrm{opt}}) \in \boldsymbol{\mathcal{U}}, \tag{2.15d}$$

$$\bar{\boldsymbol{x}}(\tau_{\mathrm{opt}}) \in \boldsymbol{\mathcal{X}}, \qquad \forall \tau_{\mathrm{opt}} \in [t, \infty). \tag{2.15e}$$

However, an actual implementation of the above algorithm is not possible. On the one hand, the infinitely long prediction horizon cannot be imposed in practice. Therefore, the optimization problem is solved for a truncated prediction horizon H and an additional, mostly additive, term J_{term} is introduced to approximate the truncated tail of the cost function [GAD16]. On the

other hand, an implementation on digital computers requires a discrete time formulation. To do so, appropriate discretization techniques such as a 4^{th}-order Runge-Kutta method can be used, introducing the time step width T. Hence, the prediction horizon is divided in $L = H/T$ discrete steps. An implementable version of the above algorithm is shown below.

$$\bar{\boldsymbol{u}}^*_{[0,L-1]}(t) = \arg\min_{\bar{\boldsymbol{u}}_{[0,L-1]}(t)} \sum_{k=0}^{L-1} T \left\| \bar{\boldsymbol{x}}_k(t) - \boldsymbol{x}^{\mathrm{d}}_k(t) \right\|^2_{\boldsymbol{Q}_{\mathrm{MPC}}} + T \left\| \bar{\boldsymbol{u}}_k(t) \right\|^2_{\boldsymbol{R}_{\mathrm{MPC}}} + J_{\mathrm{term}} \tag{2.16a}$$

$$\text{s.t. } \bar{\boldsymbol{x}}_{k+1}(t) = \boldsymbol{f}_{\mathrm{d}}\left(\bar{\boldsymbol{x}}_k(t), \bar{\boldsymbol{u}}_k(t)\right), \qquad \forall k \in [0, L-1], \tag{2.16b}$$

$$\bar{\boldsymbol{x}}_0(t) = \boldsymbol{x}_{t,\mathrm{meas}}, \tag{2.16c}$$

$$\bar{\boldsymbol{u}}_{[0,L-1]}(t) \in \boldsymbol{\mathcal{U}}, \tag{2.16d}$$

$$\bar{\boldsymbol{x}}_{[0,L]}(t) \in \boldsymbol{\mathcal{X}}. \tag{2.16e}$$

Please note, the above MPC problems are introduced in general terms. A formulation specific for the current control task can be found in chapter 3.

3 Publication

The current thesis deals with the integrated longitudinal and lateral control of railway running gears with IRW. The controller to be developed may use previously available information about the track geometry and should be robust against changing and unknown adhesion conditions between wheels and rails. In this context, an MPC approach has been employed.
Since the integrated control of railway running gears with IRW is a current research topic, the main part of this thesis is presented as a scientific publication. Used methods and additional work which could not be presented in the publication are illustrated in more detail in a following chapter. Lastly, a conclusion and discussion for the current thesis is given.

The subsequently presented scientific publication carries the title

Integrated Model Predictive Control of High-Speed Railway Running Gears with Driven Independently Rotating Wheels.

Integrated Model Predictive Control of High-Speed Railway Running Gears with Driven Independently Rotating Wheels

Jan-Hendrik Ewering, Christoph Schwarz, Simon F. G. Ehlers, and Hans-Georg Jacob

***Abstract*—Railway running gears with Independently Rotating Wheels (IRW) can significantly improve wear figures, comfort, and safety of railway running gears, but certain measures for wheelset stabilization are required. This is one reason why application of traditional wheelsets is still common practice in industry. Apart from lateral guidance, the longitudinal control is of crucial importance for railway safety.**

In the current contribution, an integrated controller for joined lateral and longitudinal control of a high-speed railway running gear with IRW is designed. To this end, a novel adhesion-based traction control law is combined with Linear Time-Variant (LTV) and nonlinear Model Predictive Control (MPC) schemes for lateral guidance. The MPC schemes are able to use tabulated track geometry data and preview information about set points to minimize the lateral displacement error.

Co-simulation results with a detailed Multi-Body Simulation (MBS) show the effectiveness of the approach compared with state-of-the-art techniques in various scenarios, including curving, changing velocities up to 400 km/h and abruptly changing wheel-rail adhesion conditions.

***Index Terms*—Model predictive control, integrated control, adhesion control, railway vehicle dynamics, independently rotating wheels**

I. Introduction

THE climate crisis is one of the most urgent challenges of today and insistently demonstrates the necessity for a transition of the mobility sector. Increasing material prices, dependency on international actors, and rising transport volumes exacerbate the problem.

In this context, railway transport can make a contribution to a sustainable and environmentally friendly mobility and should be developed further. An interesting design option for railway running gears is to employ Independently Rotating Wheels (IRW) instead of commonly used wheelsets. IRW introduce an additional degree of freedom to the system and allow (if actively controlled) to specify the exact lateral position of the running gear in the track. Based on this, wear figures and ride comfort can be improved dramatically [1]. In particular, undesired slip in the wheel-rail contacts, and hence wear, can be reduced by nearly ideal rolling. Further, the omission of the middle axle allows for new train designs such as low-floor or double deck trains with continuous floors on both levels which has implications for effectiveness and accessibility.

In this context, the German Aerospace Center (DLR) conducts railway research as part of the project Next Generation Train (NGT) which aims towards the development of a future train concept. In detail, the train is equipped with distributed drives in each running gear which are holistically controlled. At the lowest level, each running gear with IRW should robustly perform mechatronic guidance and slip prevention independently from higher control levels.

Multiple control strategies for running gears with IRW have been devised, some of which are based on H_∞ control, where stabilization and guidance is robustly achieved in the presence of parameter variations [2]. Other studies employed gain scheduled state-space controllers due to the strongly velocity dependent lateral dynamics [3]. Additional physically motivated feed forward control signals can further improve the performance and a parameter space approach has been used to ensure robustness despite the nonlinear wheel and rail profiles [4, 5]. Since the running gear with IRW shows strongly nonlinear behavior, an advanced control strategy, such as feedback linearization, is a suitable choice as well [6, 7].

In longitudinal control, a research emphasis lies on the reduction of braking distances. In this context, some groups focus on slip-based longitudinal control. These methods depend on a desired slip area in which the best braking performance (i. e. the maximum adhesion) is assumed to be [8, 9]. However, adhesion conditions between wheels and rails are highly variable and dependent on environmental influences. Hence, the maximum of the adhesion-slip characteristic is achieved at changing slip values. A possibility to overcome this problem is the application of maximum-seeking controllers. An example which is based on a sliding mode approach is shown in [10, 11]. Crucial for this concept is the availability of current and reliable slip and adhesion estimates. In the example, the estimates were obtained from an Extended Kalman Filter (EKF) [12].

In the context of combined lateral and longitudinal control, an integration approach is required. First, lateral and longitudinal system dynamics are inherently coupled in traditional vehicles with non-holonomic properties. Second, lateral guidance and longitudinal traction or braking forces are all adhesion-dependent and occur in the contacts between wheels and underground. Therefore, they are limited by the current

Manuscript received []; revised []; accepted []. Date of publication []; date of current version []. The review of this article was coordinated by []. *(Corresponding author: Jan-Hendrik Ewering.)*

Jan-Hendrik Ewering, Simon Ehlers, and Hans-Georg Jacob are with the Institute of Mechatronic Systems, Leibniz Universität Hannover, 30167 Hanover, Germany (e-mail: jan-hendrik.ewering@stud.uni-hannover.de).

Christoph Schwarz is with the Institute of System Dynamics and Control, German Aerospace Center (DLR), 82234 Wessling, Germany (e-mail: christoph.schwarz@dlr.de).

Digital Object Identifier []

adhesion conditions. If the combined lateral and longitudinal adhesion exceeds the maximum possible adhesion in a contact, extensive slip and hence instability occurs. For automotive systems, many examples for successful implementations of such integrated longitudinal and lateral controllers can be found in literature. A popular methodological choice is the application of Model Predictive Control (MPC) where an optimization problem is solved repetitively to determine the optimal control input on basis of a predictive plant model [13]–[15].

Regarding the integrated control of railway running gears with IRW, only first attempts have been made so far. In [16] and [17], a differential torque determined by a lateral guidance controller was added to a superimposed longitudinal traction or braking torque. This integration approach can be considered a decentralized overall control system [18]. A similar integration strategy, but with more sophisticated subsystem controllers was used in other contributions [19, 20]. All presented methods suffer from the fact, that a fixed allocation of torques is needed for both subsystems in order to comply with the actuator saturation. As an example, the lateral controller does not require the complete allocated torque while riding on a straight track with few irregularities. If the emergency break is applied in this scenario, only the amount of torque allocated to the longitudinal controller can be used for braking even if more motor torque could be provided. A possible solution is the introduction of a supervised integration strategy in the form of a variable allocation rule. This technique has been proposed in [21] and can reduce the braking distance in the presented simulation scenario by almost 5%.

To the best of the authors knowledge, MPC has not been used for control of railway running gears with IRW so far. However, its the application is appealing since,

- nonlinear and coupled system dynamics can be employed,
- preview information about track geometry and set-points can be considered in the prediction horizon,
- individual cost functions and weightings can be used to adjust the control objective for different scenarios.

In this light, we contribute an MPC scheme for control of running gears with IRW. Linear Time-Variant Model Predictive Control (LTV-MPC) and Nonlinear Model Predictive Control (NMPC) techniques are presented and compared. Further, we contribute a novel adhesion controller for reliable operation without knowledge of the exact adhesion-slip characteristic. It is able to handle both, regular and critical riding conditions. To combine the novel subsystem controllers, a supervised integration approach is employed as in [21]. Thus, a holistic control framework for joined longitudinal and lateral control of railway running gears with IRW is presented.

In section II, the running gear system is introduced and modeled with regard to the control context. The control synthesis is outlined in section III before experimental results of a co-simulation with a detailed Multi-Body Simulation (MBS) are presented in section IV. The control scheme of [6, 22], which is based on feedback linearization, is given as a comparison. Lastly, a discussion and an outlook is given in section V.

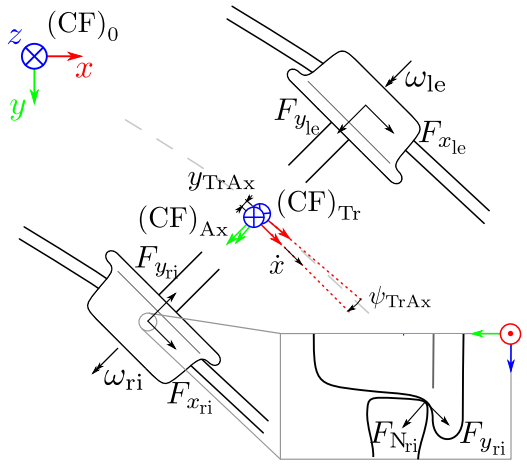

Fig. 1. System overview of a railway running gear with IRW.

II. Modeling

To start with, the running gear system is introduced. Relevant variables and frames are described and the modeling of the track is explained in order to create a framework to handle preview information. For use in MPC, a simplified system model is derived.

A. System Description

The dynamics of a running gear system with IRW have been analyzed thoroughly in the past, see [1, 23]. Only the main influences on the system are described here for brevity and in order to provide a background for the subsequent control model. A system overview with relevant Coordinate Frames (CF) can be found in Fig. 1.

Regarding the track representation, an ideal railway track can be described in terms of the path of its center line together with information about the twist of the track plane. In the current contribution, the track geometry $\mathcal{E}_{\mathrm{Tr}}$ will be characterized by its orientation of the track frame $(\mathrm{CF})_{\mathrm{Tr}}$ at the current coordinate along the ideal track path s with respect to the world frame $(\mathrm{CF})_0$. Curvatures are obtained by differentiation along s. Together with the current running velocity $\dot{x}$, the momentary rotation rates of the track can be determined, i. e.

$$\text{Absolute curve angle} \qquad \psi_{\mathrm{Tr}}(s), \tag{1a}$$

$$\text{Absolute curve rate} \qquad \dot{\psi}_{\mathrm{Tr}}(s,\dot{x}) = \left.\frac{\partial \psi_{\mathrm{Tr}}}{\partial s}\right|_s \dot{x}, \tag{1b}$$

$$\text{Superelevation angle} \qquad \varphi_{\mathrm{Tr}}(s), \tag{1c}$$

$$\text{Superelevation rate} \qquad \dot{\varphi}_{\mathrm{Tr}}(s,\dot{x}) = \left.\frac{\partial \varphi_{\mathrm{Tr}}}{\partial s}\right|_s \dot{x}, \tag{1d}$$

$$\text{Inclination angle} \qquad \epsilon_{\mathrm{Tr}}(s), \tag{1e}$$

$$\text{Inclination rate} \qquad \dot{\epsilon}_{\mathrm{Tr}}(s,\dot{x}) = \left.\frac{\partial \epsilon_{\mathrm{Tr}}}{\partial s}\right|_s \dot{x}. \tag{1f}$$

The corresponding track irregularities occur superimposed to the ideal track path and can be described by s-dependent functions as well.

For description of the running gear, the generalized coordinates

$\dot{\boldsymbol{q}}^{\mathrm{T}} = \left[\dot{x}, \dot{y}, \dot{\psi}, \omega_j\right]$ can be used which are defined in the axle body frame $(\mathrm{CF})_{\mathrm{Ax}}$. The subscript j denotes the right and left hand side of the running gear, respectively. Additionally, a roll angle φ and a vertical coordinate z have influence on the system dynamics. However, these variables can be inferred from $\boldsymbol{q}$ if nonlinear wheel and rail profiles are known and material elasticity is neglected.

The running gear is influenced by several external forces which are considered subsequently. Creep forces and a corresponding contact model are described in detail before remaining forces are stated.

Creep forces and moments occur in the contact points between wheels and rails. These are related to the current adhesion conditions $\mathcal{C}_{\mathrm{Tr}}$ which can be described in terms of the adhesion-slip characteristic in the corresponding contact points (see examples in Fig. 2). Different models can be used for representation of the adhesion-slip characteristic. A simple and intuitive model, which provides good approximations for the micro slip area, is linear Kalker theory [24]. It models longitudinal and lateral adhesion (f_x and f_y) linearly dependent on longitudinal, lateral and spin creepage (s_x, s_y and s_ψ) according to

$$\begin{bmatrix} F_x \\ F_y \end{bmatrix} = F_{\mathrm{N}} \begin{bmatrix} f_x \\ f_y \end{bmatrix} = -F_{\mathrm{N}} abG \begin{bmatrix} c_{11} & 0 & 0 \\ 0 & c_{22} & \sqrt{ab}c_{23} \end{bmatrix} \begin{bmatrix} s_x \\ s_y \\ s_\psi \end{bmatrix}, \tag{2}$$

with normal contact force F_{N}, lateral and longitudinal contact forces F_x and F_y, respectively. The Kalker coefficients are c_{11}, c_{22} and c_{23}, the shear modulus G, and the half axes of the contact ellipse are a and b. In (2), the creep torque about the vertical axis is neglected. It is worth mentioning, that the maximum adhesion and the maximum slip in lateral and longitudinal direction are coupled and limited with

$$s_{\max} \geq s = \sqrt{s_x^2 + s_y^2}, \tag{3}$$

$$f_{\max} \geq f = \sqrt{f_x^2 + f_y^2}, \tag{4}$$

where s is the total slip and f is the total tangential adhesion, respectively. Hence, all generalized coordinates are affected by adhesion and creep forces.

Besides creep forces, the motor torques τ_j are acting on the right and left wheel, respectively. Last, the rest of the train causes forces $\mathcal{F}_{\mathrm{Train}}$ on the running gear. These are mitigated by a secondary suspension stage. Another crucial impact for stability comes from dampers and springs which are placed between car body and wheel carrier.

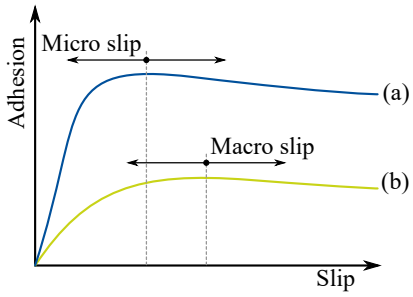

Fig. 2. Schematic adhesion-slip with good (a) and bad (b) adhesion conditions.

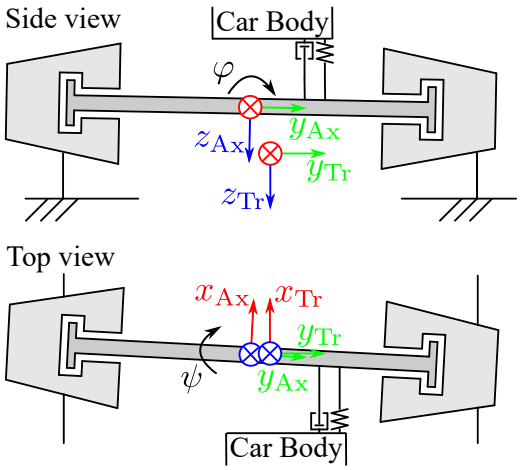

Fig. 3. Simplified model of a railway running gear with IRW for use in MPC.

B. Control-Oriented Model

For use in MPC, a simplified and discrete system representation $\boldsymbol{f}_{\mathrm{d}} : \mathbb{R}^n \times \mathbb{R}^m \to \mathbb{R}^n$ with

$$\boldsymbol{x}_{k+1} = \boldsymbol{f}_{\mathrm{d}}\left(\boldsymbol{x}_k, \boldsymbol{u}_k, \theta\right), \tag{5}$$

is derived by means of the LAGRANGE formalism. It features the state vector $\boldsymbol{x} \in \mathbb{R}^n$, the input vector $\boldsymbol{u} \in \mathbb{R}^m$, and a set which summarizes the varying parameters θ. A schematic can be seen in Fig. 3. It is worth mentioning, that the control model should only capture major dynamics over a short time horizon.

To account for the movement of the running gear along and inside the track, two additional variables y_{TrAx} and ψ_{TrAx} are introduced, which describe relative displacement and yaw angle between $(\mathrm{CF})_{\mathrm{Tr}}$ and $(\mathrm{CF})_{\mathrm{Ax}}$, respectively. Please note, the quantity ψ_{TrAx} needs to be distinguished from the absolute yaw angle between $(\mathrm{CF})_0$ and $(\mathrm{CF})_{\mathrm{Ax}}$. In this light, y_{TrAx} and ψ_{TrAx} are measures for the error from the desired path and should be minimized by the lateral guidance controller (see section III). Appropriate modeling choices for the dynamics of the auxiliary variables y_{TrAx} and ψ_{TrAx} are based on the track curvature and the current velocity [25], such that

$$\dot{\psi}_{\mathrm{TrAx}} = \dot{\psi} - \dot{\psi}_{\mathrm{Tr}}, \tag{6}$$

$$\dot{y}_{\mathrm{TrAx}} = \dot{x} \sin \psi_{\mathrm{TrAx}}. \tag{7}$$

Please note, by assuming (7), the lateral dynamics of the model are fully determined by $\dot{x}$ and ψ.

Regarding the dependent variables z and φ, conic wheels on a line-shaped rail are assumed based on [4, 26], which leads to the approximations

$$\varphi = -\Gamma y_{\mathrm{TrAx}} + \varphi_{\mathrm{Tr}}, \tag{8}$$

$$z = \frac{\delta_0 b}{2}\left(\frac{1}{\cos \psi_{\mathrm{TrAx}}} - 1\right) - \Gamma y_{\mathrm{TrAx}}^2, \tag{9}$$

where $\Gamma = \frac{\tan \delta_0}{b/2 - r_0 \tan \delta_0}$ is a geometrical parameter, b is the track gauge, r_0 is the nominal wheel radius and δ_0 is the

contact and cone angle, respectively, in the simplified model. The current wheel radii r_j and lateral distances between wheel carrier center and rails y_j can be inferred from the above relationships as well.

Despite extensive research, the reliable online estimation of adhesion parameters $\mathcal{C}_{\mathrm{Tr}}$ between wheels and rails remains difficult. Therefore, we assume that an accurately parameterized model of the adhesion-slip characteristic is not available. In this light, the creep forces cannot be modeled and no slip quantities between wheels and rails are needed. Hence, the model is further simplified by eliminating the wheel rotations from the generalized coordinate vector to reduce model complexity and computational effort in MPC. This is done by letting $c_{11} \to \infty$, which is equivalent to the assumption of ideal rolling, i. e.

$$\omega_{\mathrm{ri}} = -\frac{1}{r_{\mathrm{ri}}}\left(\dot{x} - y_{\mathrm{ri}}\left(\dot{\psi}_{\mathrm{Tr}} + \dot{\psi}\right)\right), \tag{10a}$$

$$\omega_{\mathrm{le}} = -\frac{1}{r_{\mathrm{le}}}\left(\dot{x} + y_{\mathrm{le}}\left(\dot{\psi}_{\mathrm{Tr}} + \dot{\psi}\right)\right). \tag{10b}$$

The constraints following from the above assumptions are considered directly in the generalized coordinates and generalized forces and not by means of LAGRANGE multipliers. Using the simplifications (7) through (10), a reduced vector of generalized coordinates $\boldsymbol{q}_{\mathrm{red}}^{\mathrm{T}} = [x, \psi]$ is obtained. The corresponding LAGRANGE formalism reads

$$\begin{aligned} E_{\mathrm{T}} = {} & \frac{1}{2}\left(m_x\dot{x}^2 + m\left(\dot{y}_{\mathrm{TrAx}}^2 + \dot{z}^2\right)\right) \\ & + \frac{1}{2}\left(J_{\mathrm{Ax}_z}\dot{\psi}^2 + J_{\mathrm{Ax}_x}\dot{\varphi}^2\right) \\ & + \frac{1}{2}\left(\boldsymbol{\omega}_{\mathrm{ri}}^{\mathrm{T}} + \boldsymbol{\omega}_{\mathrm{le}}^{\mathrm{T}}\right)\boldsymbol{J}_{\mathrm{W}}\left(\boldsymbol{\omega}_{\mathrm{ri}} + \boldsymbol{\omega}_{\mathrm{le}}\right), \end{aligned} \tag{11a}$$

$$E_{\mathrm{V}} = \frac{1}{2}\left(k_{\mathrm{s}_z}\left(\psi - \psi_{\mathrm{CB}}\right)^2 + k_{\mathrm{s}_x}\varphi^2\right) - mgz, \tag{11b}$$

$$E_{\mathrm{D}} = \frac{1}{2}\left(k_{\mathrm{d}_z}\left(\dot{\psi} - \dot{\psi}_{\mathrm{CB}}\right)^2 + k_{\mathrm{d}_x}\dot{\varphi}^2\right), \tag{11c}$$

$$\mathcal{L} = E_{\mathrm{T}} - E_{\mathrm{V}}, \tag{11d}$$

$$\frac{\mathrm{d}}{\mathrm{d}t}\left(\frac{\partial\mathcal{L}}{\partial\dot{\boldsymbol{q}}_{\mathrm{red}}}\right) - \frac{\partial\mathcal{L}}{\partial\boldsymbol{q}_{\mathrm{red}}} + \frac{\partial E_{\mathrm{D}}}{\partial\dot{\boldsymbol{q}}_{\mathrm{red}}} = \boldsymbol{F}_{\mathrm{gen}}, \tag{11e}$$

where E_{T} is the kinetic energy, E_{V} is the potential energy, E_{D} is the dissipation function and $\boldsymbol{F}_{\mathrm{gen}}$ denotes the generalized forces. The vectors $\boldsymbol{\omega}_j$ and the matrix $\boldsymbol{J}_{\mathrm{W}}$ describe the absolute rotation and the moment of inertia of the wheels in order to account for gyroscopic effects. The mass m is the joint mass of wheel carrier and the wheels. Similarly, J_{Ax_x} and J_{Ax_z} are the residual moments of inertia regarding a roll and an yaw motion in $(\mathrm{CF})_{\mathrm{Ax}}$. The mass $m_x = m + m_{\mathrm{CB}}/2$ accounts for the increased inertia in longitudinal direction since half the car body mass needs to be accelerated by one running gear. The moment of inertia of the wheels about their rotation axis is denoted J_{W_y}.

The parameters k_{s_x}, k_{s_z}, k_{d_x} and k_{d_z} are spring and damping constants, respectively. Please note, the yaw spring and damping moments do not occur due to relative yaw angles and rates between $(\mathrm{CF})_{\mathrm{Tr}}$ and $(\mathrm{CF})_{\mathrm{Ax}}$, but with respect to the car body. The corresponding variables of the car body ψ_{CB} and $\dot{\psi}_{\mathrm{CB}}$ can be approximated by the mean track yaw angle and rate between front and rear running gear, such that

$$\psi_{\mathrm{CB}} = \frac{\psi_{\mathrm{Tr}}(s) + \psi_{\mathrm{Tr}}(s - L_{\mathrm{CB}})}{2}, \tag{12}$$

$$\dot{\psi}_{\mathrm{CB}} = \frac{\dot{\psi}_{\mathrm{Tr}}(s) + \dot{\psi}_{\mathrm{Tr}}(s - L_{\mathrm{CB}})}{2}, \tag{13}$$

where L_{CB} denotes the distance between front and rear running gear.

Due to the assumption of ideal rolling, the motor torques τ_j act directly on the reduced generalized coordinates $\boldsymbol{q}_{\mathrm{red}}$. Therefore, the generalized forces $\boldsymbol{F}_{\mathrm{gen}}$ can be approximated by

$$\boldsymbol{F}_{\mathrm{gen}} = -\begin{bmatrix} \frac{\tau_{\mathrm{le}}}{r_{\mathrm{le}}} + \frac{\tau_{\mathrm{ri}}}{r_{\mathrm{ri}}} \\ \frac{y_{\mathrm{le}}\tau_{\mathrm{le}}}{r_{\mathrm{le}}} - \frac{y_{\mathrm{ri}}\tau_{\mathrm{ri}}}{r_{\mathrm{ri}}} \end{bmatrix} \tag{14}$$

for small angles ψ_{TrAx}.

By means of the LAGRANGE formalism, a continuous time state-space model with

$$\boldsymbol{x}^{\mathrm{T}} = \begin{bmatrix} x & \psi & \dot{x} & \dot{\psi} & y_{\mathrm{TrAx}} & \psi_{\mathrm{TrAx}} \end{bmatrix}, \tag{15}$$

$$\boldsymbol{u}^{\mathrm{T}} = \begin{bmatrix} \tau_{\mathrm{ri}} & \tau_{\mathrm{le}} \end{bmatrix}, \tag{16}$$

$$\theta = \left\{\psi_{\mathrm{Tr}} \quad \frac{\partial\psi_{\mathrm{Tr}}}{\partial s} \quad \varphi_{\mathrm{Tr}} \quad \frac{\partial\varphi_{\mathrm{Tr}}}{\partial s} \quad \epsilon_{\mathrm{Tr}} \quad \frac{\partial\epsilon_{\mathrm{Tr}}}{\partial s} \quad m_{\mathrm{CB}}\right\}. \tag{17}$$

is derived. Using a discretization method, e. g. the EULER algorithm, the desired discrete time representation of the nonlinear system dynamics $\boldsymbol{f}_{\mathrm{d}}$ is obtained.

III. CONTROLLER SYNTHESIS

The presented controller consists of three subsystems, the lateral controller, the longitudinal controller, and the integration system, see Fig. 4. As can be seen, the desired lateral position y^* and the demanded traction or braking force F_x^* of the running gear are set points for the control system. It is assumed that these values are provided by a high level system which controls all running gears in a holistic fashion in accordance with the project specification of NGT.

Another assumption is that geometric data about the track is available from a data base and that the current position of the train can be estimated sufficiently accurate. The latter is a

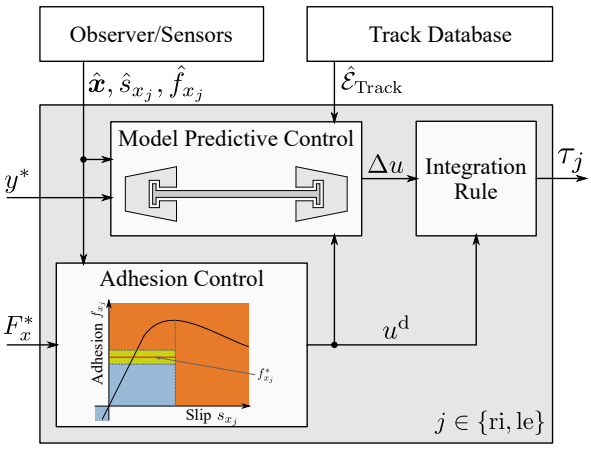

Fig. 4. Schematic of an MPC-based integrated control system for railway running gears.

current research topic at DLR and promising results have been obtained with a novel technique which uses local variations of the earth magnetic field to determine the accurate train location in a track network [27].

Further, the integrated control system is provided with measurements of states $\hat{\boldsymbol{x}}$, adhesion $\hat{f}_{x_j}$, and slip $\hat{s}_{x_j}$. The main objective of the current contribution is to investigate MPC approaches in the railway running gear context. Therefore, the MBS outputs are used as direct measurements for feedback control. However, powerful nonlinear EKF do exist for comparable applications and an observer-controller combination may be employed in future implementations [10, 28].

After some general remarks on the control framework and related assumptions, the three subsystems are explained in more detail in the following subsections. First, the adhesion controller in section III-A is concerned with the longitudinal dynamics and calculates a desired mean torque u^{d}. Second, a lateral guidance MPC-based controller which interacts with the adhesion controller is proposed. This subsystem determines a differential torque Δu between the left and the right wheel motor. Last, an integration system that combines u^{d} and Δu is introduced based on [21].

A. Adhesion Control

The adhesion controller should manage regular braking and acceleration scenarios as well as situations in which a maximum adhesion between wheel and rail is demanded. The latter occurs mostly during emergency braking or when adhesion conditions between wheels and rails are very low. For these cases, a new maximum-seeking adhesion controller has been proposed in [10] and will be briefly revisited. It is based on a sliding mode approach and approximates the switching function $\sigma = \partial f_x / \partial s_x$ by

$$\bar{\sigma} = \dot{\hat{f}}_x \dot{\hat{s}}_x, \tag{18}$$

based on appropriate derivations, estimates of longitudinal adhesion f_x, and slip s_x. The estimates can be obtained from nonlinear estimation algorithms designed in [29] which are assumed to be given here. For the current application, the control law can be adjusted to avoid a too dynamic motor torque, such that

$$u^{\mathrm{d}}_k = u^{\mathrm{d}}_{k-1} + \delta u \tag{19}$$

$$\delta u = p_1 \mathrm{sgn}\left(\bar{\sigma}\right), \tag{20}$$

where p_1 is a control parameter to be chosen sufficiently high. The resulting control behavior is illustrated in Fig. 5 on the right side, where the set point adhesion $f^*_{x_j}$ cannot be reached due to poor adhesion conditions (i. e. $f^*_{x_j} > f_{x_{\max}}$). Nonetheless, the maximum possible adhesion $f_{x_{\max}}$ should be exploited. The control law causes the motor torque to

- increase if the adhesion is below its maximum value (i. e. $\bar{\sigma} > 0$) and to
- decrease as soon as the unstable segment (III) is entered (i. e. $\bar{\sigma} < 0$).

Therefore, the controller keeps oscillating around $f_{x_{\max}}$ and eventually converges to a point close to it. The proof of convergence is based on LYAPUNOV arguments and a concavity assumption regarding the adhesion-slip characteristic in the considered region (i. e. $\partial^2 f_x / \partial s_x^2 < 0$).

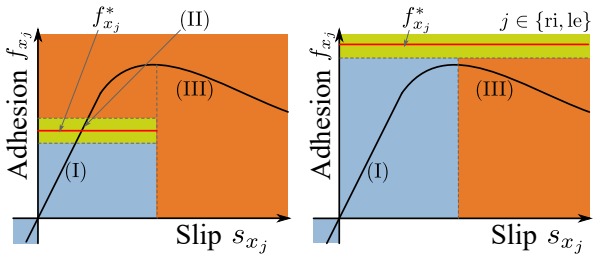

Fig. 5. Operational segments of adhesion control scheme for two scenarios: desired adhesion $f^*_{x_j} < f_{x_{\max}}$ (left) or $f^*_{x_j} > f_{x_{\max}}$ (right). Operation in segment (I): torque to be increased. Operation in segment (II): no torque change. Operation in segment (III): torque to be decreased.

In the current contribution, we will adopt this technique and generalize it for application in regular as well as maximum adhesion situations, both during traction and braking. To this end, a control law for regular operation is devised following the lines of [10] and combined with the above maximum control law (19).

Applying standard sliding mode theory to the regular braking case where the set point adhesion f^*_x lies below the maximum value of the adhesion-slip characteristic (see Fig. 5, left), we choose the switching function

$$\nu = f^*_x - f_x \approx f^*_x - \hat{f}_x = \bar{\nu}, \tag{21}$$

and the control update law

$$\delta u = p_2 \mathrm{sgn}\left(\bar{\nu}\right), \tag{22}$$

where p_2 is a control parameter. Considering the ideal switching function to proof convergence to f^*_x, a suitable LYAPUNOV candidate is

$$V(\boldsymbol{x}) = \frac{1}{2}\nu^2. \tag{23}$$

If we consider operation in the micro slip region for the regular braking and acceleration case, the use of linear Kalker theory as mentioned in section II is a valid assumption. Further, if we consider the situation when driving with constant speed, constant adhesion forces between wheel and rails are needed to counteract resistance forces such as friction. This implies $\omega r_j > \dot{x}$ which gives a constant negative slip value using the definition

$$s_x = \frac{\dot{x} - \omega r_j}{\dot{x}}, \tag{24}$$

$$\dot{s}_x = f(\boldsymbol{x}) + g(\boldsymbol{x})\delta u. \tag{25}$$

Starting from the above stationary driving condition, an increase in the motor torque δu leads to an increased rotational velocity of the wheel, which causes a further decrease of

the slip (i.e. $g(\boldsymbol{x}) < 0$). Hence, assuming a constant desired adhesion f_x^*, the time derivative of (23) reads

$$\begin{aligned}\dot{V}(\boldsymbol{x}) &= \nu\dot{\nu} && \text{(26a)}\\ &= -\nu\frac{\partial f_x}{\partial s_x}\dot{s}_x, && \text{(26b)}\\ &= \nu\left(abGc_{11}\right)\left(f(\boldsymbol{x}) + g(\boldsymbol{x})p_2\mathrm{sgn}\left(\nu\right)\right), && \text{(26c)}\\ &= \nu c f(\boldsymbol{x}) + \nu c g(\boldsymbol{x})p_2\mathrm{sgn}\left(\nu\right), && \text{(26d)}\\ &= \nu c f(\boldsymbol{x}) + |\nu|\, c g(\boldsymbol{x})p_2, && \text{(26e)}\end{aligned}$$

where c is a positive constant. From (26e) it is easy to see that a sufficiently high p_2 can ensure $\dot{V}(\boldsymbol{x}) < 0$, which renders the sliding manifold attractive. Under the standing assumptions, the control law (22) causes the adhesion to converge to set point f_x^*.

Taking the above findings further, our adhesion control method employs additional switching functions to account for traction and braking as well as for the case, when the system operates in the third quadrant of the adhesion-slip characteristic. Besides, a tolerance corridor around the demanded adhesion value f_x^* avoids oscillations. Hence, the adhesion-slip diagram is divided in multiple sub parts in which suitably chosen control design parameters L_i determine δu. Computationally efficient logical statements (such as $\hat{\dot{f}}_x\hat{\dot{s}}_x > 0$ or $f_x^* - \hat{f}_x > 0$) help to determine the sub segment, in which the system operates.

B. Nonlinear Model Predictive Control

MPC is a control method in which an optimization problem is solved to determine the "optimal" control input sequence with respect to a cost function. The first instance of the sequence is applied to the system and the optimization process is started again. The cost function is typically associated with the difference between the desired and the predicted future states over a prediction horizon H, when applying a certain control input sequence. For actual implementation, the prediction horizon is divided in L discrete time steps with duration $T = H/L$.

Applied to the current problem, the MPC-scheme takes the desired lateral position of the running gear in the track as a set point which corresponds to y_{TrAx} in the control-oriented model (see Fig. 4). Besides, the track geometry in accordance with (1) is taken as a measured disturbance input. Additionally, the observed states and the currently desired mean torque u^{d} are made available to the MPC. The latter is taken into account to improve prediction precision and hence control performance. It is worth mentioning, that not only momentary set points and track data can be used. In fact, whole sequences, e. g. dependent on the track coordinate, can be considered in the lateral controller.

The applied MPC-scheme is based on the control-oriented model introduced in section II-B. The model is used to predict future states $\bar{\boldsymbol{x}}_{[0,L]}(t)$ if a certain input sequence is applied. To retain a concise, yet brief description, a sequence $\{\boldsymbol{z}_k\}_{k=v}^{w}$ is denoted $\boldsymbol{z}_{[v,w]}$. Note further, predicted quantities are shown with a bar and a quantity followed by (t) is calculated at time t.

Following standard MPC notation and using (5), the NMPC optimization problem reads

$$\begin{aligned}\min_{\Delta\bar{u}_{[0,L-1]}(t)} \sum_{k=0}^{L-1} T\left\|\bar{\boldsymbol{x}}_k(t) - \boldsymbol{x}_k^{\mathrm{d}}(t)\right\|_{\boldsymbol{Q}}^2 + T\left\|\Delta\bar{u}_k(t)\right\|_R^2 \\ + J_{\mathrm{term}}, \end{aligned} \quad (27)$$

$$\begin{aligned}\text{s.t. } \bar{\boldsymbol{x}}_{k+1}(t) &= \boldsymbol{f}_{\mathrm{d}}\left(\bar{\boldsymbol{x}}_k(t), \bar{\boldsymbol{u}}_k(t), \theta\right), && \text{(28a)}\\ \bar{\boldsymbol{x}}_0(t) &= \hat{\boldsymbol{x}}_t, && \text{(28b)}\\ \bar{\boldsymbol{u}}_k(t) &= \begin{bmatrix} u_k^{\mathrm{d}}(t) + \Delta\bar{u}_k(t) \\ u_k^{\mathrm{d}}(t) - \Delta\bar{u}_k(t)\end{bmatrix}, && \text{(28c)}\\ \bar{\boldsymbol{u}}_{[0,L-1]}(t) &\in \boldsymbol{\mathcal{U}}, && \text{(28d)}\\ \bar{\boldsymbol{x}}_{[0,L]}(t) &\in \boldsymbol{\mathcal{X}}, \qquad \forall k \in [0, L-1], && \text{(28e)}\end{aligned}$$

where $\|\boldsymbol{v}\|_{\boldsymbol{M}}^2 = \boldsymbol{v}^{\mathrm{T}}\boldsymbol{M}\boldsymbol{v}$. $\boldsymbol{\mathcal{X}}$ and $\boldsymbol{\mathcal{U}}$ are the static state and input constraints, respectively. $\boldsymbol{Q}$ and R are cost weighting parameters of suitable dimensions. $\hat{\boldsymbol{x}}_t$ is the observed state vector at time t and J_{term} is an appropriate additive term to approximate the terminal cost. In the current implementation, a suitable choice which facilitates fast convergence to the desired set point y^* without static terminal constraints is

$$J_{\mathrm{term}} = T\left\|\bar{\boldsymbol{x}}_L(t) - \boldsymbol{x}_L^{\mathrm{d}}(t)\right\|_{\boldsymbol{Q}_L}^2, \quad (29)$$

where $\boldsymbol{Q}_L = \boldsymbol{Q}\cdot\mathrm{diag}\left(0,0,0,0,q,q\right)$ and q is a control design parameter.

The desired state sequence $\boldsymbol{x}_{[0,L]}^{\mathrm{d}}(t)$ is dependent on the current position and velocity along the track. For an efficient calculation, an approximation of the future track position and velocity is made over the prediction horizon. It is built from the desired lateral displacement sequence y^*, the track preview $\mathcal{E}_{\mathrm{Tr}}$, and the currently observed state vector $\hat{\boldsymbol{x}}_t$. In detail,

$$\boldsymbol{x}_k^{\mathrm{d}}(t)^{\mathrm{T}} = \begin{bmatrix} x_k^{\mathrm{d}} & \psi_k^{\mathrm{d}} & \dot{x}_k^{\mathrm{d}} & \dot{\psi}_k^{\mathrm{d}} & y_{\mathrm{TrAx}_k}^{\mathrm{d}} & \psi_{\mathrm{TrAx}_k}^{\mathrm{d}}\end{bmatrix}, \quad \text{(30a)}$$

$$\begin{aligned}\text{where } x_k^{\mathrm{d}} &= \hat{x}_t + \hat{\dot{x}}_t\, Tk + \frac{u^{\mathrm{d}}}{r_0 m_x}\frac{(Tk)^2}{2}, && \text{(30b)}\\ \psi_k^{\mathrm{d}} &= \psi_{\mathrm{TrAx}_k}^{\mathrm{d}} + \psi_{\mathrm{Tr}}(x_k^{\mathrm{d}}), && \text{(30c)}\\ \dot{x}_k^{\mathrm{d}} &= \hat{\dot{x}}_t + \frac{u^{\mathrm{d}}}{r_0 m_x}Tk, && \text{(30d)}\\ \dot{\psi}_k^{\mathrm{d}} &= \dot{\psi}_{\mathrm{TrAx}_k}^{\mathrm{d}} + \dot{\psi}_{\mathrm{Tr}}(x_k^{\mathrm{d}}, \dot{x}_k^{\mathrm{d}}), && \text{(30e)}\\ y_{\mathrm{TrAx}_k}^{\mathrm{d}} &= y^*(x_k^{\mathrm{d}}), && \text{(30f)}\\ \psi_{\mathrm{TrAx}_k}^{\mathrm{d}} &= \frac{\dot{y}_{\mathrm{TrAx}_k}^{\mathrm{d}}}{\dot{x}_k^{\mathrm{d}}}. && \text{(30g)}\end{aligned}$$

The same approximation is used for determination of the track preview in the system model.

C. Linear Time-Variant Model Predictive Control

The above MPC-scheme employs a detailed nonlinear system model. However, computation resources are often limited such that a model simplification is reasonable. To this end, the

system model (5) is linearized around the approximated future track position and velocity

$$\boldsymbol{A}_k = \left.\frac{\partial \boldsymbol{f}_\mathrm{d}}{\partial \boldsymbol{x}}\right|_{\boldsymbol{x}=\boldsymbol{x}_{\mathrm{lin}_k},\boldsymbol{u}=u^\mathrm{d},\theta=\theta_{\mathrm{lin}_k}}, \tag{31}$$

$$\boldsymbol{B}_k = \left.\frac{\partial \boldsymbol{f}_\mathrm{d}}{\partial \boldsymbol{u}}\right|_{\boldsymbol{x}=\boldsymbol{x}_{\mathrm{lin}_k},\boldsymbol{u}=u^\mathrm{d},\theta=\theta_{\mathrm{lin}_k}}, \tag{32}$$

$$\text{where } \boldsymbol{x}_{\mathrm{lin}_k} = \begin{bmatrix} x_k^\mathrm{d} & 0 & \dot{x}_k^\mathrm{d} & 0 & 0 & 0 \end{bmatrix}, \tag{33}$$

$$\theta_{\mathrm{lin}_k} = \theta(x_k^\mathrm{d}, \dot{x}_k^\mathrm{d}), \tag{34}$$

and $\theta(x_k^\mathrm{d}, \dot{x}_k^\mathrm{d})$ denotes the set of variable parameters, dependent on the position and velocity forecasts. The dynamic constraint (28a) is reformulated using the Linear Time-Variant (LTV) system model

$$\boldsymbol{x}_{k+1} = \boldsymbol{A}_k \boldsymbol{x}_k + \boldsymbol{B}_k \boldsymbol{u}_k, \tag{35}$$

to obtain an LTV-MPC problem. The remaining parts of the controller are unchanged.

D. Integration Approach

For the adhesion controller, it is crucial to react quickly if adhesion conditions worsen abruptly. Therefore, the adhesion control operates at a high frequency, e. g. , $1000\mathrm{Hz}$. The lateral controller, however, solves an optimization problem repetitively. In this light, computational resources do limit the maximum frequency at which the MPC-scheme can calculate control outputs. The integration rule considers this frequency mismatch and ensures the commanded differential torque Δu, which is determined by the MPC, even if u^d changes sharply. Following the approach in [21], no fixed torque values are allocated to the longitudinal and lateral controller. Rather, the output torques are determined by the integration rule

$$\tau_{\mathrm{long}_k} = \begin{cases} \min\left(u_k^\mathrm{d}, \tau_\mathrm{max} - |\Delta u_k|\right), & \text{if } u_k^\mathrm{d} > 0, \\ \max\left(u_k^\mathrm{d}, \tau_\mathrm{min} + |\Delta u_k|\right), & \text{otherwise,} \end{cases} \tag{36}$$

$$\boldsymbol{u}_k = \begin{bmatrix} \tau_{\mathrm{long}_k} + \Delta u_k \\ \tau_{\mathrm{long}_k} - \Delta u_k \end{bmatrix} \tag{37}$$

where τ_max and τ_min are the maximum and minimum possible wheel motor torques, respectively.
In the end, it is possible to smoothly adapt the control objective from longitudinal emphasis to lateral emphasis by tuning the matrices $\boldsymbol{Q}$ and R in the MPC schemes.

IV. Experimental Results

To show the effectiveness of the proposed integrated controller, extensive simulations are conducted. Since the corresponding plant models are known, the parameters of the MPC-model are assumed to be known as well and no parameter identification is performed. The control design parameters $\boldsymbol{Q}$, R, q, the prediction horizon length H, and time step T are tuned using a global optimization algorithm. In detail, a Particle Swarm Optimization (PSO) minimizes a cost function along the design parameters [30]. The cost function is associated with the difference $y_\mathrm{TrAx} - y^*$ and the magnitude of the differential torque Δu. Multiple velocities together with tracks $\mathcal{T}_1$ to $\mathcal{T}_4$ are taken into account. The control design parameters p_i are tuned heuristically.
For comparison with the obtained results, the control scheme from [6, 22] is applied. It follows a feedback linearization approach and features a simplified nonlinear inverse system model of the running gear. Therefore, the technique is also known as Nonlinear Dynamic Inversion (NDI) [31].
First, the used evaluation framework is illustrated in detail. Second, the test scenarios are presented in context of the performance criteria. Last, the actual results are shown and explained in comparison with existing methods.

A. Simulation Environment

The simulations are performed with a detailed model of a single high-speed train car and using the MBS software SIMPACK . The controller implementation is based on MATLAB and SIMULINK . In the experiments, SIMULINK and SIMPACK communicate via TCP/IP protocol at $1\mathrm{kHz}$ in a co-simulation environment.
The NMPC-scheme is implemented with the nonlinear optimization toolbox CASADI [32] which provides an comprehensive framework for convenient set-up of NMPC problems. For solving of nonlinear optimization problems, the package IPOPT is used which implements an interior point method for nonlinear programming [33].
For rough comparison of computational effort, computation times are given. The calculations are performed with an INTEL© CORE™ i7-6700K CPU @ 4.00GHz, 16 GB RAM.

B. Test Scenarios and Performance Criteria

The control performance will be evaluated by means of the Root Mean Squared Error (RMSE) of the desired lateral displacement y^* and the RMSE of the desired adhesion f_x^* in the regular operation case. If high longitudinal forces F_x^* are demanded, i. e. , if either actuator saturation occurs or the maximum possible adhesion in the wheel rail contacts is exceeded, the braking distance is taken as a measure.
Since the application of MPC in running gear control is rather new, our work focuses mainly on methodological aspects rather than a ready-to-use implementation. Therefore, control-oriented evaluation scenarios are used to scrutinize and compare different concepts. The MBS results are based on a curve entering situation. The vehicle starts on a straight track, passes a clothoid and enters a curve with constant radius. To show the effectiveness of the proposed schemes, the evaluation tracks $\mathcal{T}_i$ are designed for different velocities from 40 to $400\mathrm{km/h}$ and featuring different unbalanced lateral accelerations between 0 and the operationally allowed maximum of $0.65\mathrm{m/s^2}$. The curve radii are chosen comparable to previous publications [7, 34] and the superelevation is hence a dependent quantity[1]. An overview of the scenarios can be found in Tab. I. In addition, the curve radius of track $\mathcal{T}_1$ is chosen such that the geometrically required yaw angle between wheel carrier and car body in perfect curving is at 80% of the mechanical yaw end stops.

[1]The superelevation l_sup is deduced from the fixed values for curve radius R, velocity v and design unbalanced lateral acceleration a by $l_\mathrm{sup} = b \tan\varphi_\mathrm{sup}$ and $\varphi_\mathrm{sup} = \arcsin\frac{v^2/R - a}{g}$

TABLE I
EVALUATION TRACKS $\mathcal{T}_i$ FOR SIMPACK MULTI-BODY CO-SIMULATION, ENTERING OF IDEAL CURVES

Index i	Design velocity [km/h]	Design lat. acceleration [m/s^2]	Curve radius [m]	Super-elevation [m]
1	40	0.0000	175	0.108
2	160	0.2167	1500	0.168
3	280	0.4333	4250	0.151
4	400	0.6500	8500	0.123

In this context, $\mathcal{T}_1$ is designed to test control performance in a very narrow curve. In the current contribution, the evaluation curves are geometrically ideal without any irregularities.

C. Evaluation

First, the capability of mechatronic guidance is illustrated for the developed MPC scheme. After, the behavior of the adhesion controller is presented. Last, the performance of the integrated controller is shown for different sets of control parameters.

Fig. 6 depicts the control behavior when riding on a curved track without traction or braking (i. e. $F_x^* = 0$). A variable set point of the lateral position y^* is imposed in the form of a sine sweep. The devised MPC schemes are shown in contrast to the previously developed NDI controller. Looking at the beginning of the clothoid at 25m it can be seen, that all controllers can cope well with the change in superelevation, as they immediately counteract the gyroscopic effects by an adequate motor torque. The middle plot shows the absolute yaw angle and hence illustrates the overall path tracking ability. In addition to path following, it is possible to chase a desired lateral position within the track. The MPC-based controllers show a better accuracy than the NDI controller. In fact, the MPC approaches follow the set point nearly without delay. A reason for this behavior is the available preview information about the future set points. In this context, the error needs to occur for the NDI scheme to react. In contrast, MPC can avoid the error beforehand. This becomes visible in the motor torque plots as well, where the curve shapes are comparable but have slight offset. In spite of the generally better performance, MPC shows a drift in the lateral position and values above 2.5mm are not matched well. A possible explanation is the heuristic choice of control design parameters or the strongly simplified prediction model. When comparing both MPC schemes, NMPC is marginally superior to LTV-MPC in this scenario. However, the increased accuracy comes at the cost of a higher computational burden. The mean time to solve an optimization problem took 5.6ms in LTV-MPC and 20.3ms in NMPC.

Similar co-simulations have been conducted for different velocities. To obtain comparable results, the same straight test track and the same sinusoidal set points for y^* are used. As can be seen in Fig. 7, the experimental results resemble the previous observations regarding the lateral position. The most

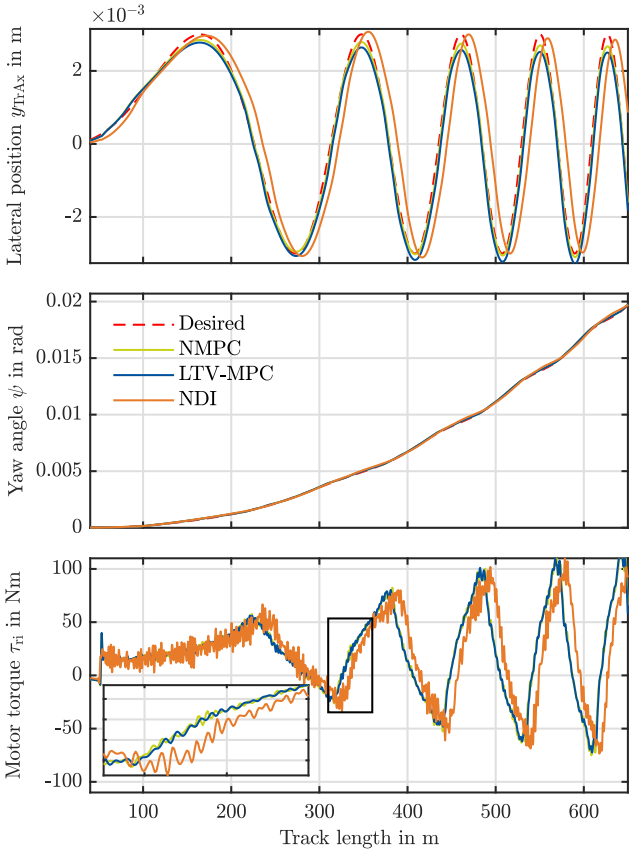

Fig. 6. Co-simulation result, evaluation track $\mathcal{T}_3$, 280km/h, good adhesion conditions, $F_x^* = 0$.

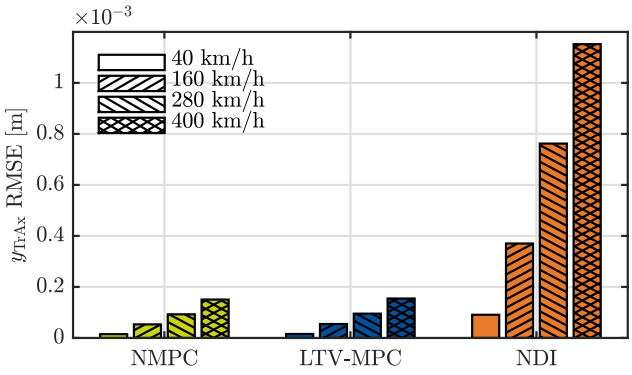

Fig. 7. Co-simulation result, 1000m of straight track, good adhesion conditions, $F_x^* = 0$, sine with period 150m as y^* set point.

accurate lateral motion is achieved with NMPC, followed by LTV-MPC and NDI. Within each method, better results are obtained with lower velocities. The velocity dependence of the absolute lateral position error is highest with the NDI method and is mitigated by the MPC-based controllers.

For evaluation of the longitudinal control law, a straight track with poor adhesion conditions is considered in Fig. 8. First, a relatively low traction force F_x^* set point is provided, such that $f_x^* < f_{x_{\max}}$. In this regular operation case, the motor torque converges to f_x^* as proved in section III-A. From 130m, the set point adhesion exceeds the maximum possible

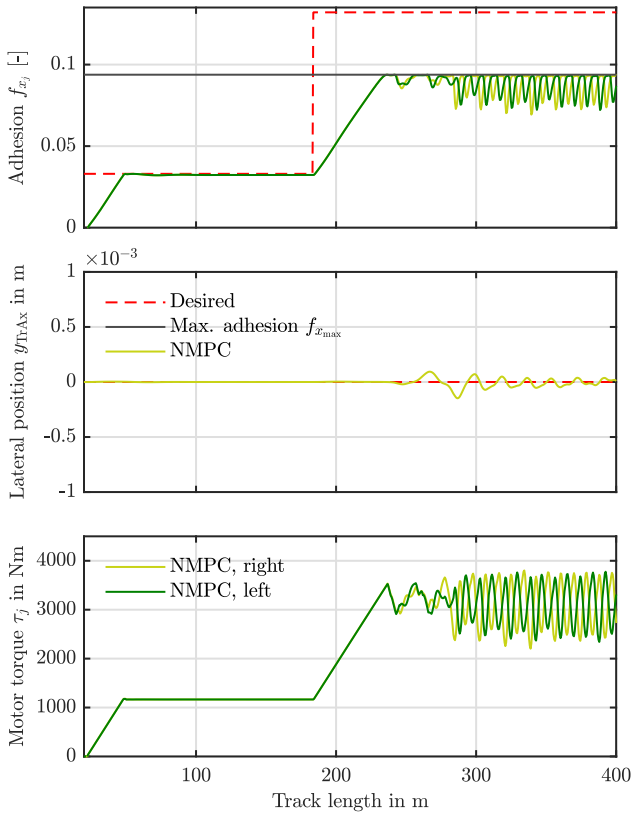

Fig. 8. Co-simulation result, straight track, 400km/h, critical adhesion conditions.

adhesion $f_{x_{\max}}$. In this situation, the controller should steer the adhesion to the maximum possible value while avoiding excessive slip and the corresponding unstable behavior. It becomes visual in the top plot, that the maximum adhesion is approached. As soon as one wheel-rail contact enters the macro slip regime, the control input u^{d} is decreased rapidly to drive the system back to the stable micro slip region. From there, the maximum adhesion is approached again. This behavior is depicted from 240m in the top plot of Fig. 8. It is worth mentioning that the devised adhesion controller operates robustly without knowledge of the adhesion slip characteristic and relies only on basic assumptions. Regarding the lateral direction, the control task becomes more difficult due to the poor adhesion conditions. Nonetheless, the results in the middle plot demonstrate that NMPC ensures a stable oscillation around the set point.

After the separate view on lateral and longitudinal behavior, the integrated concept is discussed. The link between demanded control inputs of MPC-based guidance controller and adhesion controller is realized by the integration rule presented in III-D. The resulting torque is limited by actuator constraints. Thus, the situation of actuator saturation implies a trade-off between lateral and longitudinal control performance. Considering the presented integrated controller, the control objective can be varied smoothly between lateral and longitudinal emphasis by adjusting the MPC parameters $\boldsymbol{Q}$ and R. This is shown in Fig. 9 by means of co-simulation results when

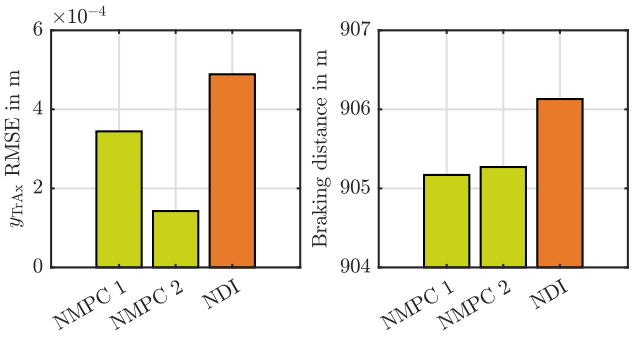

Fig. 9. Co-simulation result for NMPC-based and NDI-based integrated controllers with multiple parameter sets, 1000m of evaluation track $\mathcal{T}_2$, 160km/h, good adhesion conditions, high braking demand and actuator saturation, sine sweep as y^* set point.

driving on track $\mathcal{T}_2$ with 160km/h. The actuators are operating in saturation since adhesion conditions are good and a high braking demand value is set (i. e. $f_x^* \ll 0$). Multiple parameter sets for the NMPC-based integrated controller are employed. As can be seen, a trade-off between lateral accuracy and braking distance is possible by means of adjusted controller parameters. In this example, the only parameter changed is the input cost parameter R. In addition, we see that both NMPC-based controllers outperform the NDI scheme in terms of lateral position accuracy and braking distance.

V. Conclusion and Outlook

In the current work, we explored the use of MPC for control of high-speed railway running gears with IRW. A novel adhesion-based control method for joint handling of regular and critical adhesion conditions is presented. Both techniques are combined using an integration rule. Thus, a holistic control scheme for handling of multiple regular and critical operation scenarios is contributed. Co-simulation results with a detailed MBS software show the effectiveness of the devised integrated controller, underlining that the application of MPC is a promising approach for control of railway running gears with IRW. In particular, the presented control scheme outperforms a state-of-the-art NDI controller.

However, certain aspects require special attention. The functionality of the adhesion-based controller is dependent on a set of basic assumptions. These assumptions may not be fulfilled in every single situation which needs to be investigated in the future. Furthermore, both lateral and longitudinal sub control systems come with a number of control design parameters which need to be determined. The parameters can partly influence each other, so that tuning for multiple realistic cases may be difficult.

In accordance with the main objective to explore the application of MPC in railway running gears, the presented evaluation was strongly control-oriented. Nonetheless, a controller-observer implementation as well as further evaluation scenarios with a focus on track irregularities should be emphasized in future developments.

A common drawback of MPC is the computational burden. A LTV-MPC controller has been devised to mitigate the issue.

An approximate optimization time reduction to a fourth of the initial value has been achieved but additional work is required to ensure safe real-time operation. An interesting option for future research is the design of a centralized MPC controller for joint handling of lateral and longitudinal control.

ACKNOWLEDGMENTS

Jan-Hendrik Ewering would like to thank the research group leaders Zygimantas Ziaukas and Andreas Heckmann who enabled the joint project between the Institute of Mechatronic Systems and the Institute of System Dynamics and Control.

REFERENCES

[1] B. Abdelfattah, "Entwicklung eines Losradfahrwerkskonzeptes für Schienenfahrzeuge," Ph.D. dissertation, RWTH Aachen University, 2014.

[2] T. X. Mei and R. M. Goodall, "Robust control for independently rotating wheelsets on a railway vehicle using practical sensors," *IEEE Transactions on Control Systems Technology*, vol. 9, no. 4, pp. 599–607, 2001.

[3] ——, "Practical strategies for controlling railway wheelsets independently rotating wheels," *Journal of Dynamic Systems, Measurement, and Control*, vol. 125, no. 3, pp. 354–360, 2003.

[4] A. Heckmann, C. Schwarz, T. Bünte, A. Keck, and J. Brembeck, "Control development for the scaled experimental railway running gear of DLR," in *Proc. 24th IAVSD International Symposium on Dynamics of Vehicles on Roads and Tracks*, 2015.

[5] A. Heckmann, D. Lüdicke, G. Grether, and A. Keck, "From scaled experiments of mechatronic guidance to multibody simulations of DLR's Next Generation Train set," in *Proc. 25th IAVSD International Symposium on Dynamics of Vehicles on Roads and Tracks*, 2017.

[6] G. Grether, G. Looye, and A. Heckmann, "Lateral guidance of independently rotating wheel pairs using feedback linearization," in *Proc. Fourth International Conference on Railway Technology: Research, Development and Maintenance*, 2018.

[7] G. Grether, A. Heckmann, and G. Looye, "Lateral guidance control using information of preceding wheel pairs," in *Proc. 26th IAVSD International Symposium on Dynamics of Vehicles on Roads and Tracks*, 2019, pp. 863–871.

[8] N.-J. Lee and C.-G. Kang, "Wheel slide protection control using a command map and smith predictor for the pneumatic brake system of a railway vehicle," *Vehicle System Dynamics*, vol. 54, no. 10, pp. 1491–1510, 2016.

[9] T. Stützle, T. Engelhardt, M. Enning, and D. Abel, "Wheelslide and wheelskid protection for a single-wheel drive and brake module (sdbm) for rail vehicles," *IFAC Proceedings Volumes*, vol. 41, no. 2, pp. 16 051–16 056, 2008.

[10] C. Schwarz, T. Posielek, and B. Goetjes, "Adhesion-based maximum-seeking brake control for railway vehicles," in *Proc. 27th IAVSD International Symposium on Dynamics of Vehicles on Roads and Tracks*, 2021.

[11] ——, "Beobachterbasierte Kraftschlussregelung von Scheibenbremssystemen," in *Proc. 3rd International Railway Symposium Aachen (IRSA)*, 2021, pp. 120–135.

[12] C. Schwarz and A. Keck, "Simultaneous estimation of wheel-rail adhesion and brake friction behaviour," *IFAC-PapersOnLine*, vol. 53, no. 2, pp. 8470–8475, 2020.

[13] P. Falcone, H. E. Tseng, J. Asgari, F. Borrelli, and D. Hrovat, "Integrated braking and steering model predictive control approach in autonomous vehicles," *IFAC Proceedings Volumes*, vol. 40, no. 10, pp. 273–278, 2007.

[14] M. Ataei, A. Khajepour, and S. Jeon, "Model predictive control for integrated lateral stability, traction/braking control, and rollover prevention of electric vehicles," *Vehicle System Dynamics*, vol. 58, no. 1, pp. 49–73, 2020.

[15] H. Zhao, B. Ren, H. Chen, and W. Deng, "Model predictive control allocation for stability improvement of four–wheel drive electric vehicles in critical driving condition," *IET Control Theory & Applications*, vol. 9, no. 18, pp. 2688–2696, 2015.

[16] M. Gretzschel and L. Bose, "A new concept for integrated guidance and drive of railway running gears," *Control Engineering Practice*, vol. 10, no. 9, pp. 1013–1021, 2002.

[17] J. Pérez, J. M. Busturia, T. X. Mei, and J. Vinolas, "Combined active steering and traction for mechatronic bogie vehicles with independently rotating wheels," *Annual Reviews in Control*, vol. 28, no. 2, pp. 207–217, 2004.

[18] T. Gordon, M. Howell, and F. Brandao, "Integrated control methodologies for road vehicles," *Vehicle System Dynamics*, vol. 40, no. 1-3, pp. 157–190, 2003.

[19] J. Feng, J. Li, and R. M. Goodall, "Integrated control strategies for railway vehicles with independently-driven wheel motors," *Frontiers of Mechanical Engineering in China*, vol. 3, no. 3, pp. 239–250, 2008.

[20] Z.-G. Lu, X.-J. Sun, and J.-Q. Yang, "Integrated active control of independently rotating wheels on rail vehicles via observers," *Proceedings of the Institution of Mechanical Engineers, Part F: Journal of Rail and Rapid Transit*, vol. 231, no. 3, pp. 295–305, 2017.

[21] C. Schwarz and B. Goetjes, "Integrated vehicle dynamics control for a mechatronic railway running gear," in *Proc. Fifth International Conference on Railway Technology: Research, Development and Maintenance*, 2022.

[22] A. Heckmann, A. Keck, and G. Grether, "Active guidance of a railway running gear with independently rotating wheels," in *Proc. IEEE Vehicle Power and Propulsion Conference (VPPC)*, 2020, pp. 1–5.

[23] R. Goodall and H. Li, "Solid axle and independently-rotating railway wheelsets - a control engineering assessment of stability," *Vehicle System Dynamics*, vol. 33, no. 1, pp. 57–67, 2000.

[24] J. J. Kalker, "A fast algorithm for the simplified theory of rolling contact," *Vehicle System Dynamics*, vol. 11, no. 1, pp. 1–13, 1982.

[25] M. Morari, M. Thoma, L. Del Re, F. Allgöwer, L. Glielmo, C. Guardiola, and I. Kolmanovsky, *Automotive Model Predictive Control*. London: Springer, 2010, vol. 402.

[26] A. Jaschinski, "On the application of similarity laws to a scaled railway bogie model," Ph.D. dissertation, Technical University Delft, 1990.

[27] B. Siebler, O. Heirich, S. Sand, and U. D. Hanebeck, "Joint train localization and track identification based on earth magnetic field distortions," in *Proc. IEEE/ION Position, Location and Navigation Symposium (PLANS)*, 2020, pp. 941–948.

[28] A. Keck, C. Schwarz, T. Meurer, A. Heckmann, and G. Grether, "Estimating the wheel lateral position of a mechatronic railway running gear with nonlinear wheel–rail geometry," *Mechatronics*, vol. 73, p. 102457, 2021.

[29] C. Schwarz and A. Keck, "Observer synthesis for the adhesion estimation of a railway running gear," *IFAC-PapersOnLine*, vol. 52, no. 15, pp. 319–324, 2019.

[30] J. Kennedy and R. Eberhart, "Particle swarm optimization," in *Proc. IEEE International Conference on Neural Networks (ICNN)*, 1995, pp. 1942–1948.

[31] G. Ducard and H. P. Geering, "Stability analysis of a dynamic inversion based pitch rate controller for an unmanned aircraft," in *Proc. IEEE/RSJ International Conference on Intelligent Robots and Systems*, 2008, pp. 360–366.

[32] J. A. E. Andersson, J. Gillis, G. Horn, J. B. Rawlings, and M. Diehl, "Casadi – a software framework for nonlinear optimization and optimal control," *Mathematical Programming Computation*, In Press, 2018.

[33] A. Wächter and L. T. Biegler, "On the implementation of an interior-point filter line-search algorithm for large-scale nonlinear programming," *Mathematical Programming*, vol. 106, no. 1, pp. 25–57, 2006.

[34] B. Kurzeck, A. Heckmann, C. Wesseler, and M. Rapp, "Mechatronic track guidance on disturbed track: the trade-off between actuator performance and wheel wear," *Vehicle System Dynamics*, vol. 52, no. sup1, pp. 109–124, 2014.

Jan-Hendrik Ewering received his B.Eng. degree in mechanical engineering from University of Applied Sciences Münster, Steinfurt, Germany, in 2020. Currently he is studying towards his M.Sc. degree in mechanical engineering at Leibniz Universität Hannover, Hanover, Germany, and took courses at University of Cambridge, Cambridge, UK. He is with the Institute of Mechatronic Systems and the Institute of System Dynamics and Control of the German Aerospace Center (DLR) as a working student and for his Master's Thesis.

Christoph Schwarz received his B.Sc. and M.Sc. degrees in mechanical engineering from TU München, Munich, Germany, in 2011 and 2013, respectively. In 2022 he received his Ph.D. from RWTH Aachen University, Aachen, Germany. Currently he is working at the Institute of System Dynamics and Control of the German Aerospace Center (DLR) in Oberpfaffenhofen, Germany. His research interests include model-based estimator and control concepts especially in the field of friction and adhesion phenomena in railway context.

Simon F. G. Ehlers received his B.Sc. and M.Sc. degrees in mechanical engineering from Leibniz Universität Hannover, Hanover, Germany, in 2016 and 2019, respectively. Currently he is working towards his Ph.D. degree at the Institute of Mechatronic Systems at Leibniz Universität Hannover. His research interests include model- and learning-based estimator concepts especially in the field of vehicle dynamics.

Hans-Georg Jacob studied in Hanover and Brunswick and received his diploma degree in mechanical engineering in 1990. He received his Ph.D. and his habilitation from Universität Hannover, Hanover, Germany, in 1995 and 2006, respectively. Currently he is working as deputy director of the Institute of Mechatronic Systems at Leibniz Universität Hannover after being professor for mechatronics and robotics at University of Applied Sciences Hanover for eight years.

4 Further Description of Methods

A detailed explanation of the applied methods is given in this chapter. It provides background and extensions which could not be mentioned in the scientific publication due to the limited space. Apart from the development and implementation of a new controller architecture for railway running gears with IRW, additional approaches for modeling and system analysis are investigated. The obtained results may be used for future extensions and enhancements.
A more sophisticated modeling approach than discussed in chapter 3 is presented in 4.1. It is followed by section 4.2, in which additional insights in control synthesis are given. Lastly, the simulation environment and the link between different programs is visualized in section 4.3, accompanied by further experimental results.

4.1 Modeling

In this section, the track modeling described in the publication is enhanced by the consideration of track irregularities. Apart from that, the running gear system with IRW is carefully modeled by means of the LAGRANGE formalism while using homogeneous transformations. Furthermore, strategies are devised to tackle nonlinear influences resulting from wheel and rail profiles.

4.1.1 Track

In real world systems, the ideal track path is disturbed by track irregularities. Bounds for these errors are expressed in the frequency domain of the track length coordinate rather than in absolute terms. Therefore, lateral position error, vertical position error, superelevation (cross-level height) error and gauge widening error are described in terms of Power Spectral Densities (PSD). An overview together with usual design values for the PSD can be found in [HPK18].
Due to the structure of the simulation environment, the encountered track irregularities need to be provided to both, the controller and the simulative plant. In the MBS software SIMPACK, the PSD can be used directly to create randomly sampled error signals, which obey the required frequency domain characteristics. The sampled signal can be exported and incorporated in other programs. However, the process of manual exporting and importing is laborious and prevents flexible handling of different PSD and custom irregularity shapes.

To have full control over the simulated track irregularities, the artificial errors are sampled using MATLAB and provided to both, the controller and SIMPACK . The desired and estimated PSD of randomly sampled errors are shown in Fig. 4.1.

4.1.2 Running Gear with Driven Independently Rotating Wheels

In the scientific publication, a simplified control model for use in MPC is derived. Ideal rolling is assumed and the lateral dynamics are reduced to a first order equation dependent on the difference angle between wheel carrier and track ψ_{TrAx}. Furthermore, the wheel and rail geometries are approximated by a conic wheel on a line rail.
However, to gain insight in the system dynamics and to facilitate the development of more accurate control models, it is meaningful to carry out a detailed system analysis. An own derivation makes sense in spite of existing models, since individually set generalized coordinates can be used. Besides, individual assumptions can be employed.

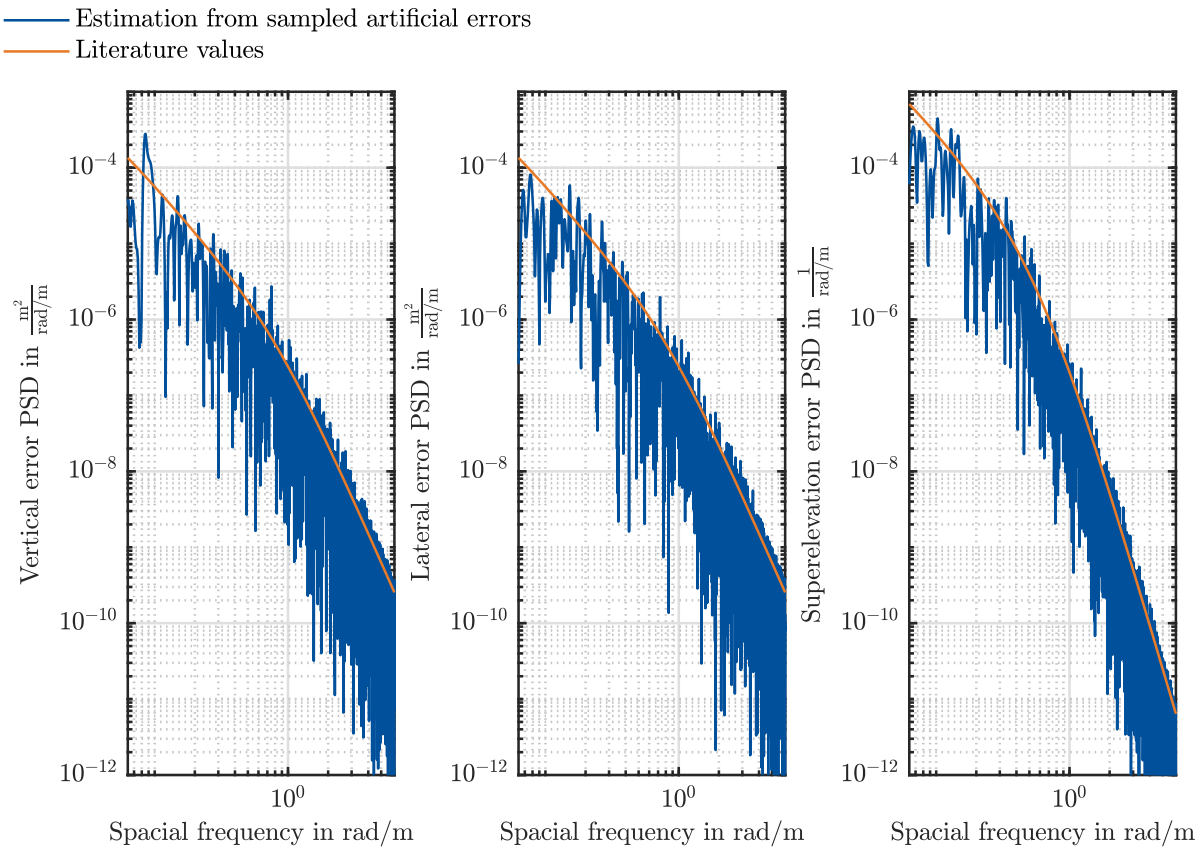

Figure 4.1: Desired design PSD according to [HPK18] and estimated PSD of randomly sampled track irregularity sequences.

The subsequent derivation of equations of motion is based on LAGRANGES' equation of the second kind for holonomic systems. In fact, the current running gear plant is a nonholonomic system. These systems are usually treated by means of LAGRANGE multipliers to account for forces which occur due to nonholonomic constraints [HN97]. In the subsequent analysis, however, these forces are directly considered as generalized forces. In detail, lateral and longitudinal creep forces occur in the rail-wheel contacts and are modeled using linear Kalker theory. The system description is performed by means of multiple CF and an overview is presented in Fig. 4.2, where ${}^{i}\boldsymbol{T}_{j}$ denotes the homogeneous transformation from $(\mathrm{CF})_j$ to $(\mathrm{CF})_i$. Additional information regarding the transformations are given in the following paragraphs. The running gear is regarded as a multi-body system with three rigid bodies, the wheel carrier (subscript $\square_{\mathrm{Ax}}$), right wheel (subscript $\square_{\mathrm{Wri}}$) and left wheel (subscript $\square_{\mathrm{Wle}}$). The corresponding centers of gravity are denoted by $\square_S$. Further, the wheel-rail contacts left and right are referred to with $\square_{\mathrm{Cri}}$ and $\square_{\mathrm{Cle}}$, respectively. An auxiliary coordinate frame at the track center line carries the subscript $\square_{\mathrm{Tr}}$.

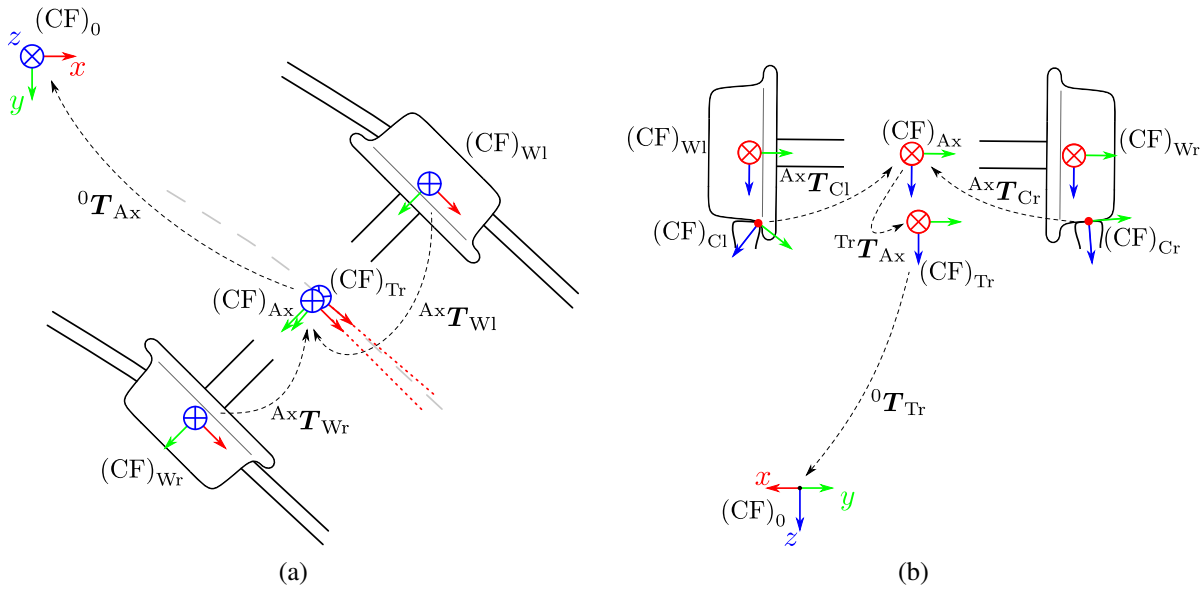

Figure 4.2: Top view (a) and rear view (b) sketch of a railway running gear with IRW, including coordinate systems and transformations. Rear view is shown for relative yaw angle between track frame and wheel carrier frame $\psi - \psi_{\mathrm{Tr}} = 0$.

Transformation matrices

To build the relationships between the CF systematically, homogeneous transformations are applied. The rotation matrices are built using EULER convention

$$\boldsymbol{R}(\alpha,\beta,\gamma) \coloneqq \boldsymbol{R}_{\mathrm{EUL}}(\alpha,\beta,\gamma) = \boldsymbol{R}_z(\alpha)\boldsymbol{R}_x(\beta)\boldsymbol{R}_z(\gamma), \tag{4.17}$$

where $\boldsymbol{R}_x$ and $\boldsymbol{R}_z$ denote elementary rotation matrices about the current x and y axis, respectively. For a detailed explanation regarding homogeneous transformations and rotation matrices, the reader is referred to [HAOR15]. The transformations used are defined as

$${}^{0}\boldsymbol{T}_{\mathrm{Tr}} = \left[\begin{array}{c|c} \boldsymbol{R}\left(0,\varphi_{\mathrm{Tr}},\psi_{\mathrm{Tr}}\right) & {}_{(0)}\boldsymbol{r}_{\mathrm{Tr}} \\ \hline \boldsymbol{0} & 1 \end{array}\right], \quad \text{with } {}_{(0)}\boldsymbol{r}_{\mathrm{Tr}}^{\mathrm{T}} = \begin{bmatrix} x_{\mathrm{Tr}} & y_{\mathrm{Tr}} & 0 \end{bmatrix}, \tag{4.18}$$

$${}^{0}\boldsymbol{T}_{\mathrm{Ax}} = \left[\begin{array}{c|c} \boldsymbol{R}\left(0,\varphi,\psi\right) & {}_{(0)}\boldsymbol{r}_{\mathrm{Ax}} \\ \hline \boldsymbol{0} & 1 \end{array}\right], \quad \text{with } {}_{(0)}\boldsymbol{r}_{\mathrm{Ax}}^{\mathrm{T}} = \begin{bmatrix} x & y & z \end{bmatrix}, \tag{4.19}$$

$${}^{\mathrm{Ax}}\boldsymbol{T}_{\mathrm{Wri}} = \left[\begin{array}{c|c} \boldsymbol{R}\left(-\pi/2,\varphi_{\mathrm{Wri}},\pi/2\right) & {}_{(\mathrm{Ax})}\boldsymbol{r}_{\mathrm{Wri}} \\ \hline \boldsymbol{0} & 1 \end{array}\right], \quad \text{with } {}_{(\mathrm{Ax})}\boldsymbol{r}_{\mathrm{Wri}}^{\mathrm{T}} = \begin{bmatrix} 0 & y_{\mathrm{W_S}} & 0 \end{bmatrix}, \tag{4.20}$$

$${}^{\mathrm{Ax}}\boldsymbol{T}_{\mathrm{Wle}} = \left[\begin{array}{c|c} \boldsymbol{R}\left(-\pi/2,\varphi_{\mathrm{Wle}},\pi/2\right) & {}_{(\mathrm{Ax})}\boldsymbol{r}_{\mathrm{Wle}} \\ \hline \boldsymbol{0} & 1 \end{array}\right], \quad \text{with } {}_{(\mathrm{Ax})}\boldsymbol{r}_{\mathrm{Wle}}^{\mathrm{T}} = \begin{bmatrix} 0 & -y_{\mathrm{W_S}} & 0 \end{bmatrix}, \tag{4.21}$$

$${}^{\mathrm{Ax}}\boldsymbol{T}_{\mathrm{Cri}} = \left[\begin{array}{c|c} \boldsymbol{R}\left(0,\delta_{\mathrm{Cri}},0\right) & {}_{(\mathrm{Ax})}\boldsymbol{r}_{\mathrm{Cri}} \\ \hline \boldsymbol{0} & 1 \end{array}\right], \quad \text{with } {}_{(\mathrm{Ax})}\boldsymbol{r}_{\mathrm{Cri}}^{\mathrm{T}} = \begin{bmatrix} 0 & y_{\mathrm{Cri}} & z_{\mathrm{Cri}} \end{bmatrix}, \tag{4.22}$$

$${}^{\mathrm{Ax}}\boldsymbol{T}_{\mathrm{Cle}} = \left[\begin{array}{c|c} \boldsymbol{R}\left(0,\delta_{\mathrm{Cle}},0\right) & {}_{(\mathrm{Ax})}\boldsymbol{r}_{\mathrm{Cle}} \\ \hline \boldsymbol{0} & 1 \end{array}\right], \quad \text{with } {}_{(\mathrm{Ax})}\boldsymbol{r}_{\mathrm{Cle}}^{\mathrm{T}} = \begin{bmatrix} 0 & y_{\mathrm{Cle}} & z_{\mathrm{Cle}} \end{bmatrix}, \tag{4.23}$$

$${}^{0}\boldsymbol{T}_{\mathrm{Wri}} = {}^{0}\boldsymbol{T}_{\mathrm{Ax}}\,{}^{\mathrm{Ax}}\boldsymbol{T}_{\mathrm{Wri}}, \tag{4.24}$$

$${}^{0}\boldsymbol{T}_{\mathrm{Wle}} = {}^{0}\boldsymbol{T}_{\mathrm{Ax}}\,{}^{\mathrm{Ax}}\boldsymbol{T}_{\mathrm{Wle}}, \tag{4.25}$$

$${}^{0}\boldsymbol{T}_{\mathrm{Cri}} = {}^{0}\boldsymbol{T}_{\mathrm{Ax}}\,{}^{\mathrm{Ax}}\boldsymbol{T}_{\mathrm{Cri}}, \tag{4.26}$$

$${}^{0}\boldsymbol{T}_{\mathrm{Cle}} = {}^{0}\boldsymbol{T}_{\mathrm{Ax}}\,{}^{\mathrm{Ax}}\boldsymbol{T}_{\mathrm{Cle}}. \tag{4.27}$$

Please note, the rotational velocities of the right and left wheel are $\omega_{\mathrm{Wri}} = \dot{\varphi}_{\mathrm{Wri}}$ and $\omega_{\mathrm{Wle}} = \dot{\varphi}_{\mathrm{Wle}}$, respectively.

Rigid body position and velocity vectors

It is assumed that the rigid body centers of gravity $\mathrm{S_{Ax}}$, $\mathrm{S_{Wri}}$, and $\mathrm{S_{Wle}}$ lie at the origins of the corresponding body CF. Thus, position and velocity vectors of the rigid body centers of gravity can be obtained by picking the 4^{th} column of the appropriate homogeneous transformations matrices, i. e.

Axle body:
$$ {}_{(0)}\tilde{\boldsymbol{r}}_{\mathrm{S_{Ax}}} = \begin{bmatrix} {}_{(0)}\boldsymbol{r}_{\mathrm{S_{Ax}}}^{\mathrm{T}} & 1 \end{bmatrix}^{\mathrm{T}} = {}^{0}\boldsymbol{T}_{\mathrm{Ax(Ax)}}\tilde{\boldsymbol{r}}_{\mathrm{Ax}} = {}^{0}\boldsymbol{T}_{\mathrm{Ax}} \begin{bmatrix} \boldsymbol{0} & 1 \end{bmatrix}^{\mathrm{T}}, \tag{4.28} $$
$$ {}_{(0)}\dot{\tilde{\boldsymbol{r}}}_{\mathrm{S_{Ax}}} = {}^{0}\dot{\boldsymbol{T}}_{\mathrm{Ax}} \begin{bmatrix} \boldsymbol{0} & 1 \end{bmatrix}^{\mathrm{T}}, \tag{4.29} $$

Wheel right/left:
$$ {}_{(0)}\tilde{\boldsymbol{r}}_{\mathrm{S_{W}}j} = {}^{0}\boldsymbol{T}_{\mathrm{W}j} \begin{bmatrix} \boldsymbol{0} & 1 \end{bmatrix}^{\mathrm{T}}, \tag{4.30} $$
$$ {}_{(0)}\dot{\tilde{\boldsymbol{r}}}_{\mathrm{S_{W}}j} = {}^{0}\dot{\boldsymbol{T}}_{\mathrm{W}j} \begin{bmatrix} \boldsymbol{0} & 1 \end{bmatrix}^{\mathrm{T}}, \qquad j \in \{\mathrm{ri}, \mathrm{le}\}\,. \tag{4.31} $$

Rigid body rotational velocities

The rotational velocities of the rigid bodies are calculated using the property

$$ {}_{(0)}\dot{\tilde{\boldsymbol{r}}}_{\mathrm{P}} = {}^{0}\dot{\boldsymbol{T}}_{\mathrm{Ax(Ax)}}\tilde{\boldsymbol{r}}_{\mathrm{P}}, \tag{4.32a} $$
$$ = {}^{0}\dot{\boldsymbol{T}}_{\mathrm{Ax}} \left({}^{0}\boldsymbol{T}_{\mathrm{Ax}}\right)^{-1} {}_{(0)}\tilde{\boldsymbol{r}}_{\mathrm{P}}, \tag{4.32b} $$
$$ = \left[\begin{array}{c|c} {}^{0}\dot{\boldsymbol{R}}_{\mathrm{Ax}} \left({}^{0}\boldsymbol{R}_{\mathrm{Ax}}\right)^{\mathrm{T}} & {}_{(0)}\dot{\boldsymbol{r}}_{\mathrm{Ax}} - {}^{0}\dot{\boldsymbol{R}}_{\mathrm{Ax}} \left({}^{0}\boldsymbol{R}_{\mathrm{Ax}}\right)^{\mathrm{T}} {}_{(0)}\boldsymbol{r}_{\mathrm{Ax}} \\ \hline \boldsymbol{0} & 1 \end{array}\right] {}_{(0)}\tilde{\boldsymbol{r}}_{\mathrm{P}}, \tag{4.32c} $$

of homogeneous transformation matrices, where ${}_{(0)}\boldsymbol{r}_{\mathrm{Ax}}$ denotes the position of the origin of the body-fixed coordinate frame $(\mathrm{CF})_{\mathrm{Ax}}$ described in $(\mathrm{CF})_{0}$. From (4.32c), it is easy to see that the equalities

$$ {}_{(0)}\dot{\boldsymbol{r}}_{\mathrm{P}} = {}_{(0)}\dot{\boldsymbol{r}}_{\mathrm{Ax}} - {}^{0}\dot{\boldsymbol{R}}_{\mathrm{Ax}} \left({}^{0}\boldsymbol{R}_{\mathrm{Ax}}\right)^{\mathrm{T}} {}_{(0)}\boldsymbol{r}_{\mathrm{AxP}} = {}_{(0)}\dot{\boldsymbol{r}}_{\mathrm{Ax}} - {}_{(0)}\boldsymbol{\omega}_{\mathrm{Ax}} \times {}_{(0)}\boldsymbol{r}_{\mathrm{AxP}}, \tag{4.33} $$

hold. Therefore, the rotational velocity ${}_{(0)}\boldsymbol{\omega}_{\mathrm{Ax}}$ of the wheel carrier can be obtained from

$$ {}_{(0)}\boldsymbol{\omega}_{\mathrm{Ax}} = {}_{(0)}\begin{bmatrix} \omega_x \\ \omega_y \\ \omega_z \end{bmatrix}_{\mathrm{Ax}}, \quad \text{with } {}^{0}\dot{\boldsymbol{R}}_{\mathrm{Ax}} \left({}^{0}\boldsymbol{R}_{\mathrm{Ax}}\right)^{\mathrm{T}} = {}_{(0)}\begin{bmatrix} 0 & -\omega_z & \omega_y \\ \omega_z & 0 & -\omega_x \\ -\omega_y & \omega_x & 0 \end{bmatrix}_{\mathrm{Ax}}, \tag{4.34} $$

and the rotational velocities of the right wheel ${}_{(0)}\boldsymbol{\omega}_{\mathrm{Wri}}$ and the left wheel ${}_{(0)}\boldsymbol{\omega}_{\mathrm{Wle}}$ are determined by similar expressions [HAOR15].

Non-conservative forces and moments

To account for the creep forces in the wheel-rail contacts and for the motor moments, non-conservative forces need to be considered. The forces between running gear and car body are strongly reduced in lateral and vertical direction due to the secondary suspension. Forces in the longitudinal direction are taken into account in ${}_{(0)}\boldsymbol{F}_{\mathrm{Train}}$. To this end, the generalized forces $\boldsymbol{F}_{\mathrm{gen}}$ are determined by

$$\begin{aligned}\boldsymbol{F}_{\mathrm{gen}} = &\left(\frac{\partial_{(0)}\boldsymbol{r}_{\mathrm{Cri}}}{\partial \boldsymbol{q}}\right)^{\mathrm{T}} {}_{(0)}\boldsymbol{F}_{\mathrm{Cri}} + \left(\frac{\partial_{(0)}\boldsymbol{\omega}_{\mathrm{Wri}}}{\partial \dot{\boldsymbol{q}}}\right)^{\mathrm{T}} {}_{(0)}\boldsymbol{M}_{\mathrm{Wri}} \\ &+ \left(\frac{\partial_{(0)}\boldsymbol{r}_{\mathrm{Cle}}}{\partial \boldsymbol{q}}\right)^{\mathrm{T}} {}_{(0)}\boldsymbol{F}_{\mathrm{Cle}} + \left(\frac{\partial_{(0)}\boldsymbol{\omega}_{\mathrm{Wle}}}{\partial \dot{\boldsymbol{q}}}\right)^{\mathrm{T}} {}_{(0)}\boldsymbol{M}_{\mathrm{Wle}} + \left(\frac{\partial_{(0)}\boldsymbol{r}_{\mathrm{S_{Ax}}}}{\partial \boldsymbol{q}}\right)^{\mathrm{T}} {}_{(0)}\boldsymbol{F}_{\mathrm{Train}},\end{aligned} \tag{4.35}$$

where ${}_{(0)}\boldsymbol{r}_{\mathrm{Cri}}$ and ${}_{(0)}\boldsymbol{r}_{\mathrm{Cle}}$ are the positions of the wheel-rail contacts on the right and left side, respectively. The vector of generalized coordinates is denoted $\boldsymbol{q}$. In the current analysis, the vectors are defined by

$${}_{(0)}\tilde{\boldsymbol{r}}_{\mathrm{C}j} = {}^{0}\boldsymbol{T}_{\mathrm{C}j}\begin{bmatrix}\boldsymbol{0} & 1\end{bmatrix}^{\mathrm{T}}, \quad \text{for } j \in \{\mathrm{r},\mathrm{l}\}, \tag{4.36}$$

in which the variables $y_{\mathrm{C}j}$ and $z_{\mathrm{C}j}$ are dependent on the current state (see (4.22), (4.23) and section 4.1.3). The generalized forces in (4.35) are

$${}_{(0)}\boldsymbol{F}_{\mathrm{Train}} = {}^{0}\boldsymbol{R}_{\mathrm{Ax}} \; {}_{(\mathrm{Ax})}\begin{bmatrix} m_{\mathrm{CB}}/2\;\ddot{x} \\ 0 \\ 0 \end{bmatrix}, \tag{4.37}$$

$${}_{(0)}\boldsymbol{F}_{\mathrm{C}j} = {}^{0}\boldsymbol{R}_{\mathrm{C}j}\; F_{\mathrm{N}} abG \begin{bmatrix} c_{11_j} & 0 & 0 \\ 0 & c_{22_j} & 0 \\ 0 & 0 & 0 \end{bmatrix} {}_{(\mathrm{C}j)}\begin{bmatrix} s_{x_j} \\ s_{y_j} \\ \Psi_j \end{bmatrix}, \tag{4.38}$$

$${}_{(0)}\boldsymbol{M}_{\mathrm{W}j} = {}^{0}\boldsymbol{R}_{\mathrm{W}j} \; {}_{(\mathrm{W}j)}\begin{bmatrix} 0 \\ \tau_j \\ 0 \end{bmatrix}, \quad \text{for } j \in \{\mathrm{r},\mathrm{l}\}, \tag{4.39}$$

where ${}_{(0)}\boldsymbol{F}_{\mathrm{C}j}$ is modeled using linear Kalker theory [Kal82] and neglecting creep torque as well as spin creepage. G is the shear modulus of the contact materials and a and b are the contact ellipse half axis lengths. The normal force in the wheel-rail contacts is approximated by $F_{\mathrm{N}} = m_{\mathrm{Ax}}/2 + m_{\mathrm{W}} + m_{\mathrm{CB}}/2$ with the rigid body masses m_{Ax}, $m_{\mathrm{W}} = m_{\mathrm{Wri}} = m_{\mathrm{Wle}}$ and the total mass of the car body m_{CB}. The corresponding slip values s_{x_j} and s_{y_j} are assumed to

be the referred velocities of wheel particles at the contact points, i. e. ,

$$ {}_{(\mathrm{C}j)}\begin{bmatrix} s_{x_j} \\ s_{y_j} \\ * \end{bmatrix} v_{\mathrm{ref}} = {}^{\mathrm{C}j}\boldsymbol{R}_0 \left({}_{(0)}\dot{\boldsymbol{r}}_{\mathrm{Ax}} + {}_{(0)}\boldsymbol{\omega}_{\mathrm{W}j} \times {}_{(0)}\boldsymbol{r}_{\mathrm{AxC}j} \right), \tag{4.40} $$

since the underground is not moving.

LAGRANGE formalism

Using the above definitions, the kinetic energy E_{T}, the potential energy E_{V}, and the LAGRANGIAN $\mathcal{L}$ are defined. A dissipation function E_{D} is used to account for damping [HN97]. Please note, that the definitions (4.45) through (4.47) differ from those presented in the scientific publication. The quantities $r_{\mathrm{C}j}$, $y_{\mathrm{C}j}$, $\delta_{\mathrm{C}j}$, φ and z are assumed to be fully dependent on the planar position and orientation due to the geometrical wheel-rail relationship (see section 4.1.3). The remaining length y_{WS} is a fixed parameter. Hence, the generalized coordinate vector and its derivative

$$ \boldsymbol{q}^{\mathrm{T}} = \begin{bmatrix} x & y & \psi & \varphi_{\mathrm{Wri}} & \varphi_{\mathrm{Wle}} \end{bmatrix}, \tag{4.41} $$

$$ \dot{\boldsymbol{q}}^{\mathrm{T}} = \begin{bmatrix} \dot{x} & \dot{y} & \dot{\psi} & \omega_{\mathrm{Wri}} & \omega_{\mathrm{Wle}} \end{bmatrix}, \tag{4.42} $$

are employed and the LAGRANGE formalism reads

$$ \frac{\mathrm{d}}{\mathrm{d}t}\left(\frac{\partial \mathcal{L}}{\partial \dot{\boldsymbol{q}}}\right) - \frac{\partial \mathcal{L}}{\partial \boldsymbol{q}} + \frac{\partial E_{\mathrm{D}}}{\partial \dot{\boldsymbol{q}}} = \boldsymbol{F}_{\mathrm{gen}}, \tag{4.43} $$

$$ \text{with } \mathcal{L} = E_{\mathrm{T}} - E_{\mathrm{V}}, \tag{4.44} $$

$$ E_{\mathrm{T}} = \frac{1}{2} \sum_{i \in \{\mathrm{Ax,Wri,Wle}\}} m_{i(0)} \dot{\boldsymbol{r}}^{\mathrm{T}}_{\mathrm{S}_i(0)} \dot{\boldsymbol{r}}_{\mathrm{S}_i} + \frac{1}{2} {}_{(0)}\boldsymbol{\omega}^{\mathrm{T}}_{i\,(0)} \boldsymbol{J}^{(\mathrm{S}_i)}_{i\,(0)} \boldsymbol{\omega}_i, \tag{4.45} $$

$$ E_{\mathrm{V}} = \frac{1}{2} \left(\boldsymbol{q} - \boldsymbol{q}_0\right)^{\mathrm{T}} \boldsymbol{K}_{\mathrm{s}} \left(\boldsymbol{q} - \boldsymbol{q}_0\right) + \sum_{i \in \{\mathrm{Ax,Wri,Wle}\}} m_{i(0)} \boldsymbol{g}^{\mathrm{T}}{}_{(0)} \boldsymbol{r}_{\mathrm{S}_i}, \tag{4.46} $$

$$ E_{\mathrm{D}} = \frac{1}{2} \left(\dot{\boldsymbol{q}} - \dot{\boldsymbol{q}}_0\right)^{\mathrm{T}} \boldsymbol{K}_{\mathrm{d}} \left(\dot{\boldsymbol{q}} - \dot{\boldsymbol{q}}_0\right). \tag{4.47} $$

The matrix $\boldsymbol{F}_{\mathrm{gen}}$ describes generalized forces and moments according to (4.35). The matrices $\boldsymbol{K}_{\mathrm{s}}$ and $\boldsymbol{K}_{\mathrm{d}}$ include spring and damping effects, respectively. The quantities $\boldsymbol{q}_0$ and $\dot{\boldsymbol{q}}_0$ are the relative generalized coordinates around which spring and damping forces occur. The quantities ψ_{CB} and $\dot{\psi}_{\mathrm{CB}}$, which are defined in the scientific publication, contribute to $\boldsymbol{q}_0$ and $\dot{\boldsymbol{q}}_0$.

Solving for $\ddot{\boldsymbol{q}}$ yields the desired equations of motion for state vector $\boldsymbol{x} \in \mathbb{R}^n$ and input vector $\boldsymbol{u} \in \mathbb{R}^m$. For convenience, cartesian coordinates in the inertial frame are used for derivation so far. For the subsequent modeling, a change of coordinates is performed with

$$ {}_{(0)}\dot{x} = {}_{(\mathrm{Ax})}\dot{x} \cos\psi - {}_{(\mathrm{Ax})}\dot{y} \sin\psi, \tag{4.48} $$

$$ {}_{(0)}\dot{y} = {}_{(\mathrm{Ax})}\dot{x} \sin\psi + {}_{(\mathrm{Ax})}\dot{y} \cos\psi, \tag{4.49} $$

which allows to define the continuous time state space system $\boldsymbol{f} : \mathbb{R}^n \times \mathbb{R}^m \to \mathbb{R}^n$ in dependence of time-varying parameters θ. In detail,

$$ \dot{\boldsymbol{x}}(t) = \boldsymbol{f}\left(\boldsymbol{x}(t), \boldsymbol{u}(t), \theta(t)\right), \tag{4.50} $$

$$ \text{with } \boldsymbol{x}^{\mathrm{T}} = \begin{bmatrix} {}_{(\mathrm{Ax})}x & {}_{(0)}\psi & {}_{(\mathrm{Ax})}\dot{x} & {}_{(\mathrm{Ax})}\dot{y} & {}_{(0)}\dot{\psi} & {}_{(\mathrm{Ax})}\omega_{\mathrm{Wri}} & {}_{(\mathrm{Ax})}\omega_{\mathrm{Wle}} & {}_{(\mathrm{Tr})}y_{\mathrm{Ax}} & {}_{(\mathrm{Tr})}\psi_{\mathrm{Ax}} \end{bmatrix}, \tag{4.51} $$

$$ \boldsymbol{u}^{\mathrm{T}} = \begin{bmatrix} \tau_{\mathrm{r}} & \tau_{\mathrm{l}} \end{bmatrix}, \tag{4.52} $$

$$ \theta = \left\{ \mathcal{E}_{\mathrm{Tr}}, \mathcal{C}_{\mathrm{Tr}}, \mathcal{F}_{\mathrm{Train}} \right\}, \tag{4.53} $$

$$ \mathcal{E}_{\mathrm{Tr}} = \left\{ \psi_{\mathrm{Tr}}, \tfrac{\partial \psi_{\mathrm{Tr}}}{\partial s}, \varphi_{\mathrm{Tr}}, \tfrac{\partial \varphi_{\mathrm{Tr}}}{\partial s} \right\}, \tag{4.54} $$

$$ \mathcal{C}_{\mathrm{Tr}} = \left\{ c_{11_{\mathrm{r}}}, c_{11_{\mathrm{l}}}, c_{22_{\mathrm{r}}}, c_{22_{\mathrm{l}}} \right\}, \tag{4.55} $$

$$ \mathcal{F}_{\mathrm{Train}} = \left\{ m_{\mathrm{CB}} \right\}, \tag{4.56} $$

where the integrated velocity in riding direction ${}_{(\mathrm{Ax})}x$ approximately equals the traveled distance along the track s. The lateral and yaw displacement dynamics between $(\mathrm{CF})_{\mathrm{Tr}}$ and $(\mathrm{CF})_{\mathrm{Ax}}$ are defined

$$ {}_{(\mathrm{Tr})}\dot{\psi}_{\mathrm{Ax}} = \dot{\psi} - \dot{\psi}_{\mathrm{Tr}}, \tag{4.57} $$

$$ {}_{(\mathrm{Tr})}\dot{y}_{\mathrm{Ax}} = {}_{(\mathrm{Ax})}\dot{x} \sin {}_{(\mathrm{Tr})}\psi_{\mathrm{Ax}} + {}_{(\mathrm{Ax})}\dot{y} \cos {}_{(\mathrm{Tr})}\psi_{\mathrm{Ax}}, \tag{4.58} $$

as in the publication, but with a more detailed representation of ${}_{(\mathrm{Tr})}\dot{y}_{\mathrm{Ax}}$ in (4.58).
For use in discrete time frameworks, the above system can be discretized by means of 4^{th}-order RUNGE-KUTTA method or other suitable discretization methods. For convenience, the symbolic calculation program MAPLE is used for model derivation and discretization.

4.1.3 Wheel-Rail Interaction

After the derivation of a general system model, this section briefly discusses the relevant geometrical aspects of wheel-rail interaction. The exact position of the contact points between wheels and rails is of major importance for the determination of slip and hence the magnitude of creep forces. In connection, the position and orientation of force attack change due to the nonlinear wheel and rail geometries.
In modern MBS software, these influences are considered together with material elasticity and complex contact search methods are applied. This is not feasible for the current MPC task due to computation time restrictions. Therefore, simplified methods to account for the nonlinear wheel and rail geometries are sought. One possibility is to introduce the variables $r_{\mathrm{C}j}$, $y_{\mathrm{C}j}$, $\delta_{\mathrm{C}j}$, φ and z which fully depend on the current lateral and yaw displacement between $(\mathrm{CF})_{\mathrm{Tr}}$ and $(\mathrm{CF})_{\mathrm{Ax}}$. The displacements are denoted ${}_{(\mathrm{Tr})}y_{\mathrm{Ax}}$ and ${}_{(\mathrm{Tr})}\psi_{\mathrm{Ax}}$, respectively.
In [KSM+21], the contact angles $\delta_{\mathrm{C}j}$ and momentary wheel radii $r_{\mathrm{C}j}$ are approximated by one dimensional exponential functions solely dependent on ${}_{(\mathrm{Tr})}y_{\mathrm{Ax}}$, neglecting the yaw dependence. To increase accuracy, offline contact searches are performed in the present work by means of the wheel and rail geometries to obtain two dimensional look-up tables in ${}_{(\mathrm{Tr})}y_{\mathrm{Ax}}$ and ${}_{(\mathrm{Tr})}\psi_{\mathrm{Ax}}$. In detail, a planar cross-section of the contact situation can be set up as illustrated in Fig. A.1. Here, nominal values for rail cant and other geometrical parameters are used, but a worn system can also be considered if geometrical parameters are known. An optimization-based contact search is conducted for each point in a ${}_{(\mathrm{Tr})}y_{\mathrm{Ax}}$-${}_{(\mathrm{Tr})}\psi_{\mathrm{Ax}}$ grid. The result maps of φ and z can be seen in Fig. 4.3. Similar surfaces are obtained for contact angles $\delta_{\mathrm{C}j}$, wheel radii $r_{\mathrm{C}j}$, and lateral contact point positions $y_{\mathrm{C}j}$ (see appendix A).

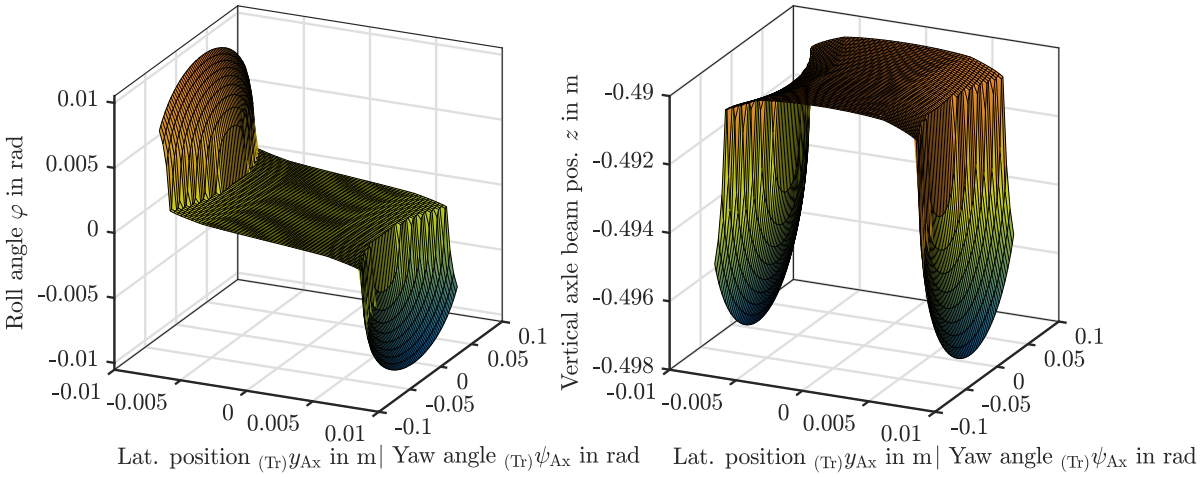

Figure 4.3: Contact search results z and φ dependent on ${}_{(\mathrm{Tr})}y_{\mathrm{Ax}}$ and ${}_{(\mathrm{Tr})}\psi_{\mathrm{Ax}}$.

4.1.4 Simplified Model

The previously developed system representation helps to understand the dynamics of the running gear plant. It offers a framework for detailed consideration of track irregularities, track path, wheel-rail adhesion conditions, and nonlinear wheel and rail geometries in a joint model. However, due to complexity and limited computational resources, using the described model in MPC remains difficult. Therefore, a simplified system representation (see chapter 3), is developed and successfully applied, whereas the results of section 4.1 form the essential basis for developments and extensions that would go beyond the scope of this conceptual work.

4.2 Control Synthesis

The general control infrastructure is described in chapter 3. However, some details concerning the adhesion-based control law are given subsequently for completeness. In addition, the implementation of the Linear Time-Variant (LTV) MPC scheme is illustrated in more detail. Lastly, the process of control parameter optimization is briefly described.

4.2.1 Adhesion-based Control

In the context of a distributed-drive train, it is meaningful to use the desired traction or braking force as a set point for a single running gear. Together with the normal contact force, the desired longitudinal adhesion f_x^* in the wheel-rail contacts can be deduced. Longitudinal controllers should aim to steer the actual adhesion f_{x_j} to this value regardless of the actual adhesion conditions $\mathcal{C}_{\mathrm{Tr}}$. If the adhesion conditions are poor and $f_{x_{\max}} < f_x^*$, the controller should steer the system to the maximum possible adhesion $f_{x_{\max}}$.
In the current thesis, unknown adhesion conditions $\mathcal{C}_{\mathrm{Tr}}$ are assumed. The controller presented in chapter 3 solely relies on the desired adhesion f_x^* and current estimates of slip $\hat{s}_{x_j}$ and adhesion $\hat{f}_{x_j}$. It alters the mean motor torque according to

$$u_k^{\mathrm{d}} = u_{k-1}^{\mathrm{d}} + \delta u, \tag{4.59}$$

where δu is determined by Algorithm 1 based on the currently encountered operational segment of the adhesion-slip curve. An overview of the operational segments can be found in Fig. 4.4. Please note, Fig. 4.4 shows a regular operation case since $f_x^* < f_{x_{\max}}$. To avoid oscillations around f_x^*, an acceptance corridor of width Δf_x^* is introduced. In the critical operation case (i. e. $f_x^* > f_{x_{\max}}$), Algorithm 1 steers the adhesion to $f_{x_{\max}}$ by switching between operational segments (I) and (VIII). To account for this case, it is crucial to carefully choose p_1 and p_2.

Algorithm 1 Adhesion-based Control

$c = \text{sign}\left(f_x^*\right)$ ▷ Traction or braking?
$\hat{f}_{x_{\text{mean}}} = \left(\hat{f}_{x_{\text{ri}}} + \hat{f}_{x_{\text{le}}}\right)/2$
if $\left|f_x^* - \hat{f}_{x_{\text{mean}}}\right| < \Delta f_x^*$ **then** ▷ Actual adhesion inside desired corridor?
  $\delta u = 0$ ▷ Control law for segment (II)-(III)
else
  if $f_x^* \hat{f}_{x_{\text{mean}}} < 0$ **then** ▷ Desired and actual adhesion in same quadrant?
    $\delta u = cp_3$ ▷ Control law for segment (IX)
  else
    if $\left(\dot{\hat{f}}_{x_{\text{ri}}} \dot{\hat{s}}_{x_{\text{ri}}} < 0\right) \vee \left(\dot{\hat{f}}_{x_{\text{le}}} \dot{\hat{s}}_{x_{\text{le}}} < 0\right)$ **then** ▷ Does macro slip occur?
      $\delta u = -cp_2$ ▷ Control law for segment (V)-(VIII)
    else
      if $f_x^* < \hat{f}_{x_{\text{mean}}}$ **then** ▷ Actual greater than desired adhesion?
        $\delta u = -cp_1$ ▷ Control law for segment (IV)
      else
        $\delta u = cp_1$ ▷ Control law for segment (I)

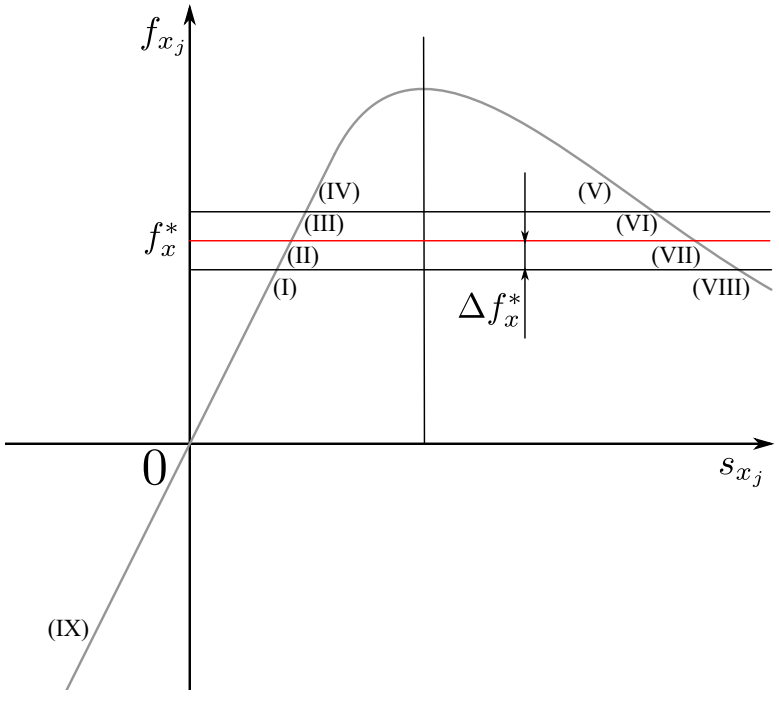

Figure 4.4: Adhesion-slip characteristic (gray) with operational segments (I)-(IX) of the presented adhesion-based controller.

Moreover, Algorithm 1 is only one possible implementation for use of the switching boundaries introduced in Fig. 4.4. Other algorithms which distinguish between the operational segments in more detail are possible. Hence, the number and choice of control parameters can vary. For full customization of δu based on the current operational segment, a truth table and appropriate logical statements can be employed.

4.2.2 Linear Time-Variant Model Predictive Control

The Linear Time-Variant Model Predictive Control (LTV-MPC) for lateral guidance is introduced in chapter 3. It employs the control-oriented model presented in the publication which is linearized about the nominal state $\boldsymbol{x}_{\mathrm{lin}_k}$ and input values $\boldsymbol{u}_{\mathrm{n}}$. Thus, it is computationally less demanding than the Nonlinear Model Predictive Control (NMPC) scheme. In this context, a quadratic optimization problem of the form

$$\min_{\boldsymbol{z}} \ \boldsymbol{z}^{\mathrm{T}}\boldsymbol{H}\boldsymbol{z} + \boldsymbol{g}^{\mathrm{T}}\boldsymbol{z}, \tag{4.60a}$$

$$\text{s.t. } \boldsymbol{A}\boldsymbol{z} \leq \boldsymbol{b}, \tag{4.60b}$$

$$\boldsymbol{A}_{\mathrm{eq}}\boldsymbol{z} = \boldsymbol{b}_{\mathrm{eq}}, \tag{4.60c}$$

is solved repetitively. For completeness, the process to construct appropriate vectors and matrices is described subsequently. Since the difference between the predicted states and the desired states is to be minimized, $\boldsymbol{z} \in \mathbb{R}^{n(L+1)+L}$ is defined as

$$\boldsymbol{z} = \begin{bmatrix} \boldsymbol{z}_{x_0} \\ \vdots \\ \boldsymbol{z}_{x_L} \\ \boldsymbol{z}_{u_0} \\ \vdots \\ \boldsymbol{z}_{u_{L-1}} \end{bmatrix} = \begin{bmatrix} \bar{\boldsymbol{x}}_0(t) - \boldsymbol{x}_0^{\mathrm{d}}(t) \\ \vdots \\ \bar{\boldsymbol{x}}_L(t) - \boldsymbol{x}_L^{\mathrm{d}}(t) \\ \Delta\bar{u}_0(t) \\ \vdots \\ \Delta\bar{u}_{L-1}(t) \end{bmatrix}. \tag{4.61}$$

The block diagonal matrix $\boldsymbol{H} \in \mathbb{R}^{(n(L+1)+L)\times(n(L+1)+L)}$ and the vector $\boldsymbol{g} \in \mathbb{R}^{n(L+1)+L}$ are

$$\boldsymbol{H} = \begin{bmatrix} \boldsymbol{Q} & & & & & \\ & \ddots & & & & \\ & & \boldsymbol{Q} & & & \\ & & & R & & \\ & & & & \ddots & \\ & & & & & R \end{bmatrix}, \qquad \boldsymbol{g} = \boldsymbol{0}. \tag{4.62}$$

Please note, the quantities used are defined in the scientific publication. To impose the linearized system model by means of the equality constraints (4.60c), a suitable form has to be obtained. To this end, the linearized system can be expressed as

$$\bar{\boldsymbol{x}}_{k+1}(t) = \boldsymbol{x}_{\mathrm{lin}_{k+1}}(t) + \bar{\boldsymbol{x}}_{\mathrm{diff}_{k+1}}(t), \tag{4.63a}$$

$$= \boldsymbol{x}_{\mathrm{lin}_{k+1}}(t) + \boldsymbol{A}_k \left(\bar{\boldsymbol{x}}_k(t) - \boldsymbol{x}_{\mathrm{lin}_k}(t)\right) + \boldsymbol{b}_{1_k} \left(\Delta\bar{u}_k(t) - 0\right) + \boldsymbol{b}_{2_k} \left(u_k^{\mathrm{d}}(t) - 0\right) \tag{4.63b}$$

where $\bar{\boldsymbol{x}}_{\mathrm{diff}_k}(t)$ is the difference between the linearization point and the current predicted state. The JACOBIANS of states and inputs are

$$\boldsymbol{A}_k = \left.\frac{\partial \boldsymbol{f}_{\mathrm{d}}}{\partial \boldsymbol{x}}\right|_{\boldsymbol{x}=\boldsymbol{x}_{\mathrm{lin}_k}, \boldsymbol{u}=\boldsymbol{0}, \theta=\theta_{\mathrm{lin}_k}}, \tag{4.64}$$

$$\boldsymbol{b}_{1_k} = \left.\frac{\partial \boldsymbol{f}_{\mathrm{d}}}{\partial \Delta\bar{u}}\right|_{\boldsymbol{x}=\boldsymbol{x}_{\mathrm{lin}_k}, \boldsymbol{u}=\boldsymbol{0}, \theta=\theta_{\mathrm{lin}_k}}, \quad \boldsymbol{b}_{2_k} = \left.\frac{\partial \boldsymbol{f}_{\mathrm{d}}}{\partial u^{\mathrm{d}}}\right|_{\boldsymbol{x}=\boldsymbol{x}_{\mathrm{lin}_k}, \boldsymbol{u}=\boldsymbol{0}, \theta=\theta_{\mathrm{lin}_k}}, \tag{4.65}$$

$$\boldsymbol{u} = \begin{bmatrix} u^{\mathrm{d}} + \Delta\bar{u} \\ u^{\mathrm{d}} - \Delta\bar{u} \end{bmatrix}, \tag{4.66}$$

where the mean input torque u^{d} is separated from the differential torque $\Delta\bar{u}$. The remaining quantities are defined in chapter 3. Using the definition of $\boldsymbol{z}$ in (4.61), the equation

$$\begin{aligned} &\begin{bmatrix} \dots & \mathbf{I} & -\boldsymbol{A}_k & \dots & -\boldsymbol{b}_{1_k} & \dots \end{bmatrix} \begin{bmatrix} \vdots \\ \bar{\boldsymbol{x}}_{k+1}(t) - \boldsymbol{x}_{k+1}^{\mathrm{d}}(t) \\ \bar{\boldsymbol{x}}_k(t) - \boldsymbol{x}_k^{\mathrm{d}}(t) \\ \vdots \\ \Delta\bar{u}_k(t) \\ \vdots \end{bmatrix} \\ &= \left[\boldsymbol{x}_{\mathrm{lin}_{k+1}}(t) - \boldsymbol{x}_{k+1}^{\mathrm{d}} + \boldsymbol{A}_k \left(\boldsymbol{x}_k^{\mathrm{d}}(t) - \boldsymbol{x}_{\mathrm{lin}_k}(t)\right) + \boldsymbol{b}_{2_k} u_k^{\mathrm{d}}(t)\right] \end{aligned} \tag{4.67}$$

can be obtained from (4.63) which determines the k^{th} row of $\boldsymbol{A}_{\mathrm{eq}}$ and $\boldsymbol{b}_{\mathrm{eq}}$. The initial constraint $\bar{\boldsymbol{x}}_0(t) = \hat{\boldsymbol{x}}_t$ and any terminal constraints must be considered separately. Static state constraints $\boldsymbol{\mathcal{X}} = [\boldsymbol{x}_{\min}, \boldsymbol{x}_{\max}]$ are introduced by means of (4.60b) and using the shift

$$\boldsymbol{x}_{\min} \leq \bar{\boldsymbol{x}}_k(t) \leq \boldsymbol{x}_{\max} \tag{4.68}$$

$$\boldsymbol{x}_{\min} - \boldsymbol{x}_k^{\mathrm{d}}(t) \leq \boldsymbol{z}_{x_k} \leq \boldsymbol{x}_{\max} - \boldsymbol{x}_k^{\mathrm{d}}(t). \tag{4.69}$$

Static input constraints to account for actuator saturation are imposed with similar inequalities.

4.2.3 Parameter Optimization

The choice of control design parameters is of crucial importance for the control performance. In the scientific publication, multiple control parameters are defined and need to be tuned.
On the one hand, parameters can be chosen heuristically. This approach can give fast results but requires system understanding and usually leads not to the globally optimal tuning. On the other hand, optimization techniques offer the possibility to find suitable control parameter values. In the current thesis the global optimization algorithm Particle Swarm Optimization (PSO) is used, which conducts gradient-free optimization [KE95]. The simulation environment, together with the optional optimization extension, is shown in Fig. 4.5. In detail, the PSO algorithm minimizes the cost function

$$J = \sum_{v\in\{40,160,280,400\}\mathrm{km/h}} \left[\frac{1}{N} \sum_{k=1}^{N} \left\| y^{\mathrm{d}}_{\mathrm{TrAx}_k}(v) - y_{\mathrm{TrAx}_k}(v) \right\|_2 + h \left\| \Delta u_k(v) \right\|_2 \right] \tag{4.70}$$

along the optimization variables $\boldsymbol{r}^{\mathrm{T}} = \begin{bmatrix} r_1 & r_2 & r_3 & r_4 & r_5 & r_6 \end{bmatrix}$, with

Prediction horizon	$H = r_1,$	(4.71)
Number of prediction steps	$L = r_2,$	(4.72)
Prediction step size	$T = H/L,$	(4.73)
State cost matrix	$\boldsymbol{Q} = \mathrm{diag}\left(0, 0, 0, 0, 10^{r_3}, 10^{r_4}, 10^{r_5}\right),$	(4.74)
Input cost matrix	$R = 10^{-3},$	(4.75)
Terminal state cost matrix	$\boldsymbol{Q}_L = \boldsymbol{Q} \cdot \mathrm{diag}\left(0, 0, 0, 0, 0, r_6, r_6\right),$	(4.76)

and h is a weighting parameter to account for the magnitude difference between y_{TrAx} and Δu. The evaluation sequences are of length N. Multiple optimization procedures with random initialization are performed to increase the chance to find a global optimum. Thus, an extensive parameter space can be explored. To account for different operating points, the curve entering scenarios for multiple velocities with tracks $\mathcal{T}_1$ to $\mathcal{T}_4$ are used for each optimization procedure. The set point signal y^* is a ramp with a superimposed sine function.
Due to the embedded MBS software, only a single computing device could be used. In addition, the simulation process for each cost function evaluation is time consuming. In this light, a number of 100 iterations is chosen. Each optimization procedure takes approximately 48 hours using an INTEL© CORE™ i7-6700K CPU @ 4.00GHz, 16 GB RAM.

4.3 Evaluation

After all, a thorough evaluation of the previous modeling, control synthesis and parametrization choices is essential to show their effectiveness. To this end, a broad environment featuring different programs is set up and will be described in the following. Therein, an additional plant model is illustrated, which is based on the modeling language MODELICA . This model is not mentioned in the scientific publication due to limited space. The section concludes with the presentation of further experimental results, especially in the context of the MODELICA plant.

4.3.1 Programmatic Environment

The main part of the evaluation are conducted in MATLAB and SIMULINK . For representation of the plant, however, additional software is employed. Apart from simple evaluation, a parameter optimization based on MATLAB can be carried out. An overview of the programmatic framework is shown in Fig. 4.5.
To start with, the scenario settings are defined in a MATLAB preprocessing script. Here, the desired set point sequences for y^* and F_x^* are introduced. Loading of initial system and controller values as well as their parametrization take place. With regard to future work, track loading and preprocessing are optimized for use of common standards in railway research. Thus, the ideal track geometry for evaluation is loaded from an external `.trm` file (for **tr**ack **m**easurement) and the track excitations are loaded from an external `.tre` file (for **tr**ack **e**xcitation). The corresponding `.trm` and `.tre` files can contain measured data from real tracks or artificially

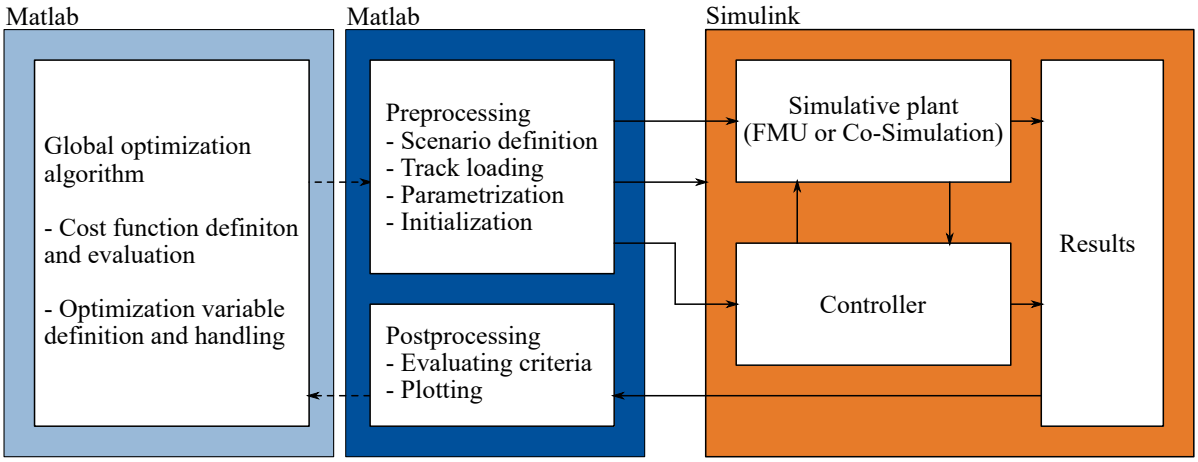

Figure 4.5: Environment for development and evaluation of the proposed control schemes in MATLAB (blue) and SIMULINK (orange), featuring an optional parameter optimization block (light blue).

generated data. In the present work, ideal evaluation track geometries are created using the MODELICA RailwayDynamics library, which has been developed at SR. Artificially sampled `.tre` excitation files from a custom PSD are computed based on section 4.1.1.
After preprocessing, SIMULINK is started where the control loop consisting of controller and detailed plant model are defined. For evaluation, two distinct plant models exist. In the publication, the state-of-the-art MBS software SIMPACK is used for a realistic plant representation by means of co-simulation. Apart from that, initial developments are made with a simplified plant model based on the modeling language MODELICA . The latter is briefly described briefly in the following paragraph.
The MODELICA implementation refers to a running gear roller rig with IRW of scale 1:5 which is presented in [KSM19]. The underlying wheel geometry of the MODELICA plant is ideally conic. For the current thesis, the model is adapted for evaluation of a single axle. It is integrated into SIMULINK by means of the standard Functional Mock-up Interface (FMI) for exchange of dynamic simulation models. FMI converts a dynamic model into a platform-independent compressed library, the Functional Mock-up Unit (FMU), with a `.xml`-file for definitions and model formulas in the form of `C`-functions [Mod22]. Parameter tables, user interfaces or documentations can be attached. If evaluation with either of the plant models is finished, results are summarized in MATLAB, performance criteria are calculated and corresponding plots are created.
Additionally, a parameter optimization can be carried out. To this end, the previously described framework is used in an objective function and certain performance criteria are used to determine the cost as described in section 4.2.3.

4.3.2 Further Results

Some exemplary results with the MODELICA plant are presented in the following. For comparison, the gain scheduled state feedback controller described in section 2.2 is employed.
In Fig. 4.6, a sine sweep set point trajectory y^* is to be followed under constant acceleration. The tracking errors of NMPC, LTV-MPC and state feedback control are in general small. However, the state feedback controller operates with a slight delay and thus greater errors in contrast to MPC schemes occur. The RMSE of the lateral position using state feedback control is $0.268\mathrm{mm}$ compared to $0.011\mathrm{mm}$ with LTV-MPC and $0.003\mathrm{mm}$ with NMPC. The RMSE difference can be explained by the incorporation of set point preview information in MPC. Moreover, the bottom plot reveals that the velocity dependency of the error is strongest with state feedback control. Since the results are calculated with the simplified MODELICA plant model, they should be used especially for methodological comparison. A quantitative comparison is conducted by means of the SIMPACK plant as shown in chapter 3 and at the end of this section.

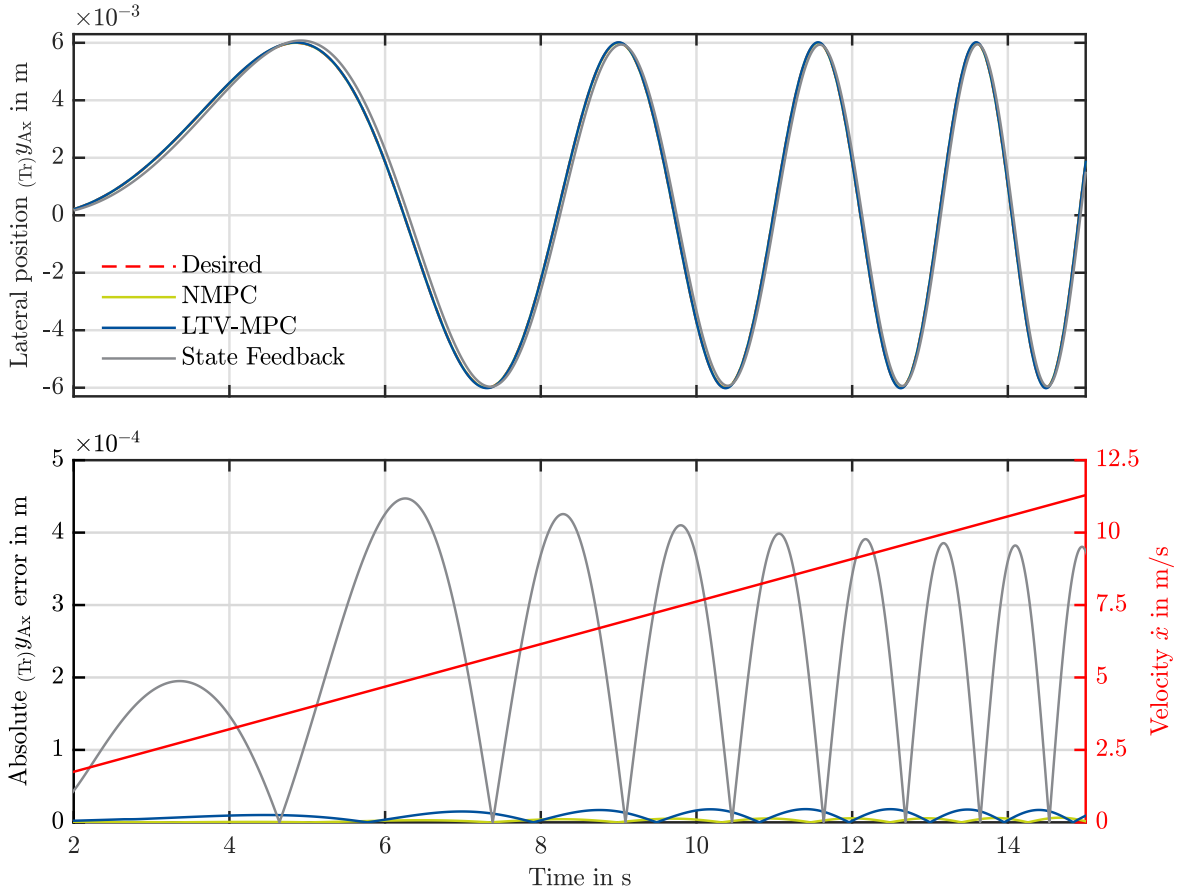

Figure 4.6: MODELICA roller rig model, moderate acceleration, good adhesion conditions, sine sweep as controller input.

Besides, a ramp function is used as lateral set point y^* to analyze additional control performance criteria (see Fig. 4.7). A ramp is chosen instead of a step function since the controllers employ numerical derivatives of y^* in their control laws. Thus, an instantaneous step would unrealistically perturb the control action. In addition, negligence of the step scenario is justified since the real track path in lateral direction (which the mechatronic guidance controller should track) is usually smooth. Experimental results show, the MPC-based lateral guidance can accurately follow the desired set point with minimal overshoot. Using gain scheduled state feedback control, a slight delay and an overshoot of 1.3% occurs in the lateral position. Furthermore, the settling time is reduced significantly if using MPC instead of state feedback control. The use of preview information can also be seen in the corresponding motor torques, where MPC induces a differential torque and hence steering action at $1.97\mathrm{s}$ even before a set point change occurs. The state feedback-based controller commands a differential torque just after the lateral position set point has changed.

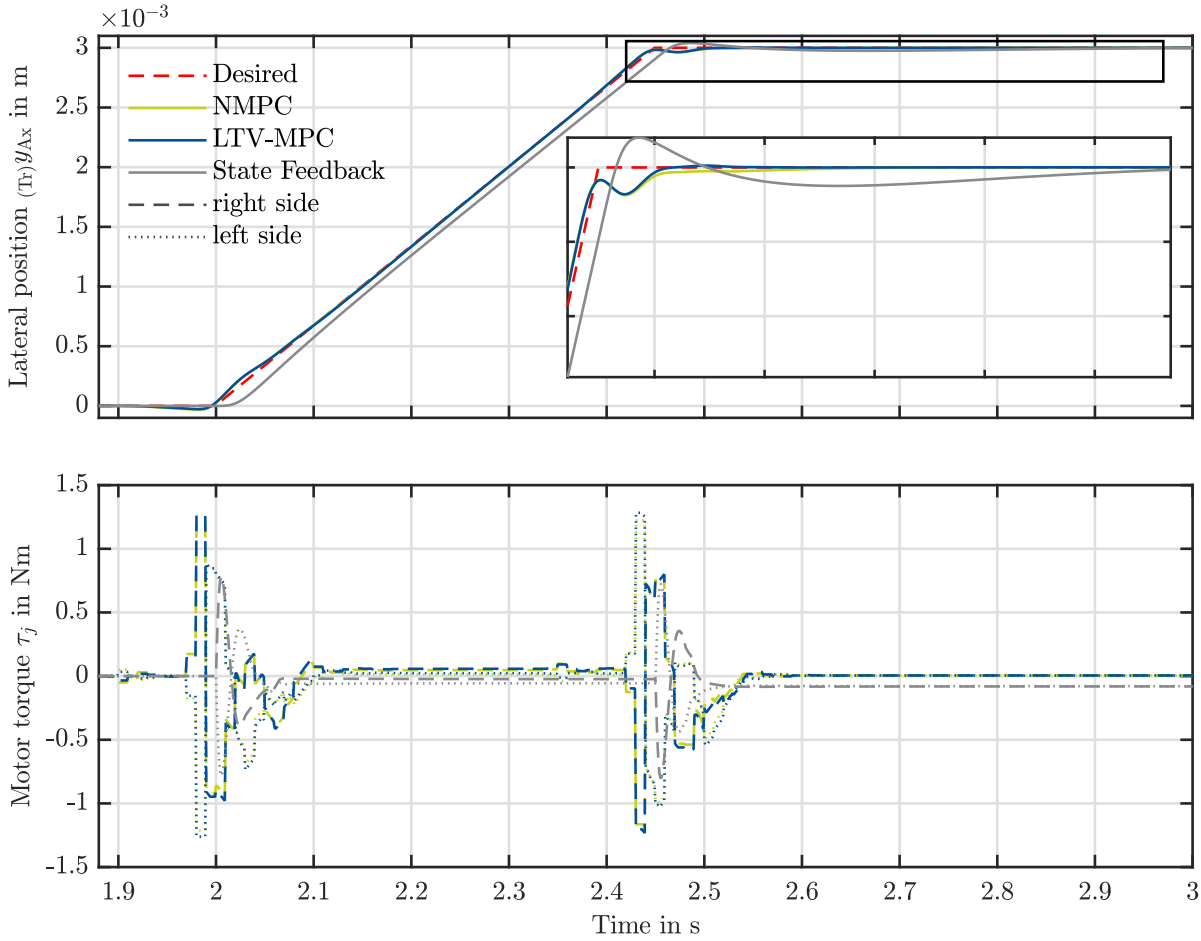

Figure 4.7: MODELICA roller rig model, $50\mathrm{km/h}$, $F_x^* = 0$, good adhesion conditions, ramp as controller input.

In Fig. 4.8, the operation of the devised adhesion-based control law is shown in combination with the gain scheduled state feedback controller. It shows, that it is in general possible to use the integration strategy and the longitudinal control law with other lateral guidance controllers as well, although the use of MPC yields specific advantages as described in chapter 3. In the scenario, the adhesion conditions in the left and right wheel-rail contact are different and change instantaneously to poor conditions at $2\mathrm{s}$. The corresponding adhesion-slip characteristics are shown in Fig. 4.9. In addition, a dynamically varying lateral position y^* is to be tracked and the set point F_x^* changes with time. As can be seen, the controller initially steers the system to the desired adhesion set point. Looking at Fig. 4.9, it is easy to see that the right wheel-rail contact requires a higher slip s_{x_j} value to provide the same longitudinal adhesion f_{x_j}. When the adhesion-slip characteristics change to poor conditions at $2\mathrm{s}$, the actual adhesion decreases rapidly. Since $f_x^* > f_{x_{\max}}$, the desired adhesion cannot be achieved and the maximum

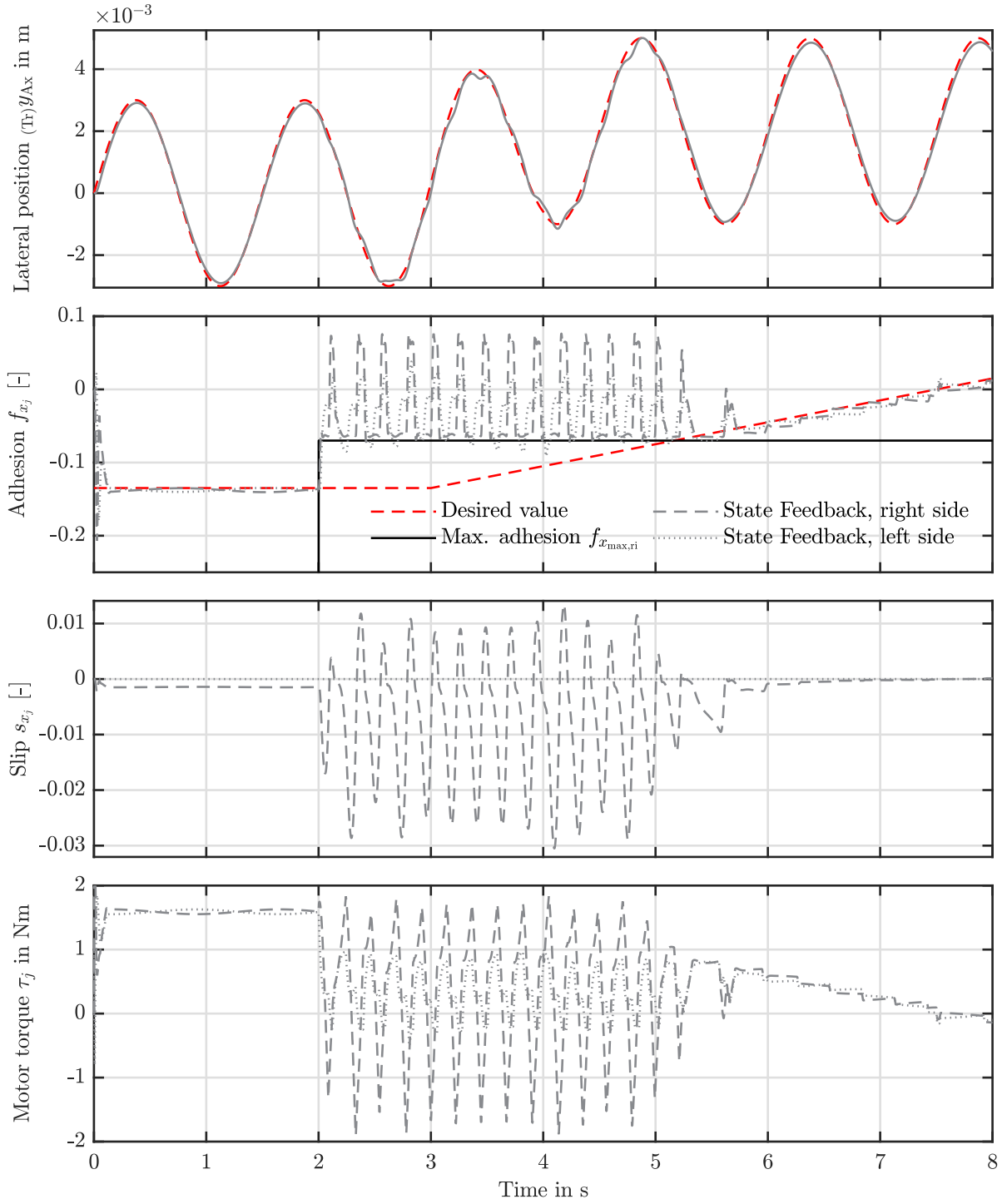

Figure 4.8: MODELICA roller rig model, 40km/h, changing braking demand, changing adhesion conditions, sine with ramp as controller input.

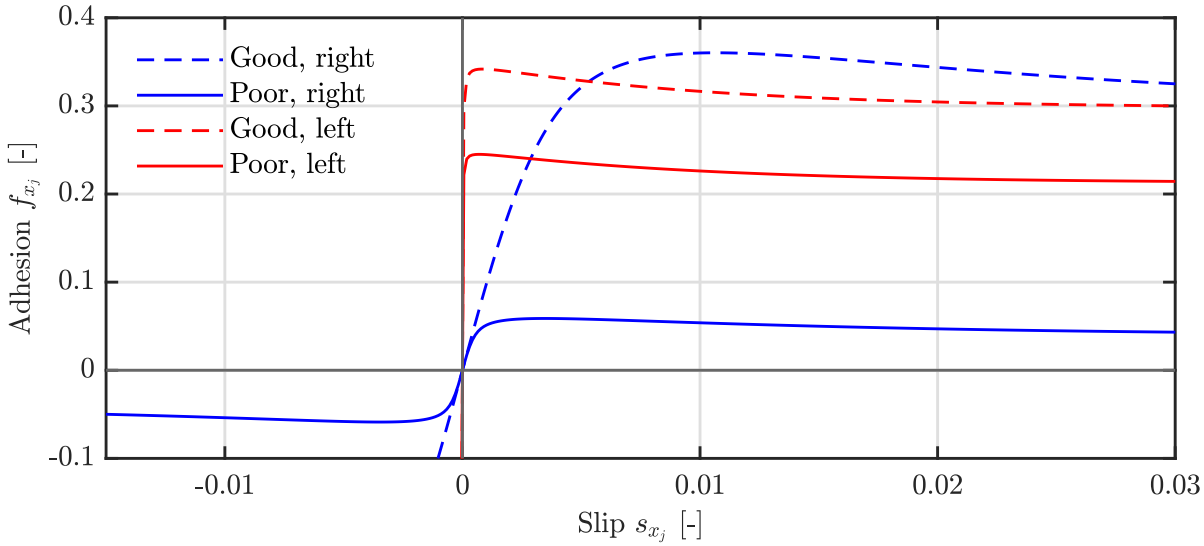

Figure 4.9: Good and poor adhesion conditions in the right and left wheel-rail contact.

value should be provided instead. By means of the adhesion-based control law presented in chapter 3, the controller drives the system to the maximum adhesion value repetitively while avoiding excessive macro slip. As soon as the desired adhesion value can be provided again at 5s (i. e. $f_x^* < f_{x_{\max}}$), the controller causes the system to follow f_x^* within a tight corridor. Therefore, the devised controller is able to operate in challenging longitudinal control situations while ensuring lateral stability and set point tracking.

The previous examples and the experimental results in chapter 3 demonstrate the theoretical applicability of the devised controller. To come one step closer to the practical application, the last scenario to be discussed includes an artificial error trajectory of the lateral position, which imitates real lateral track excitations. The trajectory is generated as described in section 4.1.1 and used as lateral set point y^*. The evaluation track itself is of ideal geometry. An implementation to consider perturbed, real tracks directly in simulation is beyond the scope of this work.

The investigation based on the SIMPACK plant proves, that the developed framework is suitable to consider known perturbations from the ideal track path. As can be seen in Fig. 4.10, the MPC-based controllers are able to accurately follow the artificial error trajectory. Comparing NMPC-based lateral control with NDI in this scenario, the RMSE of the lateral position is reduced from 2.05mm to 0.96mm. This suggests, that MPC-based integrated control is in general able to steer the system dynamically in the relevant frequency range of lateral track irregularities. Moreover, lateral guidance accuracy may be improved compared to existing control schemes.

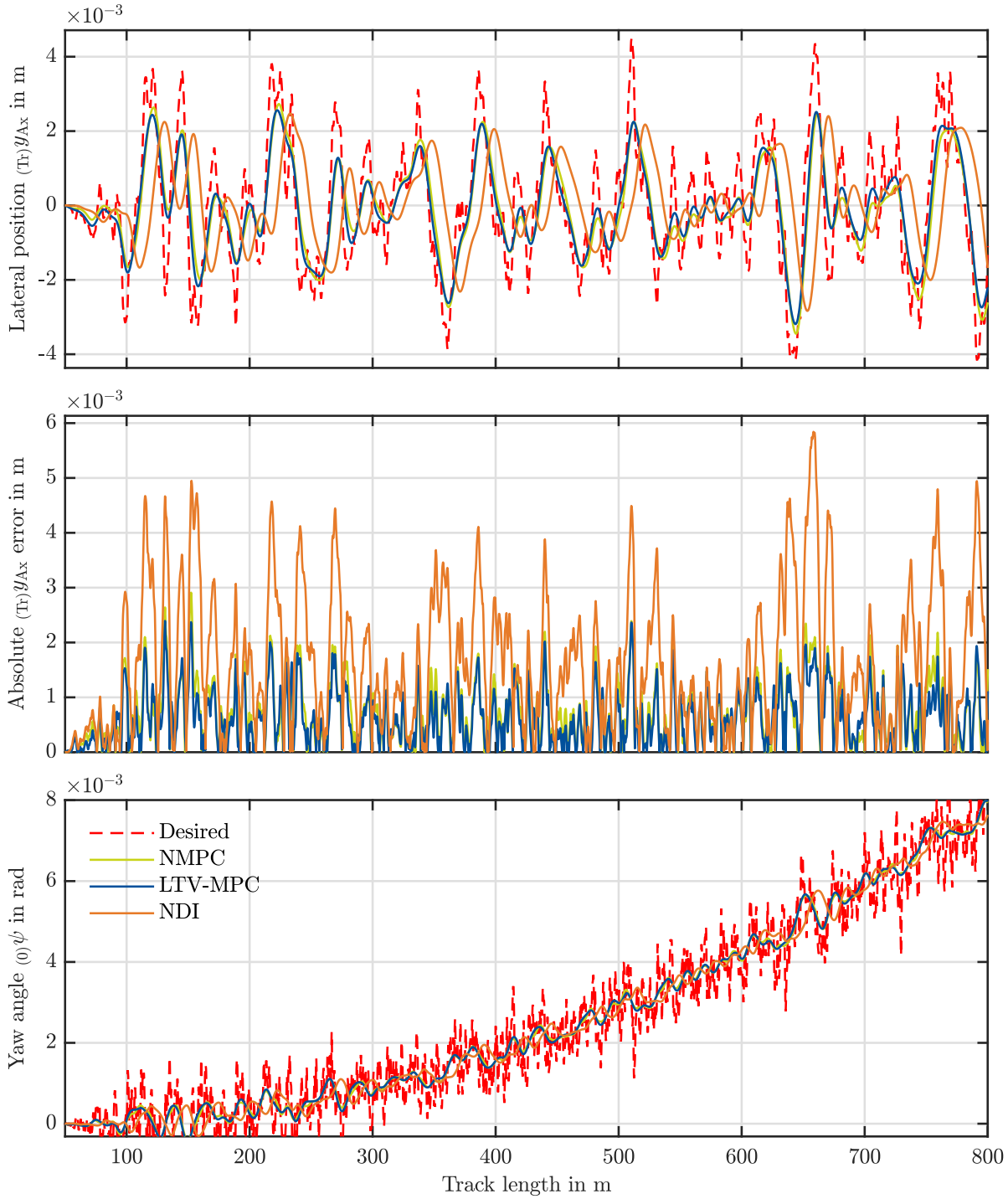

Figure 4.10: Co-simulation result, evaluation track $\mathcal{T}_4$, $400\mathrm{km/h}$, good adhesion conditions, lateral error trajectory as controller input, $F_x^* = 0$.

5 Conclusion and Outlook

In the end, a conclusion of the present work is given. It is followed by a discussion together with an outlook for future research.

5.1 Conclusion

In the current thesis, an integrated control system for joint consideration of the longitudinal and lateral dynamics of a high-speed railway running gear with IRW is developed. To this end, a framework for use of MPC in the railway context is devised.
To find a suitable predictive model, an extensive system analysis is carried out and a control-oriented model is derived. Varying quantities such as the wheel and rail geometries and the velocity are directly considered in the predictive model. Moreover, preview information about track geometry and set points is used for prediction in the model. Different MPC techniques are implemented and compared. The use of an LTV model is investigated to reduce the computational complexity and an approximate optimization time reduction to a fourth compared with NMPC is achieved. For longitudinal control, the adhesion-based system presented in [SPG21a] is extended for the general operation case and integrated with the lateral control system.
A detailed development and evaluation framework is set up and extensive simulations are carried out by means of the state-of-the-art MBS software SIMPACK. The devised system is able to safely control the railway running gear, despite influences of curving, gyroscopic effects, varying velocities, and nonlinear wheel and rail geometries. It is compared with existing control approaches which are based on gain scheduled state feedback and NDI. In both cases, the MPC-based integrated controllers show superior performance regarding lateral position error and braking distance.
In this light, the current thesis contributes a holistic framework for control of railway running gears with IRW. The control objective can be shifted smoothly between lateral and longitudinal emphasis. Service braking and traction can be performed as well as critical braking scenarios while preserving lateral stability. Due to the novelty of the devised controller and promising results, the main part of the present work is presented as a scientific publication in order to be published as a journal paper.

5.2 Outlook

The current thesis shows the applicability of MPC in the railway context. Together with a novel adhesion-based technique, an integrated controller has been developed and shows promising results for a wide range of operation conditions. However, certain aspects require special attention. Both lateral and longitudinal sub control systems come with a number of control design parameters which need to be determined. The parameters can partly influence each other, so that tuning for multiple realistic cases may be difficult. In addition, future works may focus on further refinement to consider track irregularities.

Considering the application of MPC, measures to ensure safe real-time operation need to be considered. An interesting option is the design of a centralized MPC controller for joint handling of lateral and longitudinal control. In this context, constraints regarding maximum slip and maximum adhesion might be introduced, motivated by section 2.1. As mentioned earlier, this approach relies on the detailed knowledge of the adhesion-slip characteristics such that a suitable estimation structure needs to be developed as well.

To sum up, the results of this thesis suggest that MPC-based techniques are a promising approach for integrated control of railway running gears with IRW. Future research may focus further in this area, working towards a more sustainable, efficient and safe railway transport.

Appendix

A Dependent Variables of Wheel-Rail Contacts

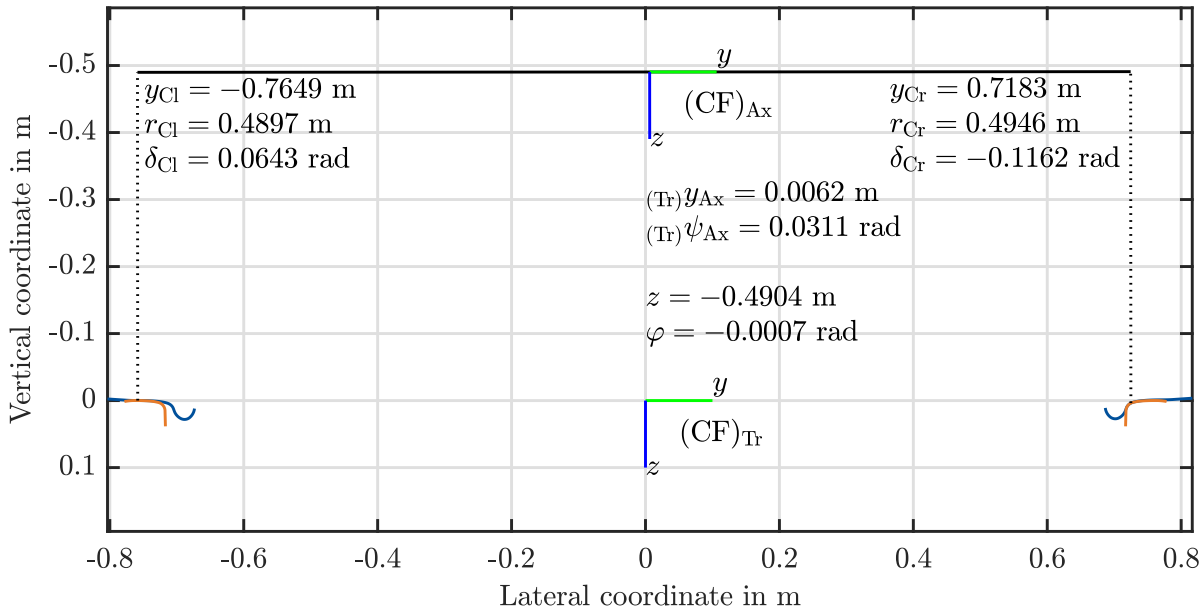

Figure A.1: Setting for optimization-based contact search between wheel and rail geometries along a grid of ${}_{(\mathrm{Tr})}y_{\mathrm{Ax}}$ and ${}_{(\mathrm{Tr})}\psi_{\mathrm{Ax}}$. Results are vertical wheel carrier position z with respect to the track frame, wheel carrier roll angle φ with respect to the track frame, wheel radii $r_{\mathrm{C}j}$, lateral contact positions $y_{\mathrm{C}j}$ and contact angles $\delta_{\mathrm{C}j}$ for $j \in \{\mathrm{ri}, \mathrm{le}\}$.

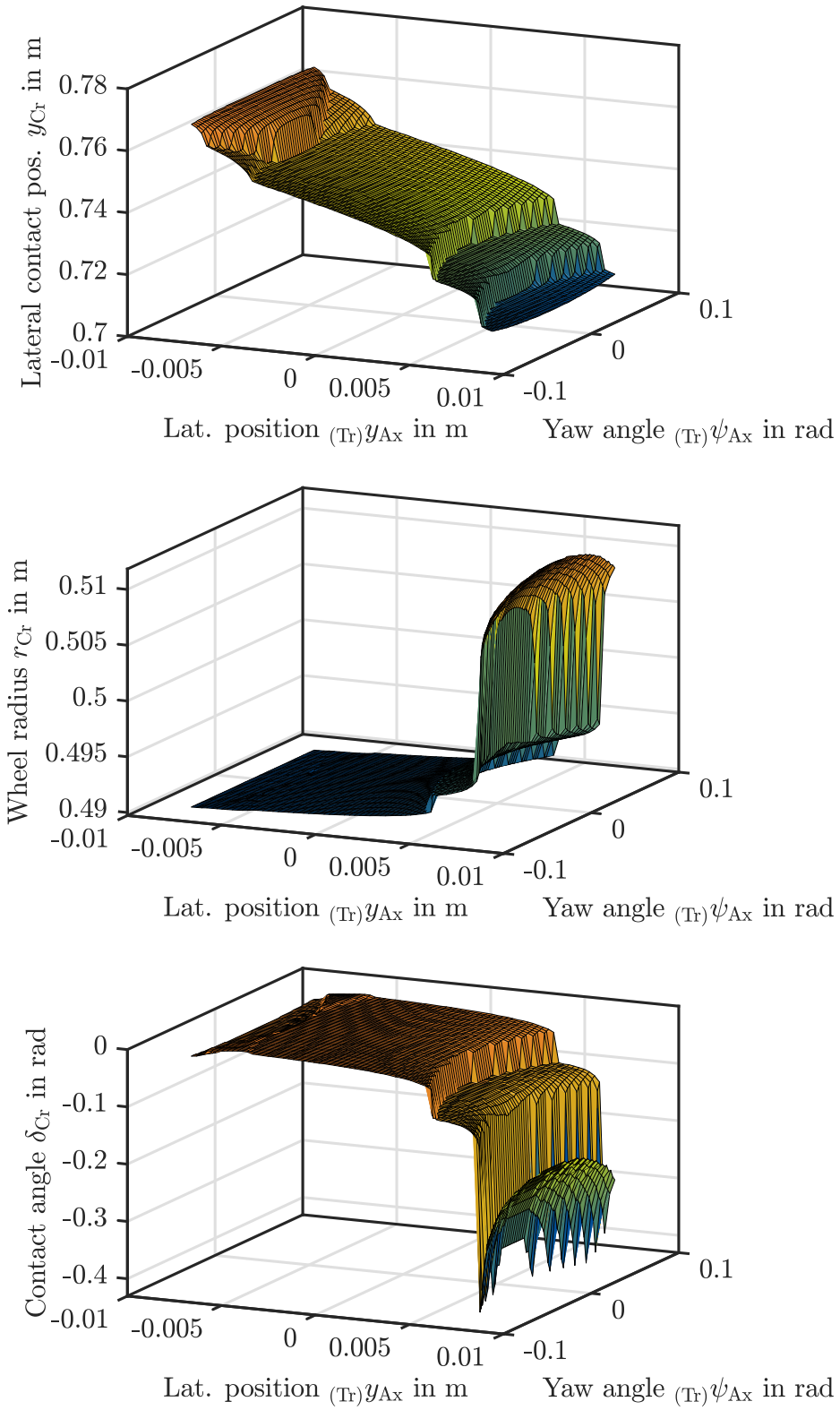

Figure A.2: Contact search results r_{Cr}, y_{Cr} and δ_{Cr} dependent on $_{(Tr)}y_{Ax}$ and $_{(Tr)}\psi_{Ax}$. Results regarding the left side are mirrored about $_{(Tr)}y_{Ax}$.

Bibliography

[Ada18] ADAMY, Jürgen: *Nichtlineare Systeme und Regelungen*. 3., bearb. u. erw. Aufl. Berlin : Springer, 2018

[AKJ20] ATAEI, Mansour ; KHAJEPOUR, Amir ; JEON, Soo: Model Predictive Control for integrated lateral stability, traction/braking control, and rollover prevention of electric vehicles. In: *Vehicle System Dynamics* 58 (2020), Nr. 1, S. 49–73

[Bun21] BUNDESTAG DER BUNDESREPUBLIK DEUTSCHLAND: *Bundes-Klimaschutzgesetz*. https://www.bmuv.de/en/law/federal-climate-change-act-bundes-klimaschutzgesetz. Version: 2021. – last accessed: 02/11/2022

[DA12] DELLMANN, Torsten ; ABDELFATTAH, Basem: Vergleich der dynamischen Eigenschaften von Radsatz und Losradpaar: Ein theoretischer Beitrag zu einer fast vergessenen Technik. In: *ZEVrail* 136 (2012), Nr. 10, S. 380–390

[Dav21] DAVID KRÜGER: *Prototypischer Radträger im Rahmen des Projekts „Forschungsinfrastruktur NGT-Fahrwerk“ (FuN)*. 2021

[Deu22a] DEUTSCHES ZENTRUM FÜR LUFT- UND RAUMFAHRT E.V.: *Forschen für den Zug der Zukunft: Hochgeschwindigkeits-Triebwagen Personenzug*. https://verkehrsforschung.dlr.de/de/projekte/ngt-hst. Version: 2022. – last accessed : 02/11/2022

[Deu22b] DEUTSCHES ZENTRUM FÜR LUFT- UND RAUMFAHRT E.V.: *Forschen für den Zug der Zukunft: NGT-FuN: Forschungsinfrastruktur NGT-Fahrwerk*. https://verkehrsforschung.dlr.de/de/projekte/ngt-fun-forschungsinfrastruktur-ngt-fahrwerk. Version: 2022. – last accessed : 02/11/2022

[DG08] DUCARD, G. ; GEERING, H. P.: Stability analysis of a dynamic inversion based pitch rate controller for an unmanned aircraft. In: *Proc. IEEE/RSJ International Conference on Intelligent Robots and Systems*, 2008, S. 360–366

[FLG08] FENG, Jinzhi ; LI, Jun ; GOODALL, R. M.: Integrated control strategies for railway vehicles with independently-driven wheel motors. In: *Frontiers of Mechanical Engineering in China* 3 (2008), Nr. 3, S. 239–250

[FTA+07] FALCONE, Paolo ; TSENG, H. E. ; ASGARI, Jahan ; BORRELLI, Francesco ; HROVAT, Davor: Integrated braking and steering model predictive control approach in autonomous vehicles. In: *IFAC Proceedings Volumes* 40 (2007), Nr. 10, S. 273–278

[GAD16] GUAY, Martin ; ADETOLA, Veronica ; DEHAAN, Darryl: *Robust and adaptive model predictive control of non-linear systems*. London, England : The Institution of Engineering and Technology, 2016

[GB02] GRETZSCHEL, Moritz ; BOSE, Lutz: A new concept for integrated guidance and drive of railway running gears. In: *Control Engineering Practice* 10 (2002), Nr. 9, S. 1013–1021

[GBM06] GOODALL, R. M. ; BRUNI, S. ; MEI, T. X.: Concepts and prospects for actively controlled railway running gear. In: *Vehicle System Dynamics* 44 (2006), Nr. sup1, S. 60–70

[GHB03] GORDON, Tim ; HOWELL, Mark ; BRANDAO, Felipe: Integrated Control Methodologies for Road Vehicles. In: *Vehicle System Dynamics* 40 (2003), Nr. 1-3, S. 157–190

[GHL19] GRETHER, Gustav ; HECKMANN, Andreas ; LOOYE, Gertjan: Lateral Guidance Control Using Information of Preceding Wheel Pairs. In: *Proc. 26th IAVSD International Symposium on Dynamics of Vehicles on Roads and Tracks*, 2019, S. 863–871

[GK90] GLADWELL, G. M. L. ; KALKER, J. J.: *Three-Dimensional Elastic Bodies in Rolling Contact*. Bd. 2. Dordrecht : Springer Netherlands, 1990

[GLH18] GRETHER, Gustav ; LOOYE, Gertjan ; HECKMANN, Andreas: Lateral guidance of independently rotating wheel pairs using feedback linearization. In: *Proc. Fourth International Conference on Railway Technology: Research, Development and Maintenance*, 2018

[HAOR15] HEIMANN, Bodo ; ALBERT, Amos ; ORTMAIER, Tobias ; RISSING, Lutz: *Mechatronik: Komponenten - Methoden - Beispiele*. München : Carl Hanser Verlag, 2015

[HKG20] HECKMANN, Andreas ; KECK, Alexander ; GRETHER, Gustav: Active Guidance of a Railway Running Gear with Independently Rotating Wheels. In: *Proc. IEEE Vehicle Power and Propulsion Conference (VPPC)*, 2020, S. 1–5

[HLGK17] HECKMANN, Andreas ; LÜDICKE, Daniel ; GRETHER, Gustav ; KECK, Alexander: From Scaled Experiments of Mechatronic Guidance to Multibody Simulations of DLR's Next Generation Train Set. In: *Proc. 25th IAVSD International Symposium on Dynamics of Vehicles on Roads and Tracks*, 2017

[HN97] HARRISON, H. R. ; NETTLETON, T.: *Advanced engineering dynamics*. London : Arnold, 1997

[HPK18] HECHT, Markus ; POLACH, Oldrich ; KLEEMANN, Ulrich: Schienenfahrzeuge. In: GROTE, Karl-Heinrich (Hrsg.) ; BENDER, Beate (Hrsg.) ; GÖHLICH, Dietmar (Hrsg.): *Dubbel*. Berlin, Heidelberg : Springer Berlin Heidelberg, 2018, S. 1210–1246

[HSB+15] HECKMANN, Andreas ; SCHWARZ, Christoph ; BÜNTE, Tilman ; KECK, Alexander ; BREMBECK, Jonathan: Control Development for the Scaled Experimental Railway Running Gear of DLR. In: *Proc. 24th IAVSD International Symposium on Dynamics of Vehicles on Roads and Tracks*, 2015

[Iwn06] IWNICKI, Simon: *Handbook of railway vehicle dynamics*. Boca Raton : CRC/Taylor & Francis, 2006

[Kal82] KALKER, Joost J.: A Fast Algorithm for the Simplified Theory of Rolling Contact. In: *Vehicle System Dynamics* 11 (1982), Nr. 1, S. 1–13

[KE95] KENNEDY, J. ; EBERHART, R.: Particle swarm optimization. In: *Proc. IEEE International Conference on Neural Networks (ICNN)*, 1995, S. 1942–1948

[KHWR14] KURZECK, Bernhard ; HECKMANN, Andreas ; WESSELER, Christoph ; RAPP, Matthias: Mechatronic track guidance on disturbed track: the trade-off between actuator performance and wheel wear. In: *Vehicle System Dynamics* 52 (2014), Nr. sup1, S. 109–124

[Kli83] KLINGEL, W.: Uber den Lauf der Eisenbahnwagen auf gerader Bahn. In: *Organ fur die Fortschritte des Eisenbahnwesens in Technischer Beziehung* (1883)

[KSM19] KECK, Alexander ; SCHWARZ, Christoph ; MEURER, Thomas: Observer design for a railway running gear with independently rotating wheels. In: *IFAC-PapersOnLine* 52 (2019), Nr. 15, S. 325–330

[KSM+21] KECK, Alexander ; SCHWARZ, Christoph ; MEURER, Thomas ; HECKMANN, Andreas ; GRETHER, Gustav: Estimating the wheel lateral position of a mechatronic railway running gear with nonlinear wheel–rail geometry. In: *Mechatronics* 73 (2021), S. 102457

[LK16] LEE, Nam-Jin ; KANG, Chul-Goo: Wheel slide protection control using a command map and Smith predictor for the pneumatic brake system of a railway vehicle. In: *Vehicle System Dynamics* 54 (2016), Nr. 10, S. 1491–1510

[LSY17] LU, Zheng-Gang ; SUN, Xiao-Jie ; YANG, Jun-Qi: Integrated active control of independently rotating wheels on rail vehicles via observers. In: *Proceedings of the Institution of Mechanical Engineers, Part F: Journal of Rail and Rapid Transit* 231 (2017), Nr. 3, S. 295–305

[MG01] MEI, T. X. ; GOODALL, R. M.: Robust control for independently rotating wheelsets on a railway vehicle using practical sensors. In: *IEEE Transactions on Control Systems Technology* 9 (2001), Nr. 4, S. 599–607

[MG03] MEI, T. X. ; GOODALL, R. M.: Practical Strategies for Controlling Railway Wheelsets Independently Rotating Wheels. In: *Journal of Dynamic Systems, Measurement, and Control* 125 (2003), Nr. 3, S. 354–360

[Mod22] MODELICA ASSOCIATION: *Functional Mock-up Interface: The leading standard to exchange dynamic simulation models.* `https://fmi-standard.org/`. Version: 2022. – last accessed: 28/11/2022

[MTD+10] MORARI, Manfred ; THOMA, Manfred ; DEL RE, Luigi ; ALLGÖWER, Frank ; GLIELMO, Luigi ; GUARDIOLA, Carlos ; KOLMANOVSKY, Ilya: *Automotive Model Predictive Control*. Bd. 402. London : Springer, 2010

[PBMV04] PÉREZ, J. ; BUSTURIA, Jesús M. ; MEI, T. X. ; VINOLAS, J.: Combined active steering and traction for mechatronic bogie vehicles with independently rotating wheels. In: *Annual Reviews in Control* 28 (2004), Nr. 2, S. 207–217

[Pol99] POLACH, Oldrich: A Fast Wheel-Rail Forces Calculation Computer Code. In: *Vehicle System Dynamics* 33:sup1 (1999), S. 728–739

[Pol05] POLACH, Oldrich: Creep forces in simulations of traction vehicles running on adhesion limit. In: *Wear* 258 (2005), Nr. 7-8, S. 992–1000

[SBH19] SCHWARZ, Christoph ; BREMBECK, Jonathan ; HECKMANN, Benjamin: Dynamics observer for the longitudinal behavior of a wheelset on a roller rig. In: *Proceedings of the Institution of Mechanical Engineers, Part F: Journal of Rail and Rapid Transit* 233 (2019), Nr. 10, S. 1112–1119

[SEEA08] STÜTZLE, Thorsten ; ENGELHARDT, Thomas ; ENNING, Manfred ; ABEL, Dirk: Wheelslide and Wheelskid Protection for a Single-Wheel Drive and Brake Module (SDBM) for Rail Vehicles. In: *IFAC Proceedings Volumes* 41 (2008), Nr. 2, S. 16051–16056

[SG22] SCHWARZ, Christoph ; GOETJES, Björn: Integrated vehicle dynamics control for a mechatronic railway running gear. In: *Proc. Fifth International Conference on Railway Technology: Research, Development and Maintenance*, 2022

[SK19] SCHWARZ, Christoph ; KECK, Alexander: Observer Synthesis for the Adhesion Estimation of a Railway Running Gear. In: *IFAC-PapersOnLine* 52 (2019), Nr. 15, S. 319–324

[SK20] SCHWARZ, Christoph ; KECK, Alexander: Simultaneous Estimation of Wheel-Rail Adhesion and Brake Friction Behaviour. In: *IFAC-PapersOnLine* 53 (2020), Nr. 2, S. 8470–8475

[SPG21a] SCHWARZ, Christoph ; POSIELEK, Tobias ; GOETJES, Björn: Adhesion-Based Maximum-Seeking Brake Control for Railway Vehicles. In: *Proc. 27th IAVSD International Symposium on Dynamics of Vehicles on Roads and Tracks*, 2021

[SPG21b] SCHWARZ, Christoph ; POSIELEK, Tobias ; GOETJES, Björn: Beobachterbasierte Kraftschlussregelung von Scheibenbremssystemen. In: *Proc. 3rd International Railway Symposium Aachen (IRSA)*, 2021, S. 120–135

[ST10] SAVARESI, Sergio M. ; TANELLI, Mara: *Active braking control systems design for vehicles*. London and Dordrecht and Heidelberg and New York : Springer, 2010 (Advances in industrial control)

[Tag22] TAGESSCHAU: *Deutsche Bahn: ICE-Züge ohne Stufen starten 2024*. `https://www.tagesschau.de/wirtschaft/unternehmen/bahn-ice-preisehoehungen-101.html`. Version: 2022. – last accessed: 02/11/2022

[ZRCD15] ZHAO, Haiyan ; REN, Bingtao ; CHEN, Hong ; DENG, Weiwen: Model Predictive Control Allocation for Stability Improvement of Four–Wheel Drive Electric Vehicles

in Critical Driving Condition. In: *IET Control Theory & Applications* 9 (2015), Nr. 18, S. 2688–2696